REINVENTING THE MOUSE WHEEL: A NEW MOUSE FOR THE MORE ACCURATE PRECLINICAL STUDY OF THERAPEUTIC ANTIBODIES FOR PATIENTS WITH CANCER

by

Emily Catherine Casey

A Dissertation

Presented to the Faculty of the Louis V. Gerstner, Jr.

Graduate School of Biomedical Sciences,

Memorial Sloan Kettering Cancer Center

in Partial Fulfillment of the Requirement for the Degree of

Doctor of Philosophy

New York, NY

May 2017

David A. Scheinberg MD, PhD Dissertation Mentor	Date

DEDICATION

I would like to dedicate this dissertation to my parents, Charles and Camille Casey, and my sister, Alyson Casey. Without their unwavering love, support, and confidence in me, none of these achievements would have been possible. They are the best cheerleaders a daughter and sister could hope for, and I am lucky to have them in my corner.

ABSTRACT

Human monoclonal antibody (mAb) therapies are potent, controllable, and highly effective methods for the specific targeting of many human cancers. Unmodified mAb therapies can act via direct antagonistic or agonistic cytotoxic mechanisms induced by the binding of an antibody to its epitope, or through interactions with the immune system via the constant (Fc) region of an antibody when bound to its target. Arguably the most important Fc-dependent mechanism is antibody-dependent cellular cytotoxicity (ADCC) mediated by Fcγ receptors (FcγRs) on immune effector cells. Despite the history of clinical success of many therapeutic antibodies to treat cancer, the success rate of mAbs to treat malignancies entering clinical trials is less than 10%, lower than mAbs for non-oncological indications. This discrepancy appears in phases II/III where lack of efficacy is observed despite robust demonstrations of therapeutic benefit in preclinical testing.

One potential source for this discrepancy is the major difference between the mouse and human FcγR networks. While therapeutic mAbs for non-oncological indications mainly depend on antibody-epitope interactions, antibodies to treat cancer largely rely on cancer cell death, and there is significant clinical evidence for the role of FcγRs in this process. The cellular expression patterns of FcγRs in the mouse and human vary, resulting in potentially critical differences in immune effector cell function in these two species. Additionally, the affinities and interactions between human IgGs and the mouse and human FcγRs differ greatly, resulting in altered functional outputs.

To address these issues and to more thoroughly study the role of FcγRs in therapeutic mAb action, we bred several novel mouse models that express the human FcγRs in lieu of the mouse FcγRs in the context of B and T cell deficiency to allow for

the xenografting of human cancer cells, called the RHuFR mouse. Flow cytometry analysis demonstrated the accurate expression of the human FcγRs on mouse effector leukocyte populations mimicking expression patterns in humans. Furthermore, functional studies (e.g. antibody-induced thrombocytopenia) utilizing the RHuFR and RHuFR derivative mice that express all the human FcγRs or lack one or more human FcγRs, respectively, exemplified the redundancy of the human FcγR network, as well as the usefulness of these models for identifying potential mechanisms by which antibodies result in phenotypic outputs driven by human Fcγ receptor interactions.

More importantly, our RHuFR mice are able to better mimic observed clinical outcomes than commercially available mouse FcγR expressing models with the same B and T cell deficiency via Rag2 knockout. This was highlighted in a therapy study where both mouse models were engrafted with a CD20+ human lymphoma cell line and treated with either rituximab, a anti-CD20 hIgG1, or obinutuzumab, an anti-CD20 Fc enhanced hIgG1. In the clinic, Obinutuzumab confers a significant progression-free survival advantage over Rituximab therapy. Our RHuFR mice showed a significant therapeutic and survival advantage when treated with Obinutuzumab compared to a modest benefit on Rituximab, while the mouse FcγR expressing model show little to no therapeutic benefit on either therapy and no difference in survival between the two treatments.

Overall, the human FcγR network is much more complex and intricate than the mouse FcγR system, and the two are not interchangeable. These novel RHuFR mice allow for the more accurate testing of antibody efficacy in treating human cancers, and provide invaluable tools for the identification of mechanisms of action, which can dictate the relevant patient populations best suited for a given therapeutic antibody.

BIOGRAPHICAL SKETCH

Emily Catherine Casey was born to Charles and Camille Casey on September 19th 1989 in New York, NY. Emily attended St. Andrew Avellino Elementary School in Flushing, NY were she was raised. She graduated from St. Francis Preparatory High School in Fresh Meadows, NY in 2007. Emily's pursuit of scientific research began in high school with her participation in the Science Research Program, where she learned to read and think critically about scientific publications and performed primary research in the lab of Dr. Saraswati Sukumar at Johns Hopkins Medical School during the summers of 2005 and 2006. Emily attended college at Cornell University's College of Agriculture and Life Sciences in Ithaca, NY where she studied biological sciences and biomedical engineering. She continued her research training in the labs of Dr. Carl Batt and Dr. Moonsoo Jin in the departments of Food Science and Biomedical Engineering, respectively. Concurrently, Emily spent her college summers as a summer undergraduate research (SURP) student in the Gerstner Sloan Kettering Graduate School of Biomedical Sciences at Memorial Sloan Kettering Cancer Center in New York, NY. As a SURP student, Emily worked in the lab of Dr. Lisa Denzin in the Immunology Program throughout the summer of 2008, followed by two summers (2009 and 2010) in the lab of Dr. David Scheinberg in the Molecular Pharmacology and Chemistry Program. Upon completion of her Bachelors in Science at Cornell in 2011, Emily began her PhD studies at Gerstner Sloan Kettering Graduate School in New York, NY that fall and joined the lab of Dr. David Scheinberg in the summer of 2012.

ACKNOWLEDGMENTS

First and foremost, I would like to thank my mentor, Dr. David Scheinberg, for all of his training, support, and patience. I would also like to thank all of the past and current members of his lab for their constant advice, willingness to lend a hand, and friendship. I would like to thank Dr. Stylianos Bournazos for all of his incredible teaching and assistance in regards to all things FcγR, and Dr. Jeffrey Ravetch for allowing me access to his research tools, resources, and animals.

I would like to thank the MSKCC Mouse Genetics Core facility staff, especially Dr. Willie Mark, Tanya Henry, Regina Lee, and Nneka Niles, for their vigilant efforts in helping me manage and care for the eleven mouse strains, as well as embryo cryopreservation and genotyping efforts. Thank you to George Mo and Dr. Patrizia Mondello for help characterizing the mice, and Dr. Kay See Tan for help with statistical analyses. Thank you to Dr. Dmitry Pankov for assistance with animal work and Dr. Michael Kharas and his lab for use of their Hemavet.

I would also like to thank the MSKCC Anti-Tumor Assessment Core, in particular Dr. Elisa de Stanchina, Dr. Huiyong Zhao, Dr. Qing Chang, Besnik Qeriqi, and Elizabeth Peguero, for assistance in engrafting and imaging my mice. Thank you to the MSKCC Small Animal Imaging Core and Flow Cytometry Core for help in using their machines and thank you to MSKCC Molecular Cytology Core, especially Dr. Katjia Manova, Yevgeniy Romin, and Vitaly Boyko, for assistance in microscopic imaging. Finally, thank you to my committee members, Dr. Marcel van den Brink and Dr. Morgan Huse, for all of their advice, and to the Gerstner Sloan Kettering Graduate School administration, staff, and students for making my journey here so memorable.

TABLE OF CONTENTS

LIST OF TABLES .... **xi**

LIST OF FIGURES .... **xii**

LIST OF ABBREVIATIONS .... **xiv**

INTRODUCTION **1**

Monoclonal Antibody Therapies Against Cancer *1*

Clinical Successes and Failures of Antibody Therapies for Cancer *5*

Mechanisms of Action of Cytotoxic Antibody Therapy *9*

Fcγ Receptors and their Importance in Antibody Therapy *13*

Introduction to the thesis *18*

CHAPTER I **19**

Introduction *19*

Materials and Methods *22*

Generation of immunodeficient human FcγR expressing RHuFR mice 22

Preparation of mouse leukocytes from spleen and blood 22

Generation of bone marrow derived macrophages and dendritic cells 22

Flow cytometry analysis of mouse leukocytes for mouse and human FcγR expression 23

Western blotting of human FcγRs 24

PCR of hFcγRIIB 24

Idiopathic thrombocytopenia purpura model 25

Iodine-125 labeling and rituximab and obinutuzumab blood half-life measurements 25

Surface plasmon resonance for measuring antibody-FcγR affinities 26
Lymphoma therapy study comparing rituximab and obinutuzumab therapy 27
Statistical analysis 28
Results *30*
Creation and characterization of the RHuFR mice 30
Testing the functional capacity of the RHuFR mice in a model of antibody-induced idiopathic thrombocytopenia purpura 47
Therapeutic human cancer antibody testing in the RHuFR mice 54
Discussion *65*
CHAPTER II **70**
Introduction *70*
Materials and Methods *75*
Cloning of ESK heavy chain variable regions into mouse IgG expression vectors . 75
Expression of ESK and mGO53 chimeric antibodies 76
Purification of ESK and mGO53 chimeric antibodies 76
Antibody protein gels 77
Flow cytometry analysis of ESK target cell binding 77
Surface plasmon resonance for measuring antibody affinities for mouse FcγRs 78
Iodine-125 labeling and ESK chimeric blood half-life measurements 78
Leukemia therapy study comparing ESK mouse chimeric antibody efficacy 79
Peptide pulsing of the TAP-deficient T2 human lymphoblastic cell line 80
Peripheral blood mononuclear cell (PBMC) isolation 80
ADCC *in vitro* assay using Chromium-51 release 81

Virus production, transduction, and selection of FRET vectors in T2 cells 81

3D time-lapse confocal microscopy 82

Statistical Analysis 83

Results 84

ESK therapeutic activity requires FcγR engagement 84

Quantification of ESK epitope site number for activation of NK cell ADCC 95

Discussion 116

CONCLUSIONS 123

BIBLIOGRAPHY 128

LIST OF TABLES

Table 1: List of FDA approved monoclonal antibody therapies for the treatment of human malignancies.. 6
Table 2: Human FcγR expression in human versus RHuFR mouse leukocytes............. 35
Table 3: Summary of novel RHuFR mice genotypes 36
Table 4: Rituximab and obinutuzumab affinity measurements for mouse FcγRs 60
Table 5: Rituximab and obinutuzumab affinity measurements for relevant human FcγRs 60
Table 6: ESK mouse chimeric antibodies affinities' for mFcγRs................................... 89
Table 7: List of RMF peptide probe sequences designed for the quantification of ESK1 epitope number.. 110

LIST OF FIGURES

Figure 1: Comparison of mouse and human FcγR networks 16

Figure 2: Creation of the novel immunodeficient human FcγR+ RHuFR mouse 31

Figure 3: Loss of mouse FcγR expression on mouse leukocytes in the Rag2-/- FcγR Null mouse 32

Figure 4: The RHuFR mice recapitulate human FcγR expression patterns on mouse leukocytes 34

Figure 5: Characterization of RHuFR^{1-} mouse 38

Figure 6: Characterization of RHuFR^{2A-} mouse 39

Figure 7: Characterization of RHuFR^{2B-} mouse 40

Figure 8: Characterization of RHuFR^{3A-} mouse 42

Figure 9: Characterization of RHuFR^{3B-} mouse 43

Figure 10: Western blot and PCR analysis of human FcγR expression 45

Figure 11: B and T cell loss in Rag2-/- FcR Null, RHuFR, and RHuFR “knockout” mice 46

Figure 12: RHuFR mice successfully deplete platelets in an antibody-induced model of ITP 48

Figure 13: The RHuFR single “knockout” mice are functionally intact 50

Figure 14: The combination RHuFR “knockout” mice reveal potential mechanisms of action for platelet depletion in an antibody-induced model of ITP 52

Figure 15: Rituximab and obinutuzumab blood half-lives in Rag2-/- mouse FcγR+, RHuFR, and RHuFR^{1-} mice 56

Figure 16: Mouse leukocyte population in Rag2-/- mouse spleens during engraftment protocol for human cancer cell xenografting 58

Figure 17: Obinutuzumab versus rituximab therapy of human lymphoma in Rag2-/- mouse FcγR+ mice 62

Figure 18: Obinutuzumab versus rituximab therapy of human lymphoma in RHUFR^{1-} mice 63

Figure 19: Frequency of overexpression of WT1 in selected hematopoietic malignancies and solid tumors 71

Figure 20: Production and purification of ESK and isotype mouse chimeric antibodies 86

Figure 21: ESK chimeric antibodies bind WT1+ HLA-A*02:01+ human leukemia cells specifically 87

Figure 22: ESK chimeric antibodies bind WT1+ HLA-A*02:01+ human mesothelioma cells specifically 88

Figure 23: ESK mouse chimeric blood half-lives in NSG mice 91

Figure 24: ESK-mIgG2a retains therapeutic efficacy in NSG mice to treat BV173 human leukemia 93

Figure 25: Model of the binding of the RMF-Biotin peptide probe to the MHC Class I HLA-A*02:01 binding groove 96

Figure 26: The RMF-Biotin peptide probe can be loaded onto MHC class I and be bound by ESK1 and streptavidin 98

Figure 27: The quantitation of RMF-Biotin/HLA-A*02:01 complexes on pulsed T2 cells measured by ESK1 and streptavidin staining 100

Figure 28: *In vitro* Cr-51 release assay on RMF and RMF-Biotin pulsed T2 cells mediated by ESK1 102

Figure 29: CFP-DEVD-YFP expressing T2 cells can be pulsed with RMF-Biotin 104

Figure 30: RMF-Biotin/HLA-A*02:01 complexes detected by SAv-AF647 are stable on the T2 cell surface 105

Figure 31: Time-lapse confocal microscopy of RMF-Biotin pulsed T2 CFP-DEVD-YFP cells bound by ESK1 and exposed the PBMCs 107

Figure 32: RMF-Biotin pulsed T2 cells no longer bind streptavidin labeled probes and have weaker ESK1 binding 108

Figure 33: RMF-K-Biotin and RMF-K-Cy5 pulsing of T2 cells 111

Figure 34: RMF-K-Cy5 is internalized into cells and results in nonspecific peptide/MHC signal 112

Figure 35: RMF-K-Biotin Short and RMF-K-Biotin Long pulsing of T2 cells 114

Figure 36: The quantitation of RMF-K-Biotin Short/HLA-A*02:01 complexes on pulsed T2 cells measured by ESK1 and streptavidin staining 115

LIST OF ABBREVIATIONS

ADC: Antibody-drug conjugate

ADCC: Antibody-dependent cell cytotoxicity

ADCP: Antibody-dependent cell phagocytosis

ALL: Acute lymphoblastic leukemia

AML: Acute myeloid leukemia

APC: Antigen-presenting cell

APC fluorophore: Allophycocyanin

AUC: Area under the curve

B-CLL: B cell CLL

BiTE: Bispecific T cell engager

BLI: Bioluminescence

BM: Bone marrow

CAR: Chimeric antigen receptor

CC: Cervical cancer

CDC: Complement-dependent cytolysis

cDNA: Complementary DNA

CDR: Complementarity-determining region

C_H: Constant domain of heavy chain

CLL: Chronic lymphocytic leukemia

CSF-1: Colony-stimulating factor-1

DAPI: 4',6-diamidino-2-phenylindole

DNA: deoxyribonucleic acid

E:T ratio: Effector-to-target ratio

Fab: Fragment antigen-binding region

FACS: Fluorescence-activated cell sorting

FBS: Fetal bovine serum

Fc: Fragment crystallizable region

FcγR: Fcγ receptor

FcRn: Neonatal Fc receptor

FDA: U.S. Food and Drug Administration

FRET: Förster resonance energy transfer

GEJ: Gastroesophageal junction adenocarcinoma

GM-CSF: Granulocyte macrophage colony-stimulating factor

GPI: Glycosylphosphatidylinositol

HAMA: Human anti-mouse antibody response

hFcγR: Human Fcγ receptor

hIgG: Human IgG

HOCL: Hypochlorus acid

HPLC: High-performance liquid chromatography

HRP: Horseradish peroxidase

Ig: Immunoglobulin

IgA: Immunoglobulin class α

IgD: Immunoglobulin class δ

IgE: Immunoglobulin class ε

IgG: Immunoglobulin class γ

IgM: Immunoglobulin class μ

IHC: Immunohistochemistry

IL-2: Interleukin-2

IL-2Rγ_C: IL-2 receptor γ-chain

IL-3: Interleukin-3

IL-4: Interleukin-4

I.P.: Intraperitoneal

ITAM: Immunoreceptor tyrosine-based activation motif

ITIM: Immunoreceptor tyrosine-based inhibitory motif

ITP: Idiopathic thrombocytopenia purpura

I.V.: Intravenous

K_D: Dissociation constant

mAb: Monoclonal antibody

MAC: Membrane attack complex

mBC: Metastatic breast cancer

mCRC: Metastatic colorectal cancer

mFcγR: Mouse Fcγ receptor

mGC: Metastatic gastric cancer

MHC: Major histocompatibility complex

mIgG: Mouse IgG

mNSCLC: Metastatic NSCLC

mRCC: Metastatic renal cell carcinoma

mRNA: Messenger RNA

msNSCLC: Metastatic squamous NSCLC

N.b.d.: No detectable binding

NFAT: Nuclear factor of activated T cells

NHL: Non-Hodgkin’s lymphoma

NK cell: Natural killer cell

NOD: Non-obese diabetic mice

NSCLC: Non-small cell lung cancer

NSG: NOD/SCID IL2R$\gamma_C^{-/-}$ mice

Nuc: Nuclear staining

PBMC: Peripheral blood mononuclear cell

PBS: Phosphate buffered solution

PCR: Polymerase chain reaction

PE: R-Phycoerythrin

P.i.: Post-injection

PNGase F: Peptide:N-Glycosidase F

prOC: Platinum-resistant ovarian cancer

PVDF: Polyvinylidene fluoride

Rag: Recombination-activating gene

RCC: Renal clear cell carcinoma

rGBM: Recurrent glioblastoma multiforme

RHuFR: Rag2-/- human FcγR expressing mouse

RHuFR^{1-}: RHuFR “knockout” hFcγRI

RHuFR$^{1/2A-}$: RHuFR “knockout” hFcγRI and hFcγRIIA

RHuFR$^{1/2B-}$: RHuFR “knockout” hFcγRI and hFcγRIIB

RHuFR$^{1/3A-}$: RHuFR “knockout” hFcγRI and hFcγRIIIA

RHuFR$^{1/3B-}$: RHuFR “knockout” hFcγRI and hFcγRIIIB

RHuFR^{2A-}: RHuFR “knockout” hFcγRIIA

RHuFR^{2B-}: RHuFR “knockout” hFcγRIIB

RHuFR^{3A-}: RHuFR “knockout” hFcγRIIIA

RHuFR^{3B-}: RHuFR “knockout” hFcγRIIIB

RMF: RMFPNAPYL WT1-derived 9-mer peptide

RMF-K: RMFPNAPKL 9-mer peptide

RNA: ribonucleic acid

ROS: Reactive oxygen species

RT-PCR: Real-time PCR

sALCL: Systemic anaplastic large cell lymphoma

SAv: Streptavidin

SCCHN: Squamous cell carcinoma of the head and neck

scFv: Single-chain variable fragment

SCID: Severe combined immunodeficiency mice

SEM: Standard error of the mean

SIM: Structured illumination microscopy

SPR: Surface plasmon resonance

STORM: Stochastic optical reconstruction microscopy

STS: Soft tissue sarcoma

TAP: Transporter associated with antigen processing

TCA: Trichloroacetic acid

TCR: T cell receptor

TCRm: TCR-mimic

TLC: Thin-layer chromatography

UC: Urothelial carcinoma

V_H: Variable domain of heavy chain

V_L: Variable domain of light chain

WB: Western blot

WT: Wild type

WT1: Wilms' tumor 1 protein

INTRODUCTION

Monoclonal Antibody Therapies Against Cancer

Over the past 20 years, monoclonal antibody (mAb) therapy has become an established and successful method for the treatment of human cancers. The use of antibodies as tools to treat cancer was first conceived upon the discovery of tumor-specific antigens (1). These tumor-specific antigens are proteins that are overexpressed, mutated, or selectively expressed by cancer cells compared to normal tissues. Antibodies are capable of selectively recognizing and binding to these antigens, therefore making them highly effective modalities for both cancer detection and therapy.

Antibodies, or immunoglobulins (Igs), are unique, polymorphic Y-shaped protein multimers, most commonly 150kDa, expressed by B cells as a natural part of the adaptive immune response. They are made up of four protein chains, two heavy chains and two light chains. Each heavy and light chain contains a variable domain (V_H and V_L, respectively) that together creates the epitope-binding site. The heavy chains contain three or more constant domains (C_H) that allow for interactions with the immune system. The branched part of the antibody where the light and heavy chains interacts is known as the fragment antigen-binding (Fab) region, while the base of the antibody where the heavy chains interact is known as the fragment crystallizable (Fc) region. This structure allows for antibodies to engage specifically with a target epitope while simultaneously interacting with the immune system. (2)

Antibodies can be categorized into classes and subclasses based on the composition of the constant domains of their heavy chains. There are five antibody classes: IgG, IgM, IgA, IgE, and IgD. The IgG class is the most common antibody class and is responsible for B cell mediated adaptive immune responses to bacterial and viral infections. IgGs can be broken down further into subclasses, which dictate their interactions with the immune system and direct their functional output. (3)

Historically, antibodies were first produced against a target antigen via isolation from the serum of animals vaccinated with a peptide or protein from that target (4). Upon repeated vaccinations, antibodies targeting a specific protein can be isolated. These are known as polyclonal antibodies, which likely share a target protein, but have distinct variable regions and thus distinct epitopes on that target protein. The production of polyclonal antibodies is effective and relatively quick and simple. However, the lack of specificity makes the use of polyclonal antibodies risky for therapeutic purposes due to the increased chance of off target interactions (5). Therefore, monoclonal antibodies, which are identical in composition and bind to the same epitopes, are more suitable for therapeutic applications.

Monoclonal antibodies were first produced in the laboratory by Kohler and Millstein in 1975 upon their discovery of hybridoma technology (6). This process was originated in mice, but can be applied to other mammals, and begins with the vaccination of that animal with an antigen of interest. B cells from the vaccinated animal producing the antibody of interest are then isolated and fused with a myeloma cell line. These now immortalized fusion cells are sequentially screened for the isolation of single clones secreting the antibodies of interest. Once identified, these hybridoma clones serve as an unlimited source for individual mAbs.

The development of hybridoma technology allowed researchers to create single antibody clones that bind to a desired antigen. The first approved mAb in the clinic developed by this technology, Orthoclone OKT3 (muromonab-CD3), is a mouse IgG targeting the CD3 antigen expressed on T cells for the prevention of acute kidney transplant rejection (7). However, the efficacy of this antibody is limited due to the production of human anti-mouse antibodies (HAMA) in many patients, which renders the antibody ineffective (8). Therefore, new approaches for adapting mAbs for use in the clinic were necessary.

This led to the creation of chimeric and humanized mAbs using DNA recombination techniques. Chimeric antibodies consist of the variable domain of the mouse or other mammal that the hybridoma originated from fused to the constant domains of a human IgG (9). Meanwhile, humanized antibodies go one step further and can be created in a number of different ways. One way is to selectively substitute amino acids in the remaining mouse variable domain of a chimeric antibody intermediate by DNA mutagenesis (10). However, this method must not alter the amino acids within the complementarity-determining region (CDR). The CDR is the region of an antibody's variable fragment that directly interacts with its target epitope and altering its structure can affect the ability of an antibody to bind its antigen. Another method is to directly insert the DNA encoding the CDRs from a hybridoma derived mAb directly onto a human IgG DNA scaffold (11).

The most recent technological advance for antibody production, called phage display technology, removes the need for these processes and hybridoma technology altogether. This technology requires the establishment of phage library, which is created by isolating the mRNA from circulating human B cells, creating cDNA libraries, and PCR amplifying the variable regions (V_H and V_L). These variable regions are then cloned into a Fab or single chain variable fragment (scFv) vector, which is linked to a bacteriophage surface protein, and then transduced into bacteria. For library production, the bacteria is infected with a helper phage that allows for the expression and packaging of the Fab or scFv DNA into phage particles that both carry the gene and display the Fab/scFv on its surface. This library can then be sequentially screened and enriched for phages that bind to a desired antigen. (12)

Once complete, the remaining phages can be used to re-infect bacteria, and the vector can be isolated to identify the candidate variable regions that bind to the antigen of interest. These can then be reverse engineered into a full length human IgG by inserting them into a human IgG DNA scaffold and produced in a mammalian cell expression system. Screening for retention of antigen binding, specificity, and affinity throughout this process is important to identifying the most promising therapeutic antibody candidate. With this new technology, mAbs with higher specificity and greater affinity can be produced without worry of a patient's humoral response. This allows researchers to target tumor antigens with higher efficiency, accuracy, and safety than before.

Clinical Successes and Failures of Antibody Therapies for Cancer

As of January 2017, 25 mAb therapies have been approved by the FDA for the treatment of human hematological malignancies and solid tumors (Table 1). The first mAb approved by the FDA for the treatment of cancer was rituximab (Rituxan) in 1997 (13). Rituximab is a chimeric human IgG1 that binds to the CD20 cell surface protein (14). CD20 is selectively expressed along the B cell lineage of immune lymphocytes, therefore making it an ideal target for B cell leukemias and lymphomas, including chronic lymphocytic leukemias (CLL) and non-Hodgkin's lymphomas (NHL). Rituximab has been highly successful in the clinic over the past 20 years (15), becoming a first-line therapy for many leukemia and lymphoma patients in combination with chemotherapy.

Soon after the approval of rituximab, trastuzumab (Herceptin) was approved by the FDA for the treatment of breast cancer in 1998 (16). Trastuzumab is a humanized hIgG1 that targets the Her2 transmembrane protein (17). Unlike CD20, Her2 expression is not relegated to breast cells, but rather is overexpressed in many forms of breast cancer and other cancers compared to normal tissues. This enables trastuzumab to selectively target the Her2 overexpressing cancer cells, resulting in a specific therapeutic effect with limited side effects. Trastuzumab is now a first-line therapy for patients with metastatic breast cancer as well as an adjuvant therapy during the early stages of breast cancer.

The early successes of rituximab and trastuzumab propelled efforts to develop more cancer targeting mAb therapies. Some of these efforts have been successful, such as cetuximab (Erbitux) targeting EGFR-positive head and neck carcinomas and metastatic colorectal cancers (18,19). However, as a whole, the market for therapeutic mAbs to treat cancer remains small. One reason for this is the limited discovery of cell surface antigens

TABLE 1

Antibody Name	Brand Name	Antigen(s)	Indication(s)	Antibody Type
Brentuximab vedotin	Adcetris	CD30	Hodgkin Lymphoma, sALCL	ADC
Ofatumumab	Arzerra	CD20	CLL	Chimeric hIgG1
Bevacizumab	Avastin	VEGF	mCRC, NSCLC, prOC, CC, mRCC, rGBM	Humanized hIgG1
Tositumomab I-131	Bexxar	CD20	NHL	ADC
Blinatumomab	Blincyto	CD19/CD3	ALL	Bispecific
Alemtuzumab	Campath	CD52	B-CLL	Humanized hIgG1
Ramucirumab	Cyramza	VEGF	mGC, GEJ, mNSCLC, mCRC	hIgG1
Daratumumab	Darzalex	CD38	Multiple Myeloma	hIgG1
Elotuzumab	Empliciti	SLAMF7	Multiple Myeloma	Humanized hIgG1
Cetuximab	Erbitux	EGFR	SCCHN, mCRC	Chimeric hIgG1
Obinutuzumab	Gazyva	CD20	CLL, Follicular Lymphoma	Fc enhanced hIgG1
Trastuzumab	Herceptin	Her2	Adjuvant Breast Cancer, mBC, mGC	Humanized hIgG1
Ado-Trastuzumab emtansine	Kadcyla	Her2	mBC	ADC
Pembrolizumab	Keytruda	PD-1	NSCLC, SCCHN, Melanoma	hIgG4
Olaratumab	Lartruvo	PDGFRα	STS	hIgG1
Gemtuzumab ozogamicin	Mylotarg	CD33	AML	ADC
Nivolumab	Opdivo	PD-1	NSCLC, Melanoma, RCC, SCCHN, Hodkin Lymphoma, UC	hIgG4
Pertuzumab	Perjeta	Her2	Breast Cancer	Humanized hIgG1
Necitumumab	Portrazza	EGFR	msNSCLC	hIgG1
Rituximab	Rituxan	CD20	NHL, CLL	Chimeric hIgG1
Atezolizumab	Tecentriq	PD-L1	mNSCLC, UC	Humanized hIgG1
Dinutuximab	Unituxin	GD-2	Pediatric Neuroblastoma	Chimeric hIgG1
Panitumumab	Vectibix	EGFR	mCRC	hIgG2
Ipilimumab	Yervoy	CTLA-4	Melanoma	hIgG1
Ibritumomab tiuxetan	Zevalin	CD20	NHL	ADC

Table 1: List of FDA approved monoclonal antibody therapies for the treatment of human malignancies. See list of abbreviations for explanation of indications.

selectively expressed or overexpressed by cancer cells. Since antibodies can only target proteins on the cell surface, they are limited to this class of proteins as potential binding epitopes. This is reflected in the limited list of targets for the current FDA approved mAbs (Table 1). Of the 25 antibody therapies listed, many of them target the same proteins, suggesting that the discovery of unique cancer-specific targets for mAb therapy is a limiting factor.

Another potential cause for the slow growth of the therapeutic mAb market is the discrepancy between preclinical and clinical efficacy. Many therapeutic mAbs demonstrate compelling efficacy in preclinical mouse models that supports movement into the clinic (20-24). However, upon entering phases II or III of clinical trials, many mAbs fail to prove efficacious enough to warrant FDA approval. Examples of these include lintuzumab (anti-CD33) for AML (25,26), farletuzumab (anti-Folate receptor α) for ovarian cancer (27), brentuximab and iratumumab (anti-CD30) for Hodgkin lymphoma (28,29), and adecatumumab (anti-EpCAM) for breast cancer (30).

Overall, antibodies entering clinical trials have an approximately 14% chance of FDA approval, with less than 40% of mAbs entering phase II clinical trials proving efficacious enough for phase III study (31). Even more striking is the discrepancy between antibodies for oncological indications and non-oncological indications. mAb therapies indicated for oncology have a 9.3% chance of gaining FDA approval, while those for non-oncological indication have a 19.3% chance (31). This difference arises in phases II and III where cancer-targeting mAbs have a significantly lower chance of proving efficacious enough for approval compared to those for non-oncological indications. This discrepancy between indications is not observed for other drug classifications, including small molecule inhibitors.

This suggests that current preclinical mouse models for testing therapeutic mAb efficacy against human cancers are inadequate for predicting clinical efficacy. Furthermore, the lower success rates of oncology mAbs compared to those for non-oncological indications may be directly linked to the different mechanisms of action employed by these two classes of therapeutic mAbs. Most cancer targeting mAbs require death of their target cell in order to prove effective, while those for other applications involve modulation of the immune system and typically do not require cytotoxic effects. Therefore, it is important to understand the mechanisms of action of therapeutic cancer mAbs to formulate a potential solution to this problem.

Mechanisms of Action of Cytotoxic Antibody Therapy

Antibodies have innate cytotoxic capabilities via Fc-independent and/or Fc-dependent mechanisms. Fc-independent mechanisms involve the direct cytotoxic effects resulting from the binding of an antibody to its target epitope. These can be agonistic or antagonistic in nature. Agonistic cytotoxicity involves the activation of apoptotic or other cell death signaling within a target cell upon the binding of an antibody to its target antigen on that cell (32-34). Antagonistic cytotoxicity includes the blockage of growth factors or oncogenic signaling by an antibody that the target cell is dependent upon for growth and/or survival, therefore resulting in target cell death (35,36). Many commercially available therapeutic antibodies to treat cancer have been shown to have direct cytotoxic capabilities in an Fc-independent manner *in vitro*. However, there is little evidence for the role of these mechanisms *in vivo*, especially in the clinic.

Fc-dependent cytotoxic mechanisms can be mediated through two main immune system components: complement-dependent cytolysis (CDC) and antibody-dependent cell cytotoxicity (ADCC). CDC involves the deposition of complement proteins onto the Fc region of antibodies bound to a target cell and subsequent cell lysis. The initiating complement protein, C1q, binds to the Fc region of an antibody and forms a hexamer with six C1q molecules interacting with six antigen-bound antibody Fc regions. This promotes the activation of the complement cascade via recruitment of other complement proteins to the antibody-bound target cell membrane. The cascade ends with the formation of the membrane attack complex (MAC) composed of multiple members of the complement protein family. The MAC forms a small pore within the cell membrane of the antibody-bound cell, resulting in the lysis of the target cell. (37)

Meanwhile, ADCC is mediated by the Fcγ receptor (FcγR) family expressed by immune effector cells, including NK cells, monocytes, macrophages, and neutrophils. FcγRs can recognize and bind to the Fc region of an IgG and can be activating or inhibitory in nature. Activating FcγRs contain an ITAM, or immunoreceptor tyrosine-based activation motif, within their intracellular signaling domain. ITAM phosphorylation occurs upon FcγR clustering resulting from the binding to IgG opsonized particles/cells. Inhibitory FcγRs contain an intracellular ITIM, or immunoreceptor tyrosine-based inhibitory motif, which is also phosphorylated upon FcγR engagement and clustering. ITIM phosphorylation results in the recruitment of phosphatases that block tyrosine-phosphorylation mediated signaling, such as that promoted by an ITAM. Since the majority of immune effector cell types express one or more activating FcγRs simultaneously with an inhibitory FcγR, the ratio of activating to inhibitory FcγR binding to an IgG-bound target will determine if the cell is activated. (38)

If an immune effector cell is activated by its FcγR signaling, it can initiate the death of the antibody-bound target cell through one of two ways. Activated NK cells will secrete cytotoxic molecules, such as perforin and granzymes, as well as engage death receptors (e.g. Fas, TRAIL) on target cells with their cognate ligands, resulting in target cell death via caspase activation and apoptosis (39). Meanwhile, monocytes and macrophages activated by FcγR signaling are largely believed to phagocytose an antibody-bound target cell (40,41), also known as antibody-dependent cell phagocytosis (ADCP). The mechanisms by which neutrophils mediate ADCC are not yet clear. However, it is believed they can act through a variety of potential mechanisms similar to their antimicrobial functions, including reactive oxygen species (ROS) and hypochlorus acid (HOCL) production and TRAIL engagement (42). In addition, activation of all effector cells can result in inflammatory cytokine secretion, resulting in the recruitment and activation of surrounding leukocytes to augment cytotoxic effects.

The different IgG subclasses have varying affinities for the activating and inhibitory FcγRs, and this correlates to their function *in vivo*. Specifically, the ratio of the affinity of an antibody for an activating FcγR to its affinity for an inhibitory FcγR, known as the A/I ratio, is directly correlated to the therapeutic activity of that antibody *in vivo* (43). For example, the mouse IgG2a and human IgG1 antibody subclasses have high A/I ratios and are the most potent mediators of ADCC in their respective species, while mouse IgG1 and hIgG4 have low A/I ratios and promote little to no activation of immune effector cells for ADCC (44). Thus, modulating an antibody's interaction with FcγRs directly influences its therapeutic potential.

For therapeutic antibodies that fail to prove efficacious in their native forms, a number of alternative approaches can be used to endow them with a therapeutic benefit. One such approach includes the conjugation of radioisotopes, toxins, or drugs to the antibody, using it as a vehicle for targeting to the payload directly to the cancer cells (45). These antibody-drug conjugates, or ADCs, have been successfully used in the clinic and a few have gained FDA approval (Table 1). However, one major caveat to ADCs involves the requirement for antibody internalization into a target cell for those carrying toxin or drug payloads in order to be effective. In addition to ADCs, antibodies can now be engineered into number of different novel therapeutics, including bispecific T cell engagers (BiTEs) and chimeric antigen receptor (CAR) T cells. These therapeutics employ the scFv of an antibody used to bind its epitope. In the case of BiTEs, the scFv of the targeting antibody is fused to the scFv specific to CD3, expressed by T cells. This allows the BiTE to specifically bind to a cancer cell expressing your target antigen and T cells at the same time, while simultaneously activating the T cell through epitope clustering (46). Meanwhile, CAR T cells are engineered to express the scFv of an antibody to specifically target a cancer cell expressing the target antigen. Therefore, the CAR T cell can home to the cancer via the scFv and become activated through primary and secondary signals (47). These applications of antibodies have proven to be highly promising in the clinic, specifically for the CD19 B cell antigen (48,49). However, these approaches have yet to be widely applied largely due to their high sensitivity and low activation threshold, increasing the chance of off target toxicities, as well as due to major adverse reactions cause by wide scale T cell activation and cytokine storming.

Fcγ Receptors and their Importance in Antibody Therapy

While studies *in vitro* have demonstrated the capability of successful commercially available antibodies to activate both CDC and ADCC, their reliance on these mechanisms for therapeutic success *in vivo* is unequal. Modifications to the Fc region of an antibody can selectively diminish its ability to engage C1q or activating FcγRs. When tested *in vivo*, antibodies incapable of target redistribution into lipid rafts were unaffected by loss of complement, while antibodies resulting in lipid raft formation had only a slight decrease in efficacy (50,51). Furthermore, in mice deficient for CDC, therapeutic antibodies retain their efficacy (52,53). However, antibodies with diminished activating FcγR binding lose therapeutic activity *in vivo*, while mice deficient in activating hFcγR signaling do not retain antibody therapy (54,55).

The importance of FcγRs for therapeutic antibody activity is further supported by clinical evidence. Patients carrying allelic variants of the activating FcγRs that confer higher affinity for therapeutic antibodies responded better to therapy when treated with rituximab, trasutuzumab, or cetuximab mAbs (56-60). Meanwhile, for lymphoma patients receiving rituximab therapy, those patients with a C1q allelic variant that reduces the available levels of this protein, thus resulting in decreased lytic complement activity, have increased response rates and prolonged time to relapse (61). Complement activation has even been shown to dampen the cytotoxic effects induced by NK cells for ADCC mediated by therapeutic antibodies (62). These data support the importance of activating FcγR signaling for therapeutic antibody efficacy and suggest that complement activity is unnecessary and a potential impediment to therapeutic antibody success.

Therefore, recent efforts in therapeutic antibody development have been focused on creating antibodies with enhanced activating FcγR engagement in order to increase the A/I ratio of an antibody (63). To achieve this, the Fc region of an antibody must be modified in one of two ways. This first approach is to introduce specific point mutations in the Fc region to enhance the binding affinity for activating FcγRs more so than inhibitory FcγRs. A number of amino acid residues in the IgG Fc region have been identified as key mediators of FcγR binding, and thus have been selectively mutated to enhance this binding (64). This methodology has been validated to increase the A/I ratio and *in vitro* ADCC activity of therapeutic mAbs (65).

The second approach to Fc engineering involves the alteration in the glycosylation pattern of an antibody's Fc region. The sugar residues attached to the heavy chains in the Fc region of an antibody play a key role in the interaction of the antibody with FcγRs. Therefore, modifications to the glycan structure can alter this interaction by either diminishing it or enhancing it (66). Specifically, the removal of a fucose residue in the glycan chain can greatly increase the affinity of an antibody to activating FcγRs (67). Glycoengineering of antibodies has been highly successful for improving therapeutic efficacy (68,69). Most notable is the recent FDA approval of the first Fc engineered antibody, obinutuzumab (Gazyva). Obinutuzumab (anti-CD20) is a humanized IgG1 that has reduced levels of fucosylated glycans on its Fc region due to manipulations in the glycosidases present in the mammalian expression system used to produce it (70). The reduction in fucosylated glycan chains on obinutuzumab results in enhanced activating FcγR binding affinity and greater therapeutic benefit in the clinic when compared to another anti-CD20 antibody, rituximab (71,72).

With the growing knowledge of the importance of FcγR engagement in therapeutic antibody success and the recent emphasis of Fc engineering in therapeutic antibody development, it is critical to understand the biology of the FcγR networks in both humans and the mouse preclinical models used to test their efficacy. The mouse FcγR system consists of three activating receptors (mFcγRI, mFcγRIII, & mFcγRIV) and one inhibitory receptor (mFcγRII), while the primary human FcγR system consists of three activating receptors (hFcγRI, hFcγRIIA, & hFcγRIIIA), an inhibitory receptor (hFcγRIIB), and a GPI-anchored "decoy" receptor (hFcγRIIIB) (73). FcγRI in both mice and humans has minimal contribution to *in vivo* activity due to its high affinity IgG binding domain, which allows FcγRI to bind serum monomeric IgG (43,74). Meanwhile, the remaining FcγRs are low affinity receptors that rely on the avidity of multimeric IgG bound to a target cell for engagement (38). This allows for FcγR clustering, phosphorylation of the intracellular ITAM and ITIM motifs, and downstream signaling.

Despite some similarities in structural homology between the two species, there are many critical differences between the human and mouse FcγR systems that can result in differences in the functional output of a therapeutic antibody (Figure 1). Mouse NK cells exclusively express mFcγRIII, while human NK cells express hFcγRIIIA. mFcγRIII has been shown to only modestly contribute to mAb efficacy *in vivo*, with mFcγRIV being the critical activating receptor for antibody therapy (53,75). Therefore, mouse NK cells are virtually dispensable for effective antibody therapy. In humans, however, NK cells play an important role in antibody therapy in patients. Studies have shown the activation of NK cells in lymphoma patients following rituximab administration, and follicular lymphoma patients carrying a defective hFcγRIIb allele do not show any

FIGURE 1

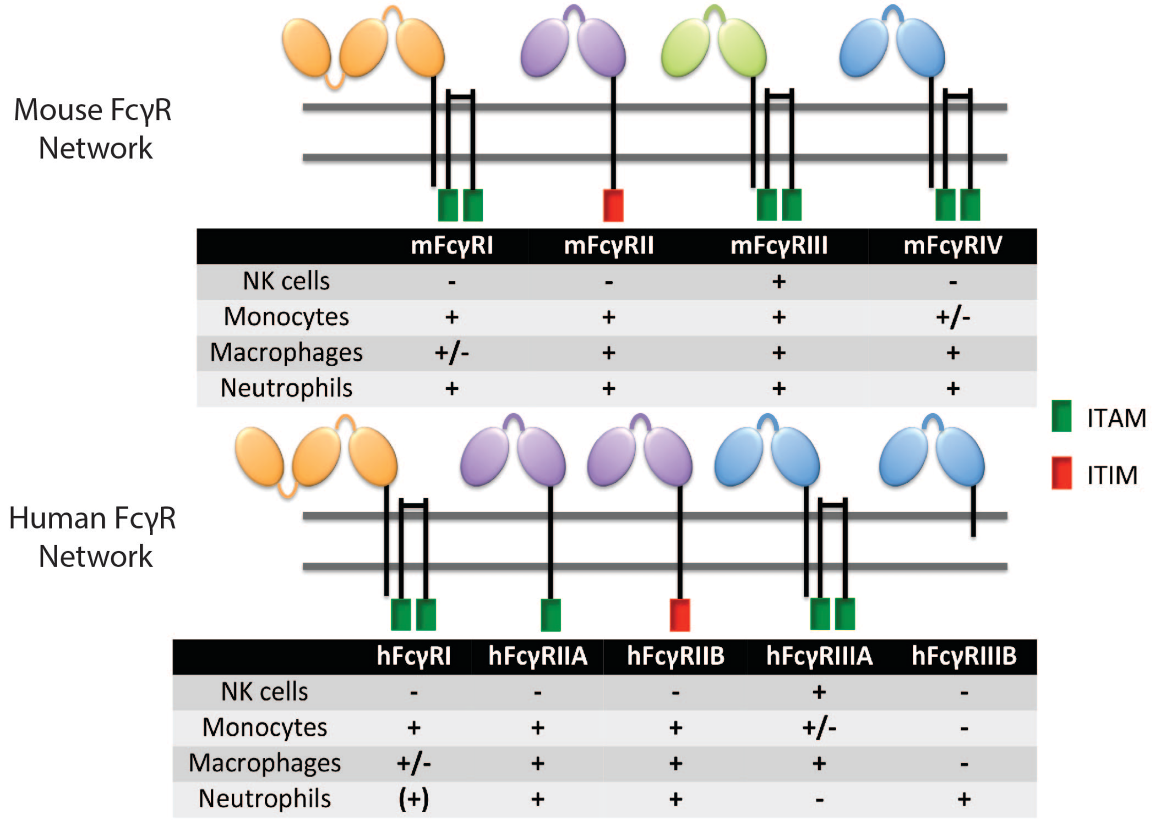

	mFcγRI	mFcγRII	mFcγRIII	mFcγRIV
NK cells	-	-	+	-
Monocytes	+	+	+	+/-
Macrophages	+/-	+	+	+
Neutrophils	+	+	+	+

	hFcγRI	hFcγRIIA	hFcγRIIB	hFcγRIIIA	hFcγRIIIB
NK cells	-	-	-	+	-
Monocytes	+	+	+	+/-	-
Macrophages	+/-	+	+	+	-
Neutrophils	(+)	+	+	-	+

Figure 1: Comparison of mouse and human FcγR networks. The structures and associated signaling domains for both human and mouse Fcγ receptors. The presence of an ITAM or an ITIM in the FcγR or its associated γ-subunit will determine whether the receptor promotes the activation or inhibition of an effector cell, respectively. The summary tables depict which receptors are expressed by specific leukocyte populations in their given species. + indicates receptor expression, - indicates lack of receptor expression, (+) indicates inducible expression, +/- indicates expression on some, but not all, cellular subsets.

enhanced therapeutic response to rituximab (76,77). Furthermore, NK cells express hFcγRIIIA, a critical receptor for antibody therapy in humans. Specifically, the hFcγRIIIA polymorphism V158F can predict the success of antibody therapies in the clinic, with those patients expressing the V158 polymorphism having stronger therapeutic responses than those with the F158 polymorphism (56-60,78), due to the enhanced affinity of the hFcγRIIIA^{V158} allele for hIgG1.

Other critical differences include the expression of mFcγRIV on mouse neutrophils and the lack of hFcγRIIIA on human neutrophils. Instead, human neutrophils express hFcγRIIIB, a GPI-anchored receptor that lacks an intracellular signaling domain. Mice do not have an equivalent hFcγRIIIB signaling-deficient receptor. This suggests that human neutrophils interact very differently with antibody-bound target cells than mouse neutrophils do. Additionally, monocytes and macrophages expressing both the activating and inhibitory FcγRs can have varied functional outputs depending on the levels of expression of the activating and inhibitory receptors. Since the regulatory elements of these immune effector cells varies, as indicated by the differences in expression of the FcγRs in cellular subsets (Figure 1), this suggests that the expression levels of the activating and inhibitory FcγRs in these cell populations is not conserved between species. Therefore, mouse and human monocytes and macrophages can react differently to therapeutic antibodies. Furthermore, human IgGs have different affinities for the mouse and human FcγRs, thus resulting in altered A/I ratios in a mouse versus a human FcγR system (79,80). These affinity differences can result in large differences in functional output of an immune effector cell, and thus in therapeutic efficacy of an antibody in these two species.

Introduction to the thesis

In this thesis, I will address two main points of my research concerning the understanding and testing of therapeutic antibodies. In chapter I, I will discuss the creation and characterization of a new human FcγR expressing immunocompromised mouse for the testing of therapeutic antibodies for the treatment of human cancers. I will also demonstrate that this new mouse can be used to model xenografted human cancers and can recapitulate clinical data comparing two anti-CD20 antibodies. This mouse model and other models described in this chapter provide a solution to the current preclinical efficacy-testing problem, supplying the research community with a more biologically relevant model to test mAb therapy, as well as tools to explore FcγR function in antibody therapy.

In chapter II, I will discuss the use of a new therapeutic antibody, called ESK1, that functions solely through ADCC as a tool for understanding the limitations of ADCC. Specifically, due to the nature of the ESK antibody, we can use it to determine the exact number of epitope sites required for an antibody to engage on a target cell in order to activate an NK cell for target cell killing. Together, this thesis will help the community to better understand FcγR biology, its role in therapeutic antibody efficacy, and the power of ADCC.

CHAPTER I

Introduction

The human FcγR network is much more complex and intricate than the mouse FcγR system, and the two are not equivalent and therefore not interchangeable. There are key differences in the function of mouse and human FcγRs, as well as differences in the expression pattern of these receptors on immune effector cells, most notably NK cells and neutrophils (Figure 1) (38,81). Furthermore, the regulation of expression of the activating and inhibitory FcγRs in the mouse and human networks is distinct, as seen in the different expression patterns for monocyte and macrophage cellular subsets (82). Therefore, the threshold level for activation of an effector cell coexpressing activating and inhibitory FcγRs, such as monocytes, macrophages, and neutrophils, in mice and humans can vary greatly.

In addition to distinctions between the FcγR networks in these two species, human IgGs interact differently with mouse and human FcγRs due to differences in affinity (79). Moreover, with the recent clinical introduction of Fc engineered antibodies and the focus of Fc enhancement of therapeutic antibodies in clinical development pipelines, testing of an affinity-enhanced antibody in a mouse FcγR network where the receptor to which affinity has been enhanced is absent has little value.

Taken together with the enormous amount of time and money required for the clinical development and testing of new antibody therapeutics, a better mouse model for preclinical efficacy testing is needed. This mouse model should better predict clinical outcomes to more rapidly and efficiently determine whether an antibody will succeed in the clinic, or whether it should be modified or abandoned.

Recently, a mouse expressing the human FcγRs in lieu of the mouse FcγRs has been created and characterized (80). This mouse contains each of the individual hFcγR transgenes (hFcγRI, hFcγRIIA^{R131}, hFcγRIIB^{I232}, hFcγRIIIA^{F158}, and hFcγRIIIB) under the control of their endogenous promoters and regulatory elements (80,83-85). Each hFcγR is expressed at biological mRNA and protein levels and has been shown to accurately recapitulate the human cellular expression pattern of hFcγRs on mouse leukocytes (80,83-85). This mouse model has proven to be a critical tool for the evaluation and study of wild type (WT) and Fc engineered hIgGs in models of infectious disease (86-88) and syngeneic tumor therapy (80). These studies have demonstrated the usefulness of testing therapeutic neutralizing and anti-cancer antibodies in this human FcγR model, respectively.

However, this model is fully immunocompetent, with no ability to engraft human cancers. Immunodeficiency is often required for a successful mouse model for testing anti-cancer therapies due to the allowance for xenografting of human cancer cell lines and primary human tumors into immunodeficient animals. This is especially important for cancer therapeutic antibodies since many are designed to human-specific epitopes that are not shared by mice. Furthermore, the transgenic expression of human antigenic targets in mouse cancers does not reflect the native expression levels of the target protein, and in some cases, is very technically challenging.

Therefore, we created new immunodeficient mouse strains for human cancer xenografting that express all or combinations of the human FcγR repertoire in the absence of mouse FcγRs, called RHuFR mice. These mice recapitulate the pattern of human FcγR expression among the various leukocyte populations and are functionally intact. Furthermore, the single and combination human FcγR "knockout" mice are useful tools for the identification of human FcγRs responsible for antibody activity and thus, mechanism of action, as seen in a model of antibody-induced idiopathic thrombocytopenia purpura (ITP). These RHuFR mice were able to accurately recapitulate clinical data comparing two anti-CD20 therapeutic antibodies for the treatment of human lymphoma, when a commercially available immunodeficient model expressing mouse FcγRs failed to do so. The data presented here validates the usefulness of these mice for the preclinical screening of therapeutic antibodies for the treatment of human cancer.

Materials and Methods

Generation of immunodeficient human FcγR expressing RHuFR mice

C57Bl/6 Rag2-/- mice were obtained from the Jackson Laboratories (Stock #008449) and bred to C57Bl/6 mouse FcγRI-/- mouse FcγRα-/- mice (Jeffrey Ravetch, Rockefeller University). Upon the generation of triple knockout mice (Rag2-/-, mFcγRI-/-, mFcγRα-/-), these mice were subsequently bred to C57Bl/6 immunocompetent human FcγR expressing mice (mFcγRI-/-, mFcγRα-/-, hFcγRI+, hFcγRIIA^{R131}+, hFcγRIIB^{I232}+, hFcγRIIIA^{F158}+, & hFcγRIIIB+) obtained from Dr. Jeffrey Ravetch (Rockefeller University). Individual and combination human FcγR "knockout" strains were isolated during the breeding process to establish the RHuFR derivative lines described. Genotyping of all mouse progeny was performed by the MSKCC Mouse Genetics Core Facility according to PCR genotyping protocols (80). All mouse husbandry and experimental procedures complied with IACUC guidelines.

Preparation of mouse leukocytes from spleen and blood

Mouse spleens were gently dissociated, passed through a 70μm mesh, and washed in ice cold PBS. Mice were bled using heparinized capillary tubes. Mouse splenocytes and blood samples underwent red blood cell lysis using ACK lysis buffer (Gibco), and cells were then washed and blocked in FACS Buffer (1X PBS + 5% human serum + 0.02% sodium azide) on ice for 15 min.

Generation of bone marrow derived macrophages and dendritic cells

Bone marrow was flushed from mouse femurs and tibias, passed through a 70μm mesh, and washed once with ice cold PBS. For macrophages, bone marrow was resuspended in complete RPMI + 10% FBS media supplemented with 5ng/mL recombinant mouse CSF-1 (Biolegend) and 5ng/mL recombinant mouse IL-3 (R&D Systems) and plated in a sterile 10cm petri dish (non tissue culture treated). On day 1, non-adherent cells were collected and fresh macrophage differentiation media added for a cell concentration of $1x10^6$ cells/mL. Cells were re-plated into new 10cm petri dishes (10mL/plate). 3-4mLs of fresh macrophage differentiation media was added to each plate on day 4, and adherent cells were collected in PBS via cell scraping on day 7. For dendritic cells, bone marrow was resuspended in complete RPMI + 10% FBS media supplemented with 10ng/mL recombinant mouse GM-CSF (Peprotech) and 10ng/mL recombinant mouse IL-4 (Peprotech) and plated at $1x10^6$ cells/mL in 10cm petri dishes (10mL/plate). On day 3, plates were gently swirled, 75% of the media aspirated, and fresh differentiation media added. On day 6, loosely adherent cells were collected. Both bone marrow derived macrophages and dendritic cells were washed in PBS and blocked in FACS Buffer with 5% human serum prior to flow cytometry analysis.

Flow cytometry analysis of mouse leukocytes for mouse and human FcγR expression

Single cell suspensions were stained with predetermined optimal concentrations of each antibody, and samples were analyzed using LSRFortessa (BD Biosciences). The following antibodies (clones) were used for immunophenotyping of mouse leukocytes: anti-CD3ε (145-2C11), anti-B220 (RA3-6B2), anti-CD45 (30-F11), anti-CD11b (M1/70), anti-CD11c (N418), anti-GR-1 (RB6-8C5), anti-NK1.1 (PK136), anti-F4/80 (BM8), and anti-I-A/I-E (M5/114.15.2). The following antibodies (clones) were used for mouse FcγR expression: anti-mFcγRI (X54-5/7.1), anti-mFcγRII/III (2.4G2), and anti-mFcγRIV (9E9). The following antibodies (clones) were used for human FcγR expression: anti-hFcγRI (10.1), anti-hFcγRIIA (IV.3), anti-hFcγRIIB (2B6), anti-hFcγRIIIA/B (3G8), and anti-hFcγRIIIB (1D3). Cell samples were stained with antibody cocktails for 30-45min on ice and washed with FACS buffer prior to analysis. For blood samples, cells were further RBC lysed and fixed with BD FACS Lysing solution (BD Biosciences) prior to washing. For all other samples, DAPI was added for the exclusion of dead cells in analysis.

Western blotting of human FcγRs

Mouse splenocytes were lysed on ice for 30 min using cell lysis buffer (Cell Signaling) according to manufacturer`s extraction protocol. Protein quantitation was done using the Direct Detect Infrared Spectrometer system (EMD Millipore). A total of 30μg of protein was denatured in Laemmli sample buffer (Bio-Rad) at 95°C for 5 minutes and western immunoblotting was performed using 4-15% Mini-PROTEAN TGX gels (Bio-Rad). Transfer was performed using the Trans-Blot Turbo Transfer system (Bio-Rad) onto PVDF membranes. Proteins were detected using the following primary antibodies: anti-hFcγRI (ab140779), anti-hFcγRIIA (ab194937), anti-hFcγRIIIA/B (ab125477), anti-hFcγRIIIB (MAB1597), and anti-β-actin (A5316). Secondary anti-rabbit (170-6515) and anti-mouse (170-6516) HRP-conjugated antibodies were used. Images were acquired by using the Chemidoc MP system (Bio-Rad).

PCR of hFcγRIIB

Total RNA from mouse splenocytes was isolated using the RNeasy Plus Mini Kit (Qiagen) according to manufacturer's extraction protocol. cDNA libraries from RNA extraction of mouse splenocytes were created using qScript cDNA SuperMix (Quanta Biosciences) following the manufacturer's reaction protocol. PCR on 1μg of cDNA samples was performed using *Taq* DNA Polymerase using Standard *Taq* Buffer (New England Biosciences) following manufacturer's PCR protocol. The following primers were used for amplification of hFcγRIIB (Integrated DNA Technologies) with an annealing temp of 55°C:

FWD: 5'-AGACCCTCCCTGAGAAACCAG-3'

Rev: 5'-GACAGGGAGCTTCAGGACTC-3'

PCR products were run on a 2% agarose gel with SYBR Safe (Invitrogen) and imaged using the Chemidoc MP system (Bio-Rad).

Idiopathic thrombocytopenia purpura model

Mice between 8-12 weeks of age were used of both genders (n=3 males and n=3 females). Mice were pre-bled using heparinized capillary tubes for the time 0 time point, and platelet counts were measured using a Hemavet 950 (Drew Scientific). All mice were injected I.V. with 8.5μg of the 6A6 anti-platelet hIgG1 in sterile PBS (80). Subsequent bleeds occurred at 6 hours, 24 hours, 48 hours, and 72 hours for observing platelet depletion and recovery.

Iodine-125 labeling and rituximab and obinutuzumab blood half-life measurements

0.5mCi of the Iodine-125 radionuclide (PerkinElmer) was added to 100μg of each antibody, rituximab (Rituxan, Genentech) and obinutuzumab (Gazyva, Genentech), in PBS. Chloramine-T (Sigma-Aldrich) was added to a final concentration of 100μg/mL and reacted for 1 minute, followed by the addition of sodium metabisulfite (Sigma-Aldrich) at a final concentration of 1mg/mL and reacted for 3 minutes. Labeled antibodies then underwent purification over 10DG desalting columns (Bio-Rad). Reaction efficiency and product recovery was measured using thin layer chromatography with 10% TCA as the solvent. TLC analysis of free versus bound I-125 for both the crude reaction and antibody products measured on a Cobra II Auto-Gamma counter (Packard) using an I-125 protocol allowed for the calculation of antibody concentration and I-125 counts per μg of antibody for each sample. C57Bl/6 Rag2-/- mouse FcγR+ mice, RHuFR mice, and RHuFR^{1-} mice between 8-12 weeks of age were injected I.V. with 100μg trace labeled antibody (97μg cold + 3μg hot) in sterile PBS for both antibodies (n=5 female mice/genotype/antibody). Mice were bled using heparinized capillary tubes at 2 minutes post antibody injection for the total initial counts injected per mouse. Each blood collection tube was preweighed to measure the total grams of blood collected per mouse for each time point. Mice were subsequently bled at 1 hour, 8 hours, 24 hours, 48 hours, and 96 hours. All blood samples were capped, spun down, and read on the Cobra II Auto-Gamma counter. Sample decay was controlled for by counting an aliquot of each antibody injection mixture at each measured time point.

Surface plasmon resonance for measuring antibody-FcγR affinities

All experiments were performed with a Biacore T200 SPR system (Biacore, GE Healthcare) at 25^{o}C in HBS-EP^{+} buffer (10 mM HEPES, pH 7.4; 150 mM NaCl; 3.4 mM EDTA; 0.005% (v/v) surfactant P20). For the comparison of the affinity of rituximab and obinutuzumab for mouse and human FcγRs, recombinant protein G (Life Technologies) was immobilized to the surface of a CM5 sensor chip (GE Healthcare) using amine coupling chemistry at a density of 500 RU. IgG samples (250 nM; rituximab or obinutuzumab) were captured (60 s; 20 μl/min) on the Protein G-coupled surface at a density of 1000-2000 RU and recombinant human or mouse FcγR ectodomains (0.0156 – 2 μM; 1:2 successive dilutions, Sinobiological) were injected sequentially over flowcells of the sensor chip at a flow rate of 20 μl/min. Association time was 60 s followed by a 300-s dissociation step. At the end of each cycle, sensor surface was regenerated with 10 mM glycine, pH 2.0. Background binding to blank immobilized flow cells was subtracted and affinity constants were calculated using BIAcore T200 evaluation software (GE Healthcare) using the 1:1 Langmuir binding model.

Lymphoma therapy study comparing rituximab and obinutuzumab therapy

Male and female RHuFR^{1-} mice and female C57Bl/6 Rag2-/- WT mice between 5-7 weeks of age were whole body sublethally irradiated with 500cGy 3 weeks prior to cancer cell injection. On Day-1, all mice were injected I.P. with a predetermined optimal concentration of anti-NK1.1 (PK136). On Day 0, mice were injected I.V. via tail vein with 10x10^6 Daudi human Burkitt lymphoma cells (luciferase reporter gene+) suspended in sterile PBS. Prior to the onset of therapeutic antibody administration, mice were randomized into 1 of 4 groups (n=4-5 mice/group/gender): untreated, isotype (HuM195 hIgG1), rituximab (Rituxan, Genentech), and obinutuzumab (Gazyva, Genentech). Bioluminescence imaging (BLI) of tumor growth and therapeutic antibody administration began on Day 14. Antibodies were administered twice per week at 100μg/dose I.V. for a total of 3 weeks. For BLI, 2mg/mouse of D-Lucifern (Gold Biotechnology) was injected I.V. immediately prior to imaging on an IVIS Spectrum (PerkinElmer). Imaging was halted on Day 28 due to saturation of signal in untreated groups. Mouse survival was tracked with facial tumor growth of 1cm^3, hind-leg paralysis, or hunched/sluggish as endpoints.

Statistical analysis

All data are shown as means ± SEM, with the exception of the survival curves. All statistical tests were two-sided and performed using R 3.3.1 (R Core Team, Vienna, Austria) using the clinfun and coin packages. Statistical significance is defined as $p<0.05$. No formal multiple-testing adjustments were conducted.

For the antibody-induced thrombocytopenia model, differences between genders were calculated using the area under the curve (AUC) for every mouse between time 0 and 72 hours and compared within genotypes using the Wilcoxon Mann-Whitney test based on permutation testing procedure. The thrombocytopenia models were analyzed separately in the maximum depletion phase and the platelet recovery phase. To test for significant differences between genotypes in maximum platelet depletion achieved at 6 hours post-injection, the Kruskal-Wallis test was performed using permutation testing. If significant differences were noted, pairwise comparisons using the Wilcoxon rank sum test between each genotype was performed using permutation testing. For platelet recovery (time 6 to 72 hours), AUC was normalized to % platelet depletion at maximum ($AUC_{recovery}$/(100 – Platelet % at 6 hours)). This relative AUC was summarized for each mouse to test if significant differences exist between genotypes using the Kruskal-Wallis test with permutation testing. If significant differences were noted, pairwise comparisons between relative AUCs for each genotype were performed using the Wilcoxon rank sum test with permutation testing. Permutation testing procedures were performed using 10,000 permutations.

For quantitation of bioluminescence imaging in the *in vivo* lymphoma therapy model, AUC for each mouse from time 14 to 28 days was used. To test for statistically significant differences between treatment groups within genotypes, a non-parametric permutation test comparing the area under the bioluminescence profile curves was performed using the Kruskal-Wallis test, stratified by gender where applicable, with permutation testing. Since all mice survived until day 28, there was no issue of dependent right censoring. If treatment groups are significantly different, pairwise comparisons between groups using the Wilcoxon rank sum test, stratified by gender where applicable, with permutation testing was performed. Assessments using the Wilcoxon Mann Whitney tests showed that there were no statistically significant differences between genders across genotypes. Analyses were conducted with 5,000 permutations.

For mouse survival in the *in vivo* lymphoma therapy model, overall survival was modeled as number of days between tumor injection and death or censoring using the Kaplan-Meier method for each genotype. Survival curves were compared across treatment groups by the log-rank test, stratified by gender where applicable, based on permutation reference distributions for small sample size (89). Each resampling procedure included 500 permutations. If the overall log-rank test indicated significant differences among groups, subsequent pairwise comparisons were conducted between groups.

Results

Creation and characterization of the RHuFR mice

The breeding scheme depicted in Figure 2 shows the methodology used to create the Rag2-/- Human Fcγ Receptor (RHuFR) mice. Briefly, we began by crossing Rag2-/- mice to mice lacking the mouse FcγRs (mFcγRI-/-, mFcγRα-/-) (80). Using an immunodeficient background, such as Rag2 knockout, allows for the engraftment of human cancer cell lines and primary human cells due to the lack of mature B and T cells, therefore reducing the likelihood of rejection. This allowed us to create an intermediary mouse strain, the Rag2-/-, mFcγRI-/-, mFcγRα-/- (FcγR Null) strain. This immunodeficient, mouse FcγR deficient model is used as a negative control for characterization of the other strains. In addition, it can be a useful tool to determine the extent to which a therapeutic antibody relies on Fcγ receptor engagement for activity. This strain was thoroughly characterized for the loss of all mouse FcγR expression on the leukocyte populations in direct comparison to the parental Rag2-/- strain (Figure 3). The immunodeficient FcγR Null strain was then crossed to the immunocompetent mouse model expressing all of the human FcγRs in lieu of the mouse FcγRs (80). This immunocompetent mouse model contains each of the individual hFcγR transgenes (hFcγRI, hFcγRIIA^{R131}, hFcγRIIB^{I232}, hFcγRIIIA^{F158}, & hFcγRIIIB) under the control of their endogenous promoters and regulatory elements and has been thoroughly characterized (80,83-85). After many rounds of breeding and backcrosses, we were able to create mice expressing all of the human FcγR transgenes in the Rag2-/-, mouse FcγR null background, known as the RHuFR mouse. We validated the expression of each of

FIGURE 2

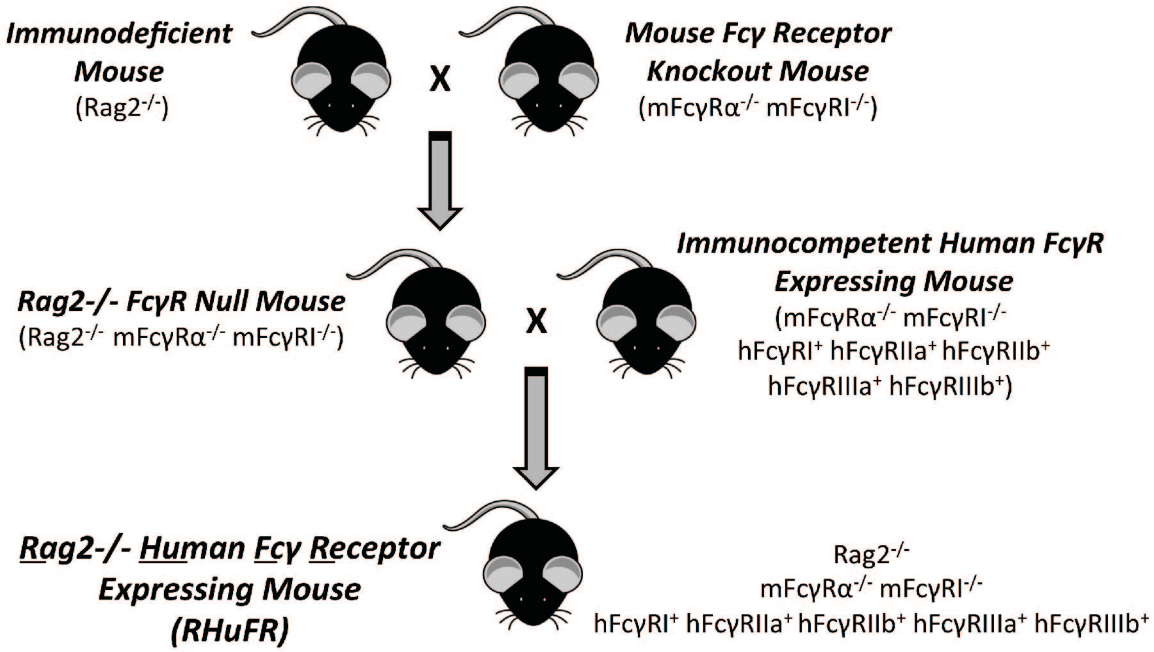

Figure 2: Creation of the novel immunodeficient human FcγR+ RHuFR mouse. This breeding scheme was used to create the immunodeficient human FcγR-only expressing RHuFR mice. Rag2-/- mice lacking one or more human FcγRs were isolated during this breeding to establish the RHuFR "knockout" strains.

FIGURE 3

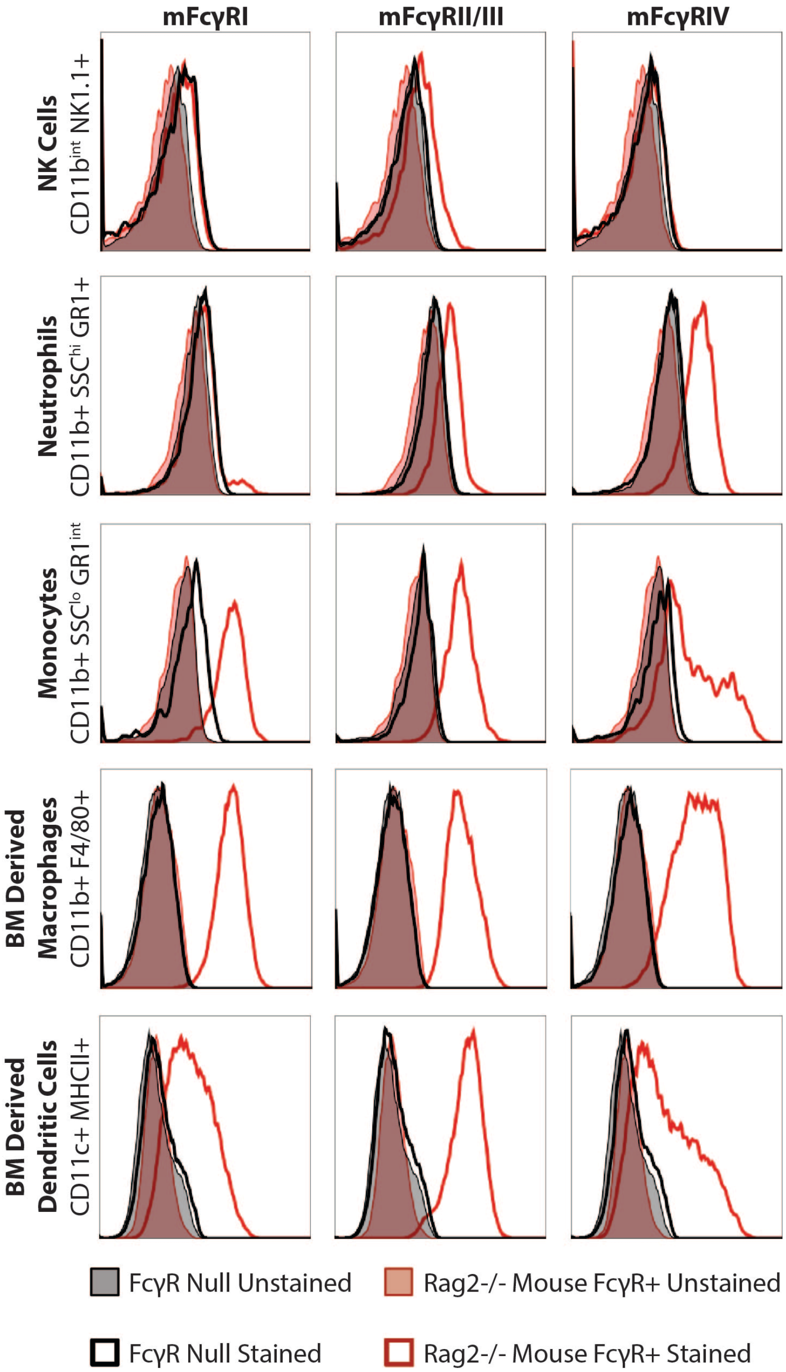

Figure 3: Loss of mouse FcγR expression on mouse leukocytes in the Rag2-/- FcγR Null mouse. Representative flow cytometry analyses of mouse leukocyte populations from parental Rag2-/- (red) and Rag2-/- FcγR Null mice (black) (n=3). Unstained samples are shaded and mFcγR stained samples are lines.

the human FcγRs on the mouse leukocyte populations in the RHuFR mouse to ensure expression of the receptors mimics the expression observed in humans (Figure 4).

This analysis demonstrated the exclusive expression of hFcγRIIIA on the NK cells in the RHuFR mouse. RHuFR neutrophils appear to express all the human FcγRs. However, since the antibody for hFcγRIIIA also detects hFcγRIIIB, it is likely that the positive signal seen here is due to the detection of the hFcγRIIIB since it is strongly expressed by this cell population. Meanwhile RHuFR blood-derived monocytes express hFcγRI, IIA, and IIB. It also appears that some of the express hFcγRIIIA, while others do not. This is consistent with what is observed in humans (82). Bone marrow (BM) derived macrophages from the RHuFR mice express hFcγRI, IIA, IIB, and IIIA, while BM derived dendritic cells express hFcγRIIA and hFcγRIIB, as expected. These direct comparisons between what is observed in the RHuFR mice and what is known for the expression of FcγRs in humans (90) is summarized in Table 2.

While breeding the RHuFR mouse, mice lacking each of the individual hFcγRs, or mice lacking hFcγRI in combination with each of the other hFcγRs were isolated and used to establish single and combination RHuFR "knockout" derivative strains (Table 3). These individual and combination hFcγR "knockout" strains were created in order to potentially probe the separate role of each receptor in therapeutic antibody activity, both in the presence and absence of hFcγRI. The reason for choosing combination deficiencies in the hFcγRI "knockout" background is due to the lack of circulating Ig in this model caused by Rag2 deficiency and loss of mature B cells. Since hFcγRI is the only high affinity FcγR capable of binding monomeric soluble IgG, while the other receptors bind

FIGURE 4

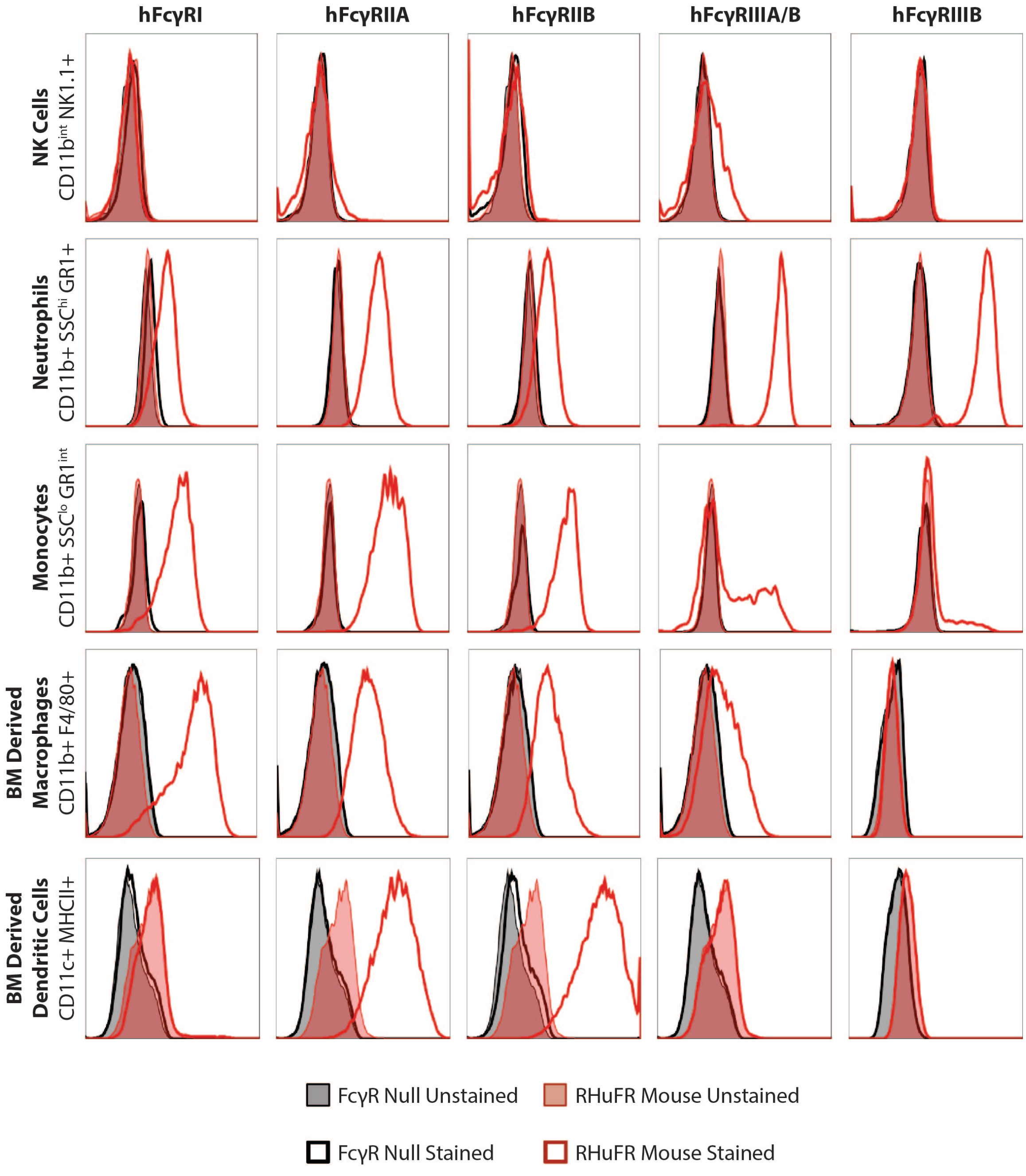

Figure 4: The RHuFR mice recapitulate human FcγR expression patterns on mouse leukocytes. Representative flow cytometry analyses performed on mouse effector leukocyte populations (NK cells, neutrophils, monocytes, bone marrow (BM) derived macrophages, an BM derived dendritic cells) from the FcγR Null (black) and RHuFR (red) mice (n=3). Unstained samples are shaded and hFcγR stained samples are lines.

TABLE 2

	hFcγRI		hFcγRIIA		hFcγRIIB		hFcγRIIIA		hFcγRIIIB	
	Human	RHuFR	Human	RHuFR	Human	RHuFR	Human	RHuFR	Human	RHuFR
NK cells	-	-	-	-	-	-	+	+	-	-
Neutrophils	(+)	+	+	+	+	+	-	-	+	+
Monocytes	+	+	+	+	+	+	+/-	+/-	-	-
Macrophages	+/-	+	+	+	+	+	+	+	-	-
Dendritic Cells	-	-	+	+	+	+	-	-	-	-

Table 2: Human FcγR expression in human versus RHuFR mouse leukocytes. A table summarizing the expression of human FcγRs on human immune cells and on the RHuFR mouse immune cell populations. + indicates receptor expression, - indicates lack of receptor expression, (+) indicates inducible expression, +/- indicates expression on some, but not all, cellular subsets.

TABLE 3

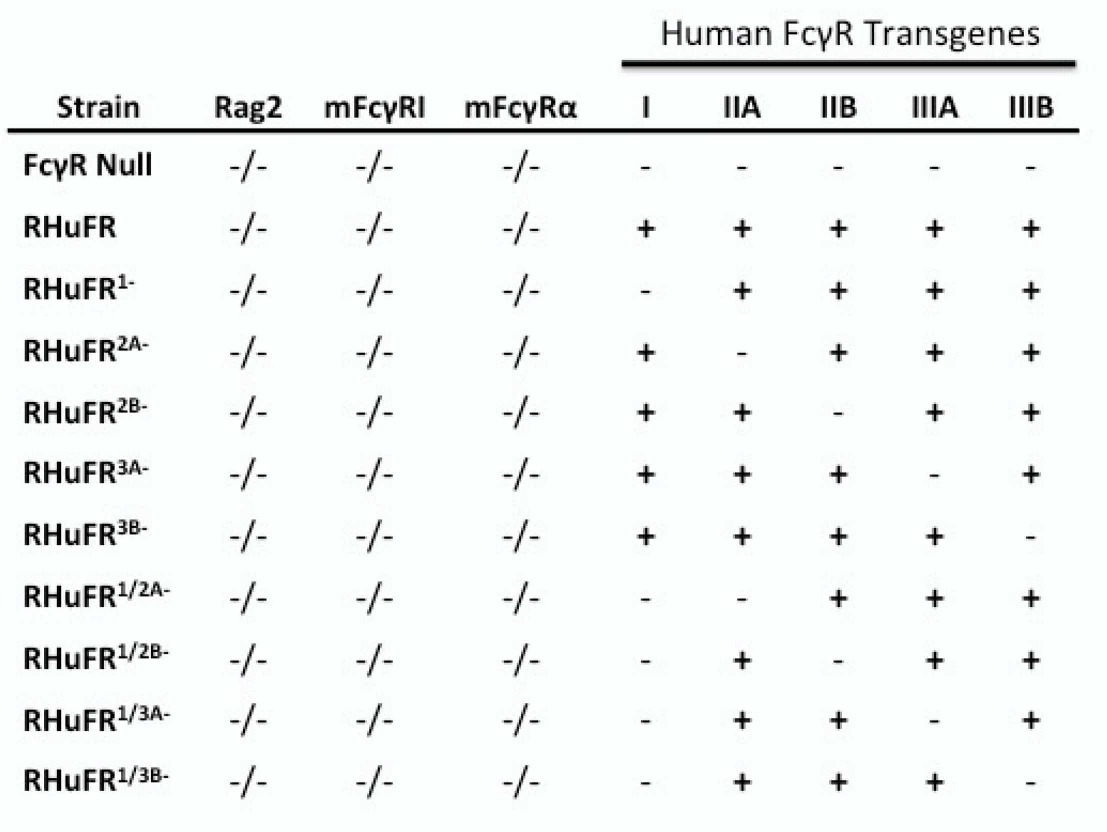

				Human FcγR Transgenes				
Strain	**Rag2**	**mFcγRI**	**mFcγRα**	**I**	**IIA**	**IIB**	**IIIA**	**IIIB**
FcγR Null	-/-	-/-	-/-	-	-	-	-	-
RHuFR	-/-	-/-	-/-	+	+	+	+	+
RHuFR^{1-}	-/-	-/-	-/-	-	+	+	+	+
RHuFR^{2A-}	-/-	-/-	-/-	+	-	+	+	+
RHuFR^{2B-}	-/-	-/-	-/-	+	+	-	+	+
RHuFR^{3A-}	-/-	-/-	-/-	+	+	+	-	+
RHuFR^{3B-}	-/-	-/-	-/-	+	+	+	+	-
RHuFR$^{1/2A-}$	-/-	-/-	-/-	-	-	+	+	+
RHuFR$^{1/2B-}$	-/-	-/-	-/-	-	+	-	+	+
RHuFR$^{1/3A-}$	-/-	-/-	-/-	-	+	+	-	+
RHuFR$^{1/3B-}$	-/-	-/-	-/-	-	+	+	+	-

Table 3: Summary of novel RHuFR mice genotypes. Genotypes of all 11 novel strains of mice created in this report are listed with name of the mouse strain and genes of interest across the columns and each mouse strain per row. The first row is the FcγR Null mouse, an immunodeficient (Rag2-/-), mouse FcγR deficient model used as a negative control for characterization of the other strains. The second row in the table is the Rag2-/- human FcγR+ RHuFR mouse expressing all five human receptors in the absence of the mouse FcγRs. Rows 3-7 are the RHuFR "knockout" strains isolated during breeding that lack one of the five human FcγRs (1-, 2A-, 2B-, 3A-, and 3B-) in the context of Rag2 and mFcγR deficiency. The last four rows (8-11) are the combination "knockout" RHuFR mice that lack hFcγRI in combination with one of the other human FcγRs (1/2A-, 1/2B-, 1/3A-, and 1/3B-). -/- indicates homozygous gene knockout, - represents absence of the transgene, + represents presence of the transgene.

immune complexes, it is possible it can interfere with therapeutic antibodies in the Rag2-/- background by acting as an antibody sink.

Once each of the individual hFcγR “knockout” strains were established (RHuFR^{1-}, RHuFR^{2A-}, RHuFR^{2B-}, RHuFR^{3A-}, and RHuFR^{3B-}), characterization of their human FcγR expression pattern on mouse leukocytes was also performed to confirm presence of all the human receptors except the single “knockout” receptor. The RHuFR^{1-} mouse demonstrated the lack of human FcγRI expression on the neutrophils, monocytes, and BM derived macrophages populations as compared to the RHuFR mice, while maintaining appropriate expression of all other human FcγRs on respective effector populations (Figure 5).

In the RHuFR^{2A-} mice (Figure 6), the loss of human FcγRIIA expression on neutrophils and BM derived macrophages was clear. However, for monocytes and BM derived dendritic cells, hFcγRIIA staining was decreased but not absent. Even though this antibody is selective for binding human FcγRIIA, cross-recognition of the hFcγRIIB receptor by this antibody is feasible, especially in the cells expressing high amounts of hFcγRIIB, which is the case for monocytes and dendritic cells. In the RHuFR^{2B-} mice (Figure 7), human FcγRIIB expression is absent on the neutrophil, monocyte, and BM derived macrophage and dendritic cell populations as expected. However, the staining of the hFcγRIIA antibody in these populations is also slightly reduced compared to the RHuFR mice, confirming that indeed, this antibody can bind both receptors. All other human FcγR expression patterns are maintained RHuFR^{2A-} and RHuFR^{2B-} mice.

FIGURE 5

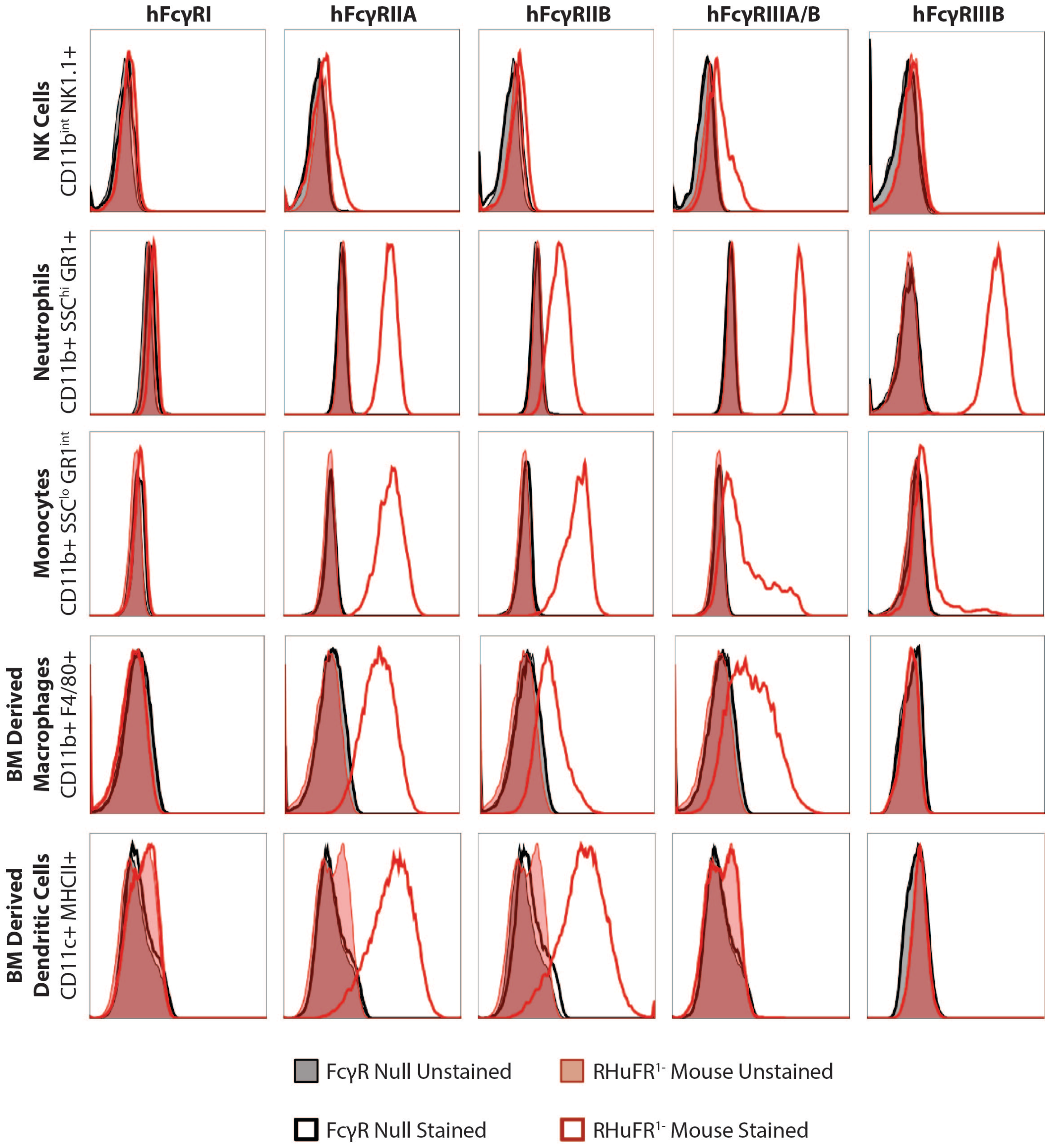

Figure 5: Characterization of RHuFR^{1-} mouse. Representative flow cytometry analyses of effector leukocyte populations from RHuFR^{1-} (red) and FcγR Null mice (black) (n=3). Unstained samples are shaded while human FcγR stained samples are lines.

FIGURE 6

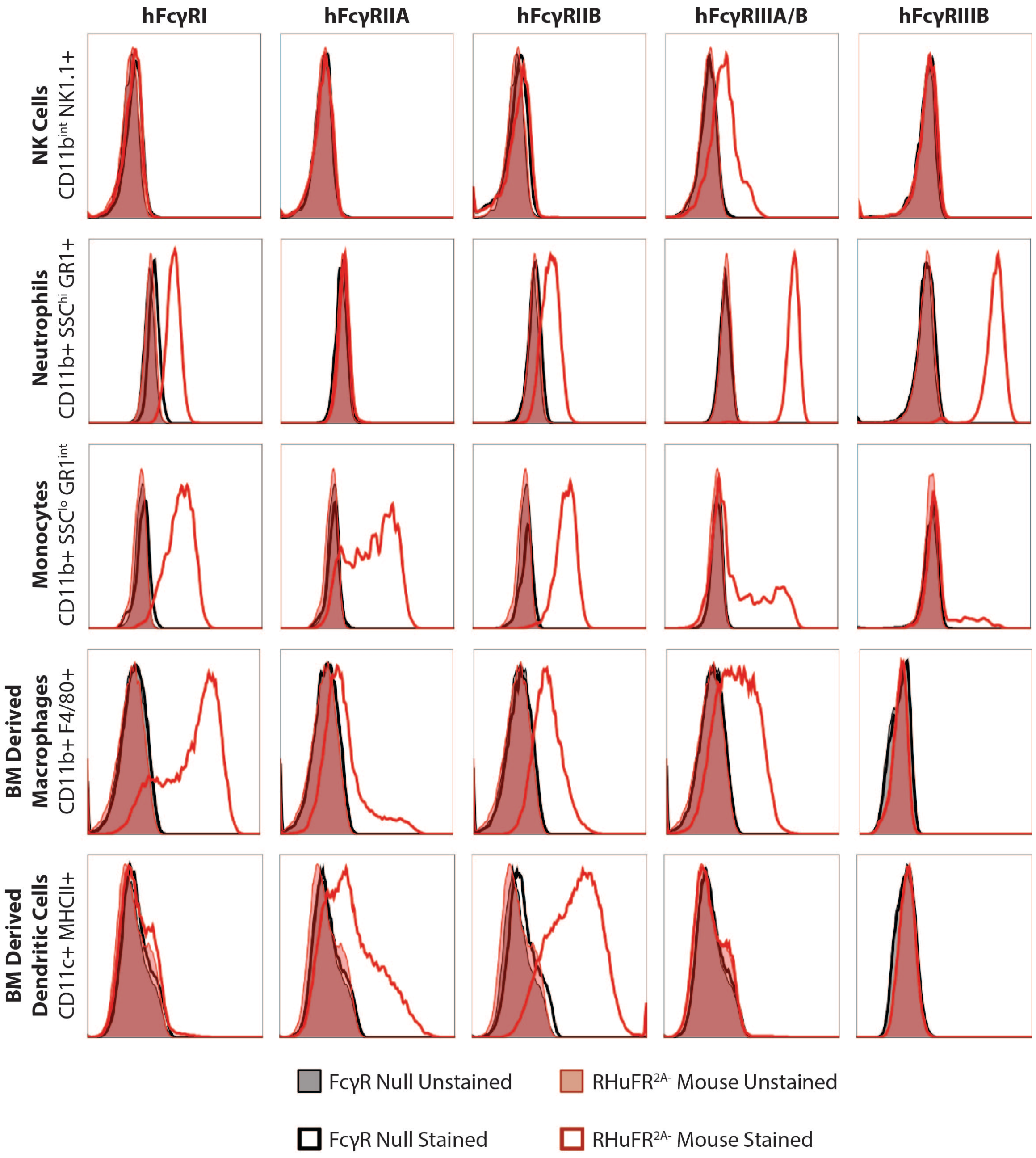

Figure 6: Characterization of RHuFR^{2A-} mouse. Representative flow cytometry analyses of effector leukocyte populations from RHuFR^{2A-} (red) and FcγR Null mice (black) (n=3). Unstained samples are shaded while human FcγR stained samples are lines.

FIGURE 7

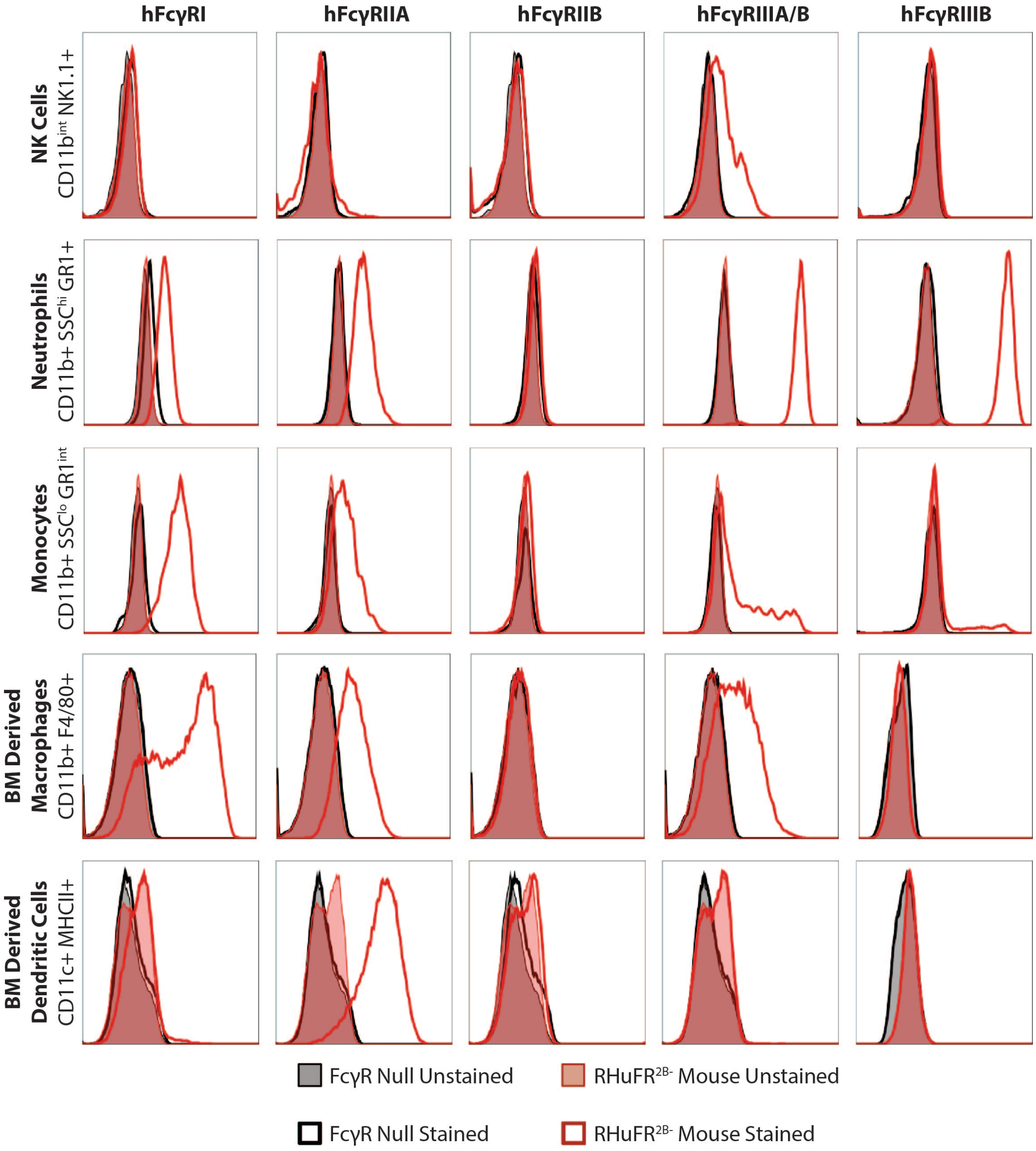

Figure 7: Characterization of RHuFR^{2B-} mouse. Representative flow cytometry analyses of effector leukocyte populations from RHuFR^{2B-} (red) and FcγR Null mice (black) (n=3). Unstained samples are shaded while human FcγR stained samples are lines.

In the RHuFR^{3A-} mice (Figure 8), human FcγRIIIA/B antibody staining on the NK cell and the BM derived macrophage populations is not observed, confirming the presence of the hFcγRIIIA receptor on these cells. No loss in hFcγRIIIA/B antibody signal is observed for the neutrophil population in the RHuFR^{3A-} mice, suggesting that the positive signal is due to hFcγRIIIB expression. This is confirmed by the strong hFcγRIIIB antibody staining. However, the hFcγRIIIA/B antibody signal is still present for the monocyte population. This is abnormal since there is little to no hFcγRIIIB antibody binding in this population.

Furthermore, in the RHuFR^{3B-} mice (Figure 9), there is an obvious lack of hFcγRIIIA/B and hFcγRIIIB antibody binding on neutrophil and monocyte populations. For the neutrophils, this re-confirms the expression of hFcγRIIIB in lieu of hFcγRIIIA on this population, mimicking what is observed on human neutrophils. For the monocytes, it is possible that blood derived RHuFR monocytes do not express either human FcγRIIIA or FcγRIIIB, but that the positive signal observed for the hFcγRIIIA/B antibody in the RHuFR mice is contamination of the monocyte gate with neutrophils due to the unavoidable closeness of gating between the two populations. However, this is unlikely since the hFcγRIIIB antibody signal would be much stronger if the positive hFcγRIIIA/B antibody signal in the monocyte gate was indeed contamination from neutrophils. On the other hand, it may be that the monocytes do express hFcγRIIIA in all of the other RHuFR mice except RHuFR^{3B-} since they stain positive for the hFcγRIIIA/B antibody and not the hFcγRIIIB antibody in these other strains. All other human FcγR expression patterns are maintained for the RHuFR^{3A-} and RHuFR^{3B-} mice when compared to the RHuFR mice.

FIGURE 8

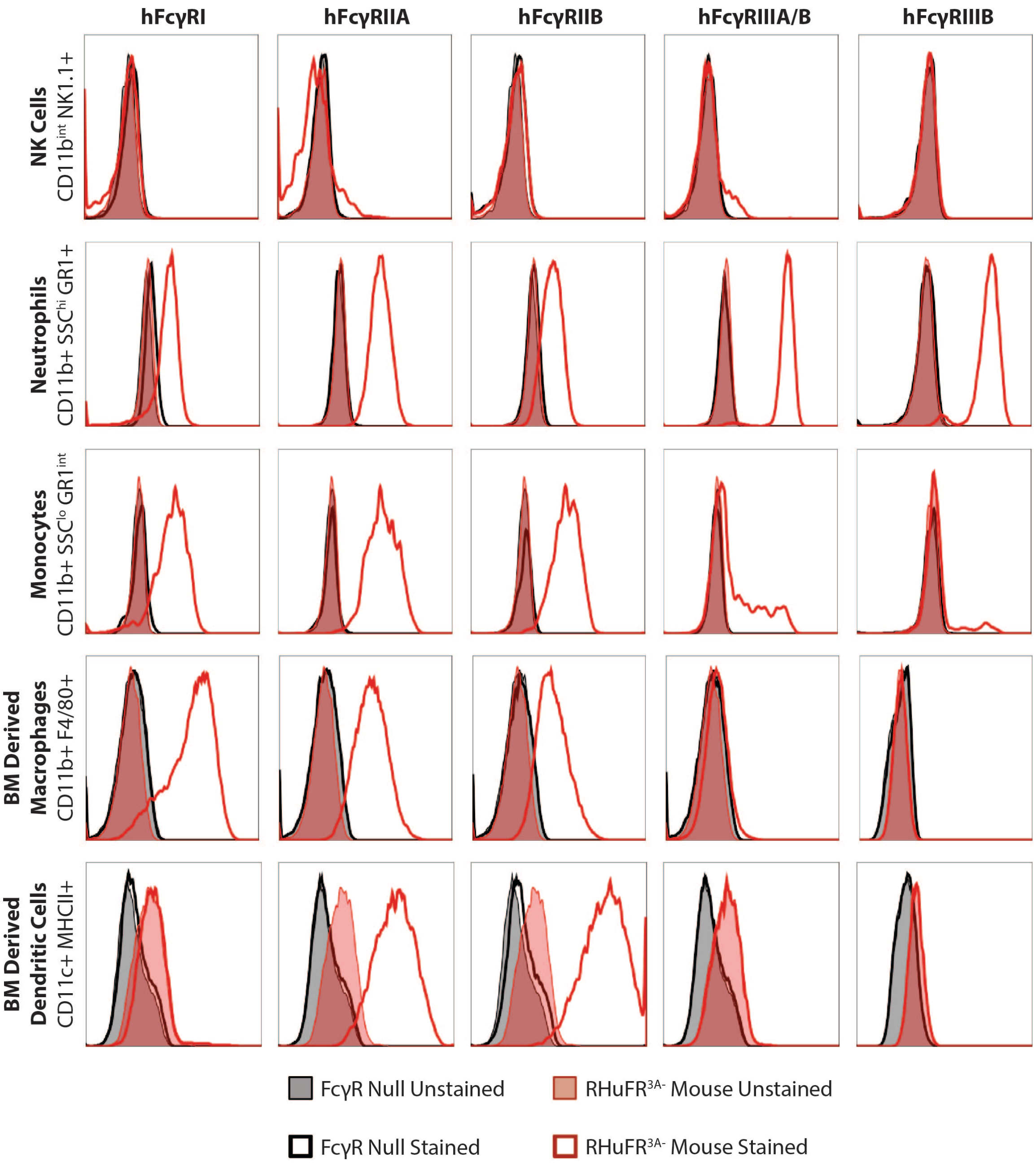

Figure 8: Characterization of RHuFR^{3A-} mouse. Representative flow cytometry analyses of effector leukocyte populations from RHuFR^{3A-} (red) and FcγR Null mice (black) (n=3). Unstained samples are shaded while human FcγR stained samples are lines.

FIGURE 9

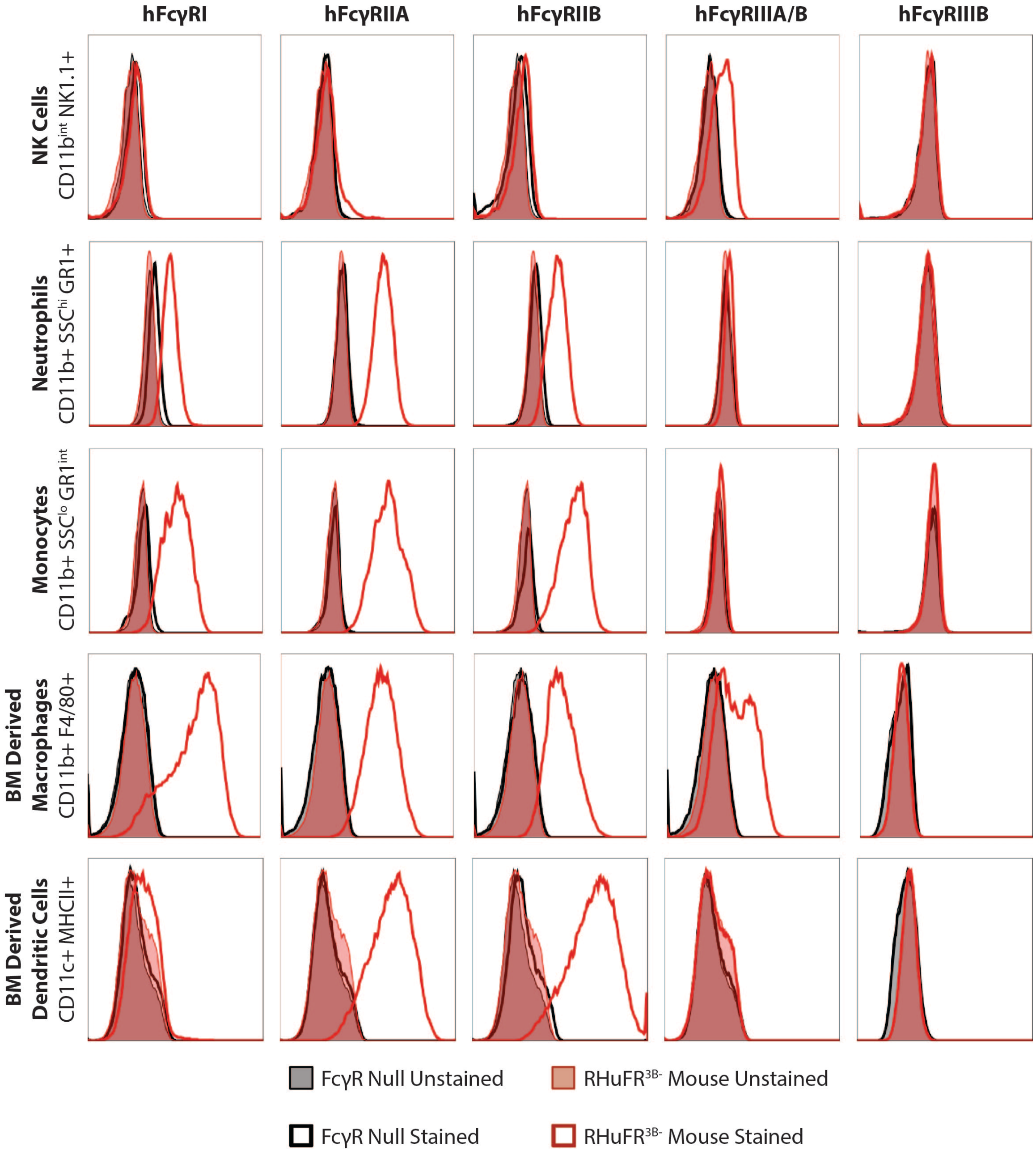

Figure 9: Characterization of RHuFR^{3B-} mouse. Representative flow cytometry analyses of effector leukocyte populations from RHuFR^{3B-} (red) and FcγR Null mice (black) (n=3). Unstained samples are shaded while human FcγR stained samples are lines.

In addition to cell surface expression, the expression or absence of each human FcγR in the new RHuFR mouse strains was assessed by western blot or PCR (Figure 10). Western blot and PCR was performed on whole mouse splenocytes from RHuFR, FcγR Null, $RHuFR^{1-}$, $RHuFR^{2A-}$, $RHuFR^{2B-}$, $RHuFR^{3A-}$, and $RHuFR^{3B-}$ mice. Since there was not a good antibody available for hFcγRIIB, PCR was used instead to confirm the presence or absence of expression of this receptor. The RHuFR mouse has positive signal for all human FcγR antibodies (I, IIA, IIIA, and IIIB), while the FcγR Null shows a lack of signal, confirming expression and absence, respectively. Each hFcγR "knockout" RHuFR derived strain lacks their respective receptor. Meanwhile, PCR for the human FcγRIIB transcript shows a lack of hFcγRIIB mRNA for the $RHuFR^{2B-}$ mouse, with appropriate signal for the RHuFR mouse and all other derivative "knockout" strains.

Lastly, in order to ensure that all of the RHuFR mice can be xenografted with human cancers, we confirmed the lack of circulating B and T cells in these mice (Figure 11). This was done by probing for B220 (B cells) and CD3 (T cells) expressing cells in blood leukocytes from mice that are Rag2+/- and comparing the presence or absence of these sample populations in a control Rag2-/- mouse. We then looked for these populations in the blood leukocytes of the Rag2-/- FcγR Null mouse, RHuFR mouse, and RHuFR single "knockout" mice. All new mouse strains tested showed a complete loss of these mature circulating B and T cell populations.

FIGURE 10

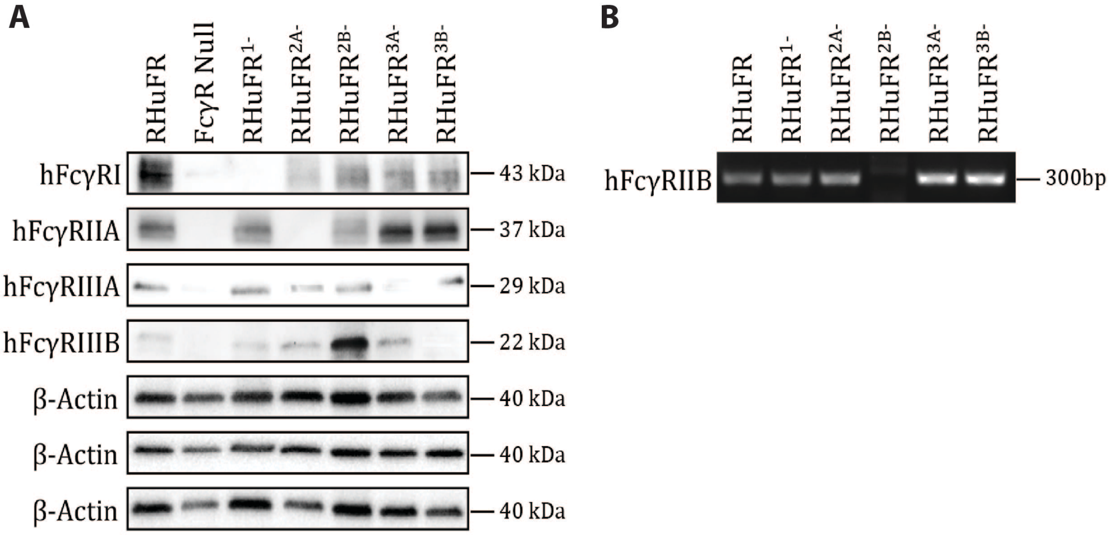

Figure 10: Western blot and PCR analysis of human FcγR expression. A) Western blot of mouse splenocytes from RHuFR, FcγR Null, RHuFR^{1-}, RHuFR^{2A-}, RHuFR^{2B-}, RHuFR^{3A-}, and RHuFR^{3B-} mice using antibodies to hFcγRI, hFcγRIIA, hFcγRIIIA, hFcγRIIIB, and mouse β-actin as a loading control. The RHuFR mouse has positive signals for all human FcγR antibodies, while the FcγR Null shows a lack of signal, confirming expression and absence, respectively. Each hFcγR deficient RHuFR derivative strain lacks their respective receptor. Human FcγRIIB could not be specifically probed by western blot due to a lack of a good antibody. **B)** PCR analysis on mouse splenocytes cDNA for human FcγRIIB shows a lack of transcript for the RHuFR^{2B-} mouse, with appropriate signal for the RHuFR mouse and all other “knockout” strains.

FIGURE 11

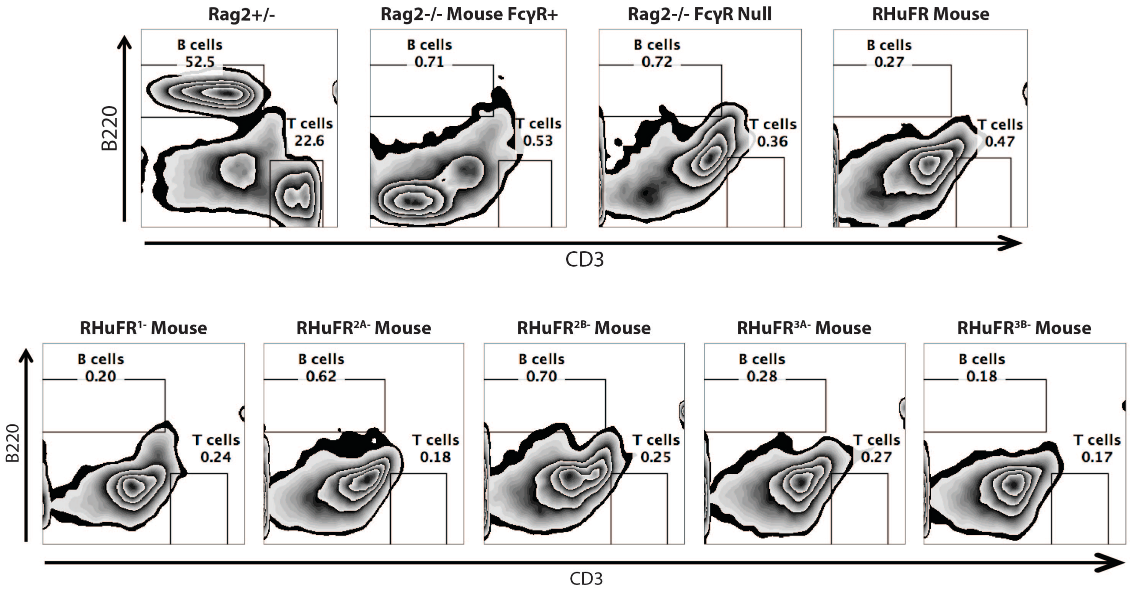

Figure 11: B and T cell loss in Rag2-/- FcR Null, RHuFR, and RHuFR "knockout" mice. Flow cytometry gating on B and T cells in Rag2+/- mice and loss of the B and T cell populations in parental Rag2-/- mouse FcγR+, Rag2-/- FcγR Null, RHuFR, RHuFR^{1-}, RHuFR^{2A-}, RHuFR^{2B-}, RHuFR^{3A-}, and RHuFR^{3B-} mice (n=2 per genotype).

Testing the functional capacity of the RHuFR mice in a model of antibody-induced idiopathic thrombocytopenia purpura

In order to determine whether or not the reconstituted human FcγR network remained functional in order for the RHuFR mice to mediate ADCC, a model of antibody-induced idiopathic thrombocytopenia purpura (ITP) was employed. The ITP model acts as a surrogate for *in vivo* antibody-dependent cytotoxicity by employing an anti-platelet hIgG1 that results in acute depletion of blood platelets in an FcγR dependent manner. This model for the functional testing of ADCC in mice was used for the initial characterization of the immunocompetent human FcγR expressing mice previously developed (80). Other functional models were used to evaluate this mouse, such as the depletion of B and T cells from circulation. However, due to the lack of B and T cells in our RHuFR mice due to Rag2 deficiency, the ITP model is the only congruent model to validate functionality of the human FcγR network in our mice.

Upon administration of an anti-platelet antibody (6A6 hIgG1) to Rag2-/- mice expressing the native mouse FcγRs, more than 85% depletion of original platelet numbers is observed 6 hours post antibody administration, the time point at which maximum platelet depletion is achieved (Figure 12). Meanwhile, the Rag2-/- FcγR null model only experienced a 25% reduction in platelet counts, representing non-FcγR mediated platelet loss. In the RHuFR mice, ~65% depletion of platelets was observed, consistent with reported numbers for the immunocompetent human FcγR expressing mice (80). This suggests that the introduction of Rag2 deficiency does not interfere with FcγR mediated function in these animals and that FcγR function has been maintained from the parental immunocompetent human FcγR expressing mice.

FIGURE 12

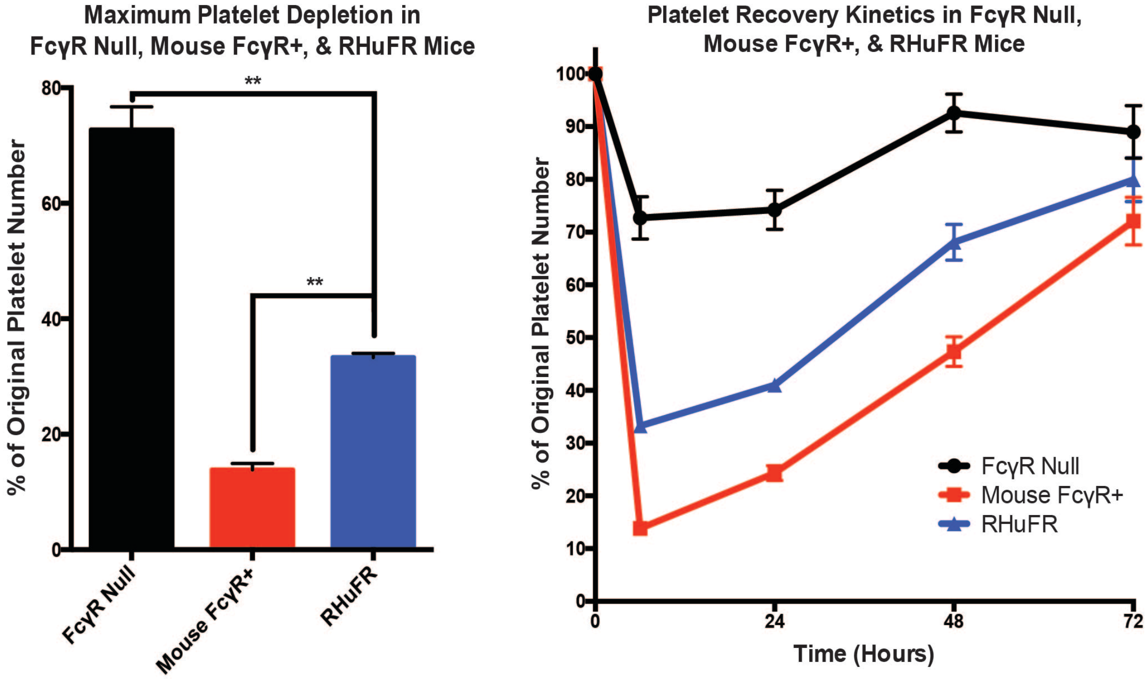

Figure 12: RHuFR mice successfully deplete platelets in an antibody-induced model of ITP. The left bar graph shows the average percentage of retained platelets (normalized to time 0 platelet count for each mouse) at 6 hours (time of maximum platelet depletion) post injection of the anti-platelet 6A6 hIgG1 antibody. The Rag2-/- FcγR Null (black), Rag2-/- mouse FcγR+ (red), and RHuFR (blue) mice are compared (n=3 males and 3 females), with no observed significant differences in gender within genotypes. The RHuFR mouse had ~65% platelet depletion, which is statistically different compared to the FcγR Null and mouse FcγR+ mice ($p<0.0045$ and $p<0.0058$ respectively). The right line graph depicts mean platelet recovery kinetics from maximum depletion (6hr). The rates of recovery of platelets for all mice are not statistically different.

Of note, both the RHuFR mice and immunocompetent human FcγR expressing mice consistently show a lower degree of platelet depletion in this ITP model than either the commercially available Rag2-/- or WT C57Bl/6 mouse FcγR+ mice, respectively (80). This suggests that for this ITP model, the interaction of the 6A6 hIgG1 with mouse platelets and the mouse FcγR network is more efficient at inducing platelet loss from the circulation via ADCC than when there is a human FcγR network present. This may be due to the FcγR expression patterns of the mouse leukocytes in the mouse versus human FcγR expressing mice. It may also indicate that this model relies on the clearance of platelets by effector cells coexpressing activating and inhibitory FcγRs, where activation is directly correlated to the antibody's A/I ratio. For a hIgG1, the threshold for activation of these cells in a mouse FcγR system is much lower due to its higher A/I ratio, while in a human FcγR system this threshold is higher due to a lower A/I ratio (79). This would explain the ability of the mouse FcγR network to have enhanced activity in this ITP model.

We then wanted to test the functional capacity of our RHuFR derived individual human FcγR "knockout" lines (RHuFR^{1-}, RHuFR^{2A-}, RHuFR^{2B-}, RHuFR^{3A-}, and RHuFR^{3B-}) in this model of antibody induced ITP. This will allow us to begin to understand the human FcγR network redundancies and potential antibody-mediated mechanisms of action. Therefore, platelet loss in mice with *single human FcγR "knockouts"* was measured and compared directly to the RHuFR mouse (Figure 13). The RHuFR^{2B-} strain was not characterized in this ITP model due to a lack of availability of age-matched mice in the Rag2-/- background at the time of these experiments. Loss of human FcγRI, FcγRIIIA, and FcγRIIIB resulted in little to no variation in platelet

FIGURE 13

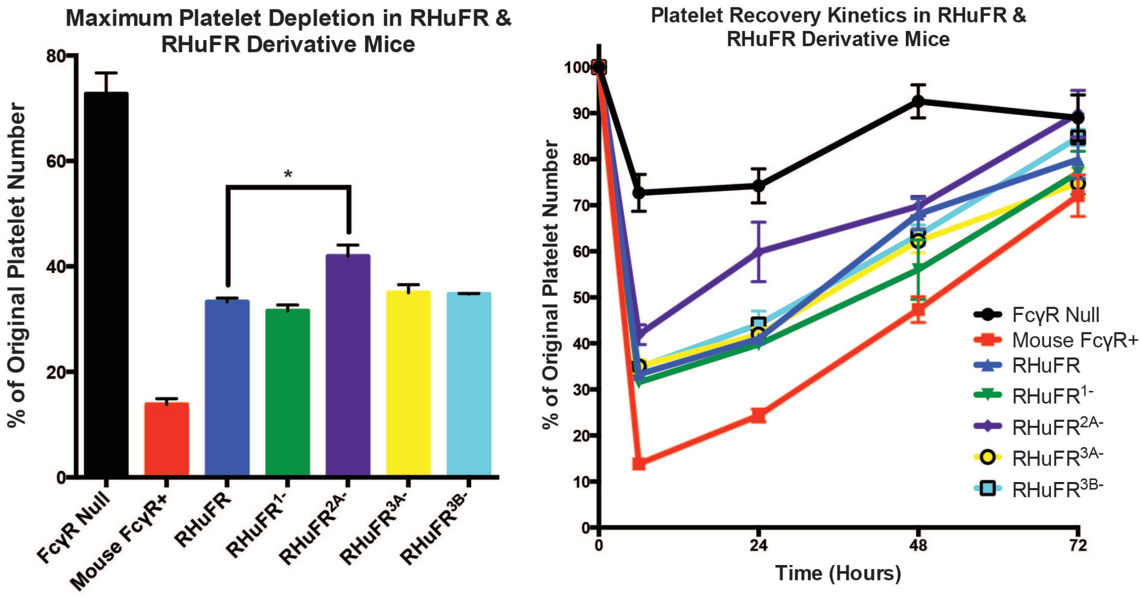

Figure 13: The RHuFR single "knockout" mice are functionally intact. Comparison of maximum platelet depletion (left bar graph) and platelet recovery kinetics (right line graph) for each single human FcγR "knockout" RHuFR derivative strain (n=3 males and 3 females) compared to the RHuFR mouse. No significant differences between genders within genotypes were observed. RHuFR^{2A-} mice showed a slight reduction in platelet depletion (~55% depletion) with $p<0.0201$ compared to RHuFR mice. Platelet recovery kinetics for all RHuFR single "knockout" mice were similar with no significant differences.

depletion or platelet recovery kinetics when compared to RHuFR mice. However, RHuFR^{2A-} mice showed a small but significant reduction in platelet clearance when compared to the parental RHuFR mice (~55%), but no change in the kinetics of platelet recovery. This suggests that the RHuFR derived single "knockout" strains retain their functional capacity in this model, and that the human FcγR network is highly redundant. It also may suggest a role for hFcγRIIA in platelet loss from circulation in this antibody-induced ITP model.

In order to explore the functional capacity of the RHuFR^{1-} *combination "knockout"* mice—mice that lack hFcγRI in addition to one of the other human FcγRs—, these strains were also studied in this model of ITP (Figure 14). Compared to RHuFR^{1-}, maximum platelet loss does not vary for RHuFR$^{1/2B-}$ or RHuFR$^{1/3B-}$ mice, with a slight but significant decrease for RHuFR$^{1/3A-}$ mice. More interestingly, the RHuFR$^{1/2A-}$ mice show a large reduction in platelet clearance (~35% platelet depletion) compared to RHuFR^{1-} mice, which suggests that hFcγRI loss augments the phenotype observed for the RHuFR^{2A-} mice. Since mouse platelets express hFcγRIIA (80), this trend suggests immune complex formation via platelet hFcγRIIA engagement, similar to that observed in heparin-induced thrombocytopenia, and a subsequent role of hFcγRI in immune complex clearance in this antibody-induced model. Meanwhile, the kinetics of platelet recovery for the RHuFR$^{1/2B-}$ and RHuFR$^{1/3B-}$ mice increase significantly from RHuFR^{1-} mice, but the mechanism for this enhanced recovery remains unclear. Taken together, this data highlights 1) the redundancy of the human FcγR network with effector leukocytes able to engage other FcγRs when one receptor is lost, 2) the intricate and complex web of

FIGURE 14

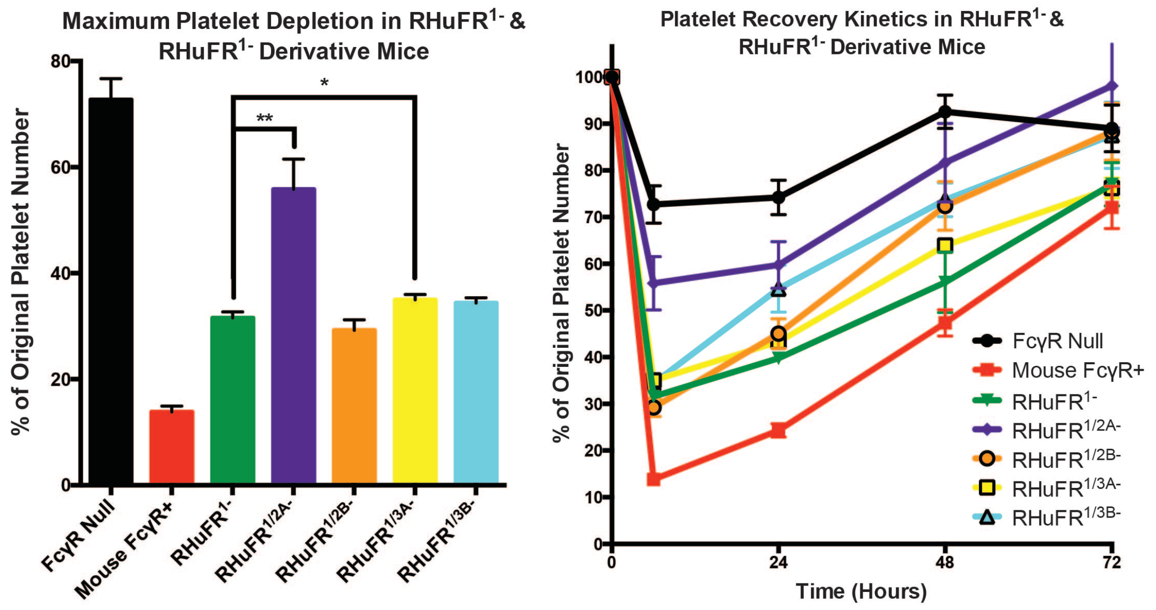

Figure 14: The combination RHuFR "knockout" mice reveal potential mechanisms of action for platelet depletion in an antibody-induced model of ITP. Maximum platelet depletion (left, bar graph) and platelet recovery kinetics (right, line graph) for the combination RHuFR "knockout" mice, or RHuFR^{1-} derived, mice (n=3 males and 3 females) compared to RHuFR^{1-} mice. No significant differences between genders within genotypes were observed. RHuFR$^{1/3A-}$ mice demonstrated a slight reduction in platelet loss at maximum ($p<0.0478$), while RHuFR$^{1/2A-}$ showed a robust reduction in platelet clearance (~35% depletion) when compared to RHuFR^{1-} mice ($p<0.0054$). Platelet recovery for RHuFR$^{1/2B-}$ and RHuFR$^{1/3B-}$ mice was significantly faster than observed platelet recovery in the RHuFR^{1-} mice ($p<0.0064$ and $p<0.0052$ respectively).

interactions between these receptors, the cells they are expressed on, and the antibody-bound target, and 3) a potential key role for hFcγRIIA in antibody-induced thrombocytopenia. Understanding these results in full is out of the scope of this project, but can yield enlightening results on the human FcγR network biology, as well as a better understanding of platelet biology and ITP pathogenesis.

Importantly, functional analysis in this antibody-induced model of ITP was performed in equal numbers of mice of both genders, male and female, for all genotypes tested. No statistical differences between genders for any of the described mouse genotypes, including all RHuFR and RHuFR single and combination "knockout" strains, were observed for functional capacity in platelet loss. This allows us to use both genders in our experimental models without concern for gender specific differences. Overall, this model of antibody-induced thrombocytopenia highlights the complexity and redundancy of the human FcγR network, as well as the potential for these single and combined RHuFR "knockout" mice to reveal potential antibody mechanisms of action.

Therapeutic human cancer antibody testing in the RHuFR mice

In order to demonstrate the clinical relevance of the new RHuFR mice as a model to study therapeutic antibodies to treat human cancers, we chose to compare the therapeutic effects of two commercially available anti-CD20 antibodies, rituximab and obinutuzumab. These antibodies, although they target the same protein, are structurally and functionally distinct. However, they have been directly compared clinically, allowing us a point of reference for paralleling therapeutic and survival outcomes in our RHuFR mice to those in the clinic. Rituximab is a chimeric hIgG1 with a heavy chain constant region, while obinutuzumab is a humanized IgG1 that has reduced fucosylated glycan chains in its Fc region resulting in enhanced binding to activating hFcγRIIIA. A recent Phase III study compared the clinical efficacy of obinutuzumab to rituximab in combination with chlorambucil in patients with CLL (72). This study demonstrated a significant advantage of the Fc enhanced obinutuzumab combination as compared to the rituximab combination, including a greater percentage of patients with negative minimal residual disease in both the bone marrow and blood, 19.5% to 2.6% and 37.7% to 3.3% respectively, as well as significantly enhanced median progression free survival, 26.7 months with obinutuzumab to 15.2 months with rituximab (72). Therefore, in our RHuFR mice, we expect obinutuzumab to confer a greater therapeutic response and larger survival advantage when compared to rituximab.

Simultaneously, we wanted to compare the efficacy of rituximab and obinutuzumab therapy in a commercially available Rag2-/- mouse FcγR expressing model. In order to qualitatively compare the relative effects of antibody therapy in the RHuFR and commercial Rag2-/- model, the antibodies pharmacokinetic profiles in the two models must be similar enough to establish a single antibody-dosing regimen. While there was little difference between the two antibodies in blood clearance rates within mice of the same genotype, allowing for obinutuzumab and rituximab to be dosed similarly, there were large differences between the two mouse models (Figure 15). Rag2-/- mouse FcγR+ mice had prolonged antibody blood half-lives (β half-lives >1 week), while the RHuFR mice had extremely short antibody kinetics (β half-lives <1 day). Therefore, to make dosing schedules for the two mouse strains similar, we employed the RHuFR derivative "knockout" strain that lacks human FcγRI (RHuFR^{1-}) to remedy this kinetic discrepancy. Human FcγRI is the only high affinity human FcγR that binds soluble, monomeric IgG, and thus, hFcγRI has been shown to minimally contribute to mAb therapies *in vivo* (43,74). As previously mentioned, since the RHuFR mice are Rag2 deficient and therefore lack circulating IgG, every hFcγRI receptor is unoccupied and can act as an antibody sink, potentially contributing to the shortened blood half-lives of these antibodies in the RHuFR mouse. Furthermore, the availability of hFcγRI in an antibody therapy model is unrealistic since patients typically have circulating Ig and therefore, unavailable hFcγRI. In the Rag2-/- mouse FcγR+ mice, this does not appear to be an issue despite the presence of mouse FcγRI.

Therefore, we tested the kinetics of rituximab and obinutuzumab in the RHuFR^{1-} mice (Figure 15). The observed β half-lives for rituximab and obinutuzumab were 2.9 and 3.5 days, respectively. Despite still having a shorter kinetic profile than what is observed for the Rag2-/- mouse FcγR+ mice, the ~3 day half-lives of these antibodies in the RHuFR^{1-} mouse allows for a twice weekly antibody-dosing regimen to compare therapeutic effects between the RHuFR^{1-} and the Rag2-/- mouse FcγR+ mice. In addition,

FIGURE 15

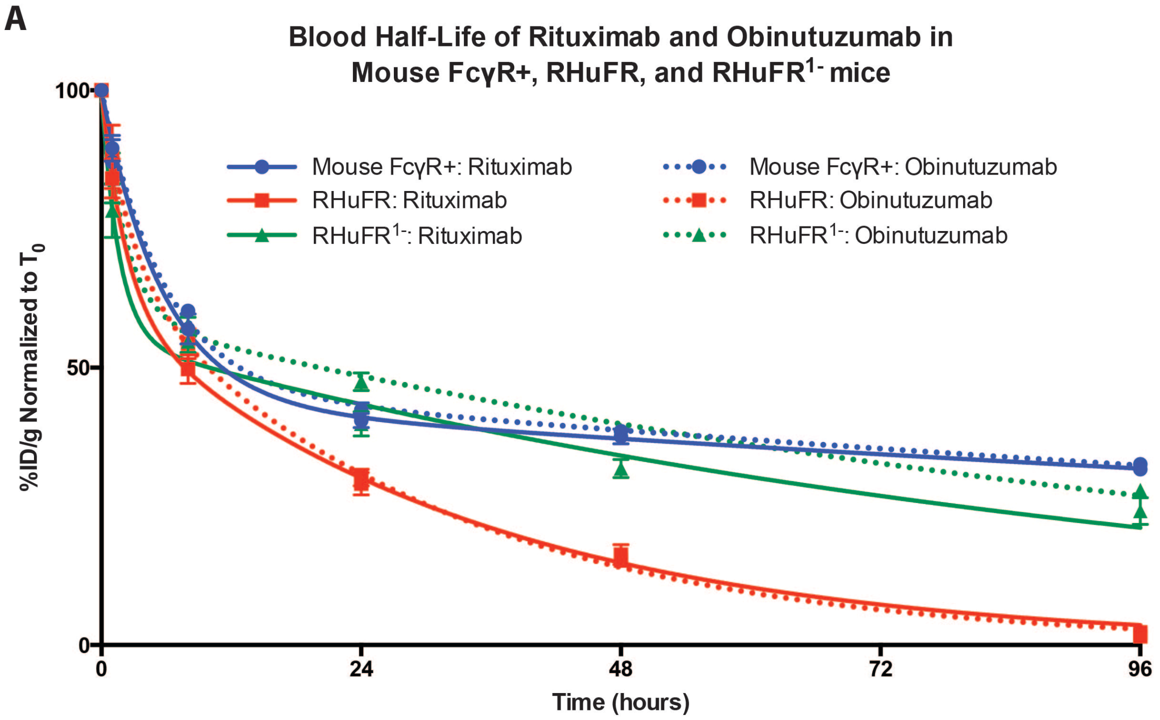

B

	Rituximab	Obinutuzumab
Rag2-/- Mouse FcγR	8.89 days	7.76 days
RHuFR	0.98 days	0.88 days
RHuFR^{1-}	2.89 days	3.54 days

Figure 15: Rituximab and obinutuzumab blood half-lives in Rag2-/- mouse FcγR+, RHuFR, and RHuFR^{1-} mice. A) I-125 labeled rituximab and obinutuzumab blood clearance measured as percent injected dose per gram (%ID/g) normalized to time 0hr (T_0) after injection into Rag2-/- mouse FcγR+, RHuFR, or RHuFR^{1-} mice (n=5 mice/genotype/antibody). **B)** Table of calculated β half-lives of rituximab and obinutuzumab in each mouse strain based on a two-phase decay model.

the half-lives of rituximab and obinutuzumab are very similar in both the RHuFR^{1-} and the Rag2-/- mouse FcγR+ mice, suggesting that they have similar affinities for the mouse neonatal Fc receptor (FcRn) that is largely responsible for antibody clearance from the circulation. Indeed, this will allow us to rule out kinetic reasons for any differences we observe between these antibody therapies within the mouse models. Importantly, the RHuFR^{1-} mouse expresses all other human FcγRs in the same manner as in the RHuFR mice (Figure 5) and is functionally intact, showing identical platelet clearance to the RHuFR mouse in the ITP model (Figure 13).

Therefore, Rag2-/- mice expressing either the mouse FcγRs or human FcγRs (RHuFR^{1-}) were engrafted with the CD20+ Daudi human lymphoma cell line, which expresses firefly luciferase allowing for bioluminescence imaging. The protocol for the engraftment of human cancer cells in the Rag2-/- mouse FcγRI and RHuFR^{1-} mice was developed after observations that simple intravenous injection of human lymphoma cell lines was insufficient for tumor outgrowth without prior manipulation. Therefore, mice undergo sublethal irradiation (500cGy) 3 weeks prior and NK cell depletion the day prior to human tumor cell injection. In order to understand why this protocol allows for successful engraftment and to ensure the recovery of the immune effector cell compartments expressing human FcγRs prior to therapeutic antibody administration, these cell population numbers were analyzed as percentages of total splenic mouse leukocytes for Rag2-/- mice undergoing this engraftment protocol (Figure 16). Strikingly, upon sublethal irradiation of these mice, the total percentage of CD45+ leukocytes within the spleen drops significantly, by approximately 50% on the day prior to tumor cell

FIGURE 16

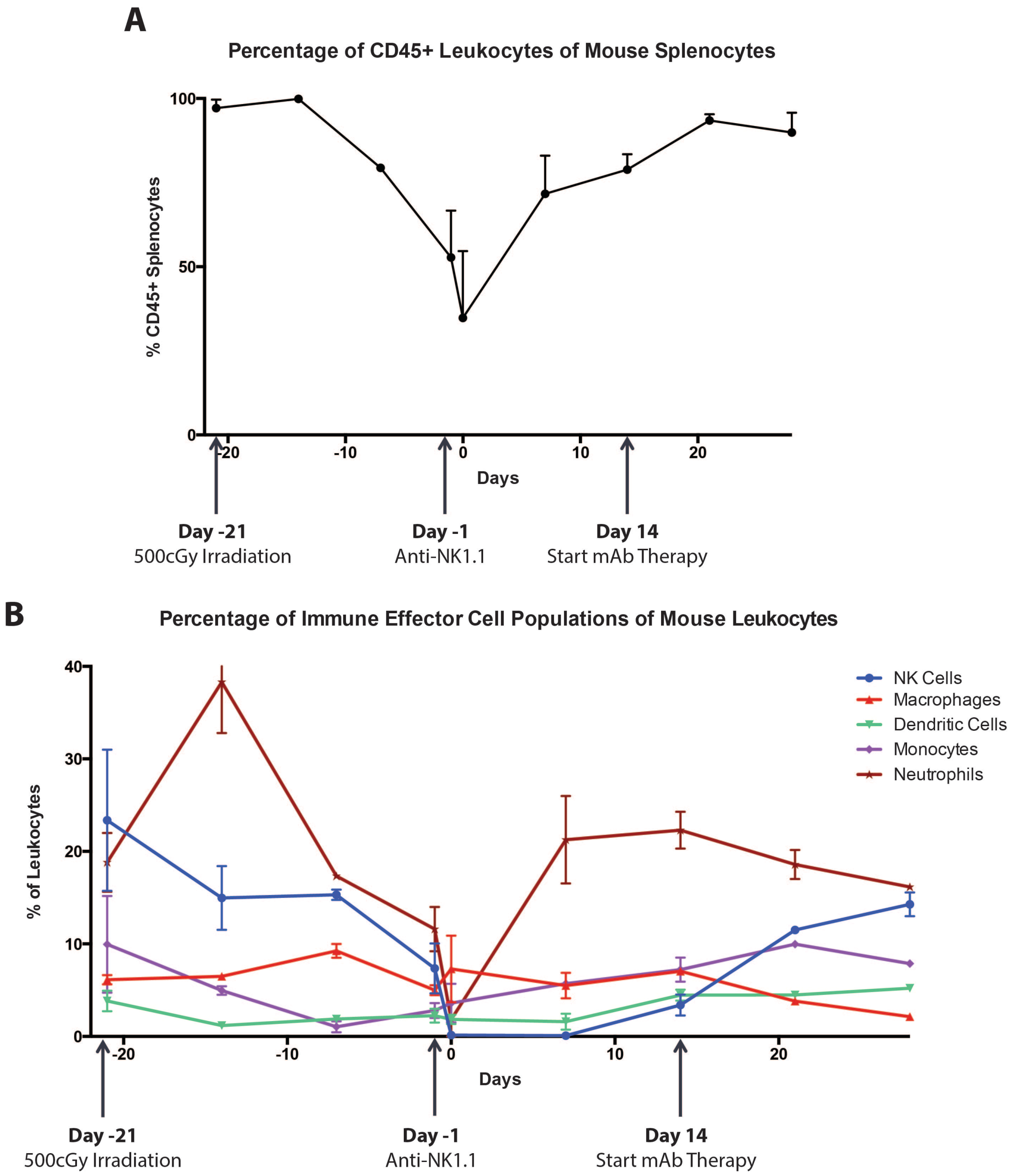

Figure 16: Mouse leukocyte population in Rag2-/- mouse spleens during engraftment protocol for human cancer cell xenografting. A) CD45+ splenic leukocytes as a percentage total splenocytes within Rag2-/- mouse spleens before irradiation (Day -21) up until Day 28 p.i. **B)** NK cell, macrophage, dendritic cell, monocyte, and neutrophil splenic populations as a percentage of CD45+ leukocytes in Rag2-/- mouse spleens before irradiation (Day -21) up until Day 28 p.i.

injection. Therefore, even though the percentages of the immune effector populations within the splenic leukocyte population do not appear to change significantly after irradiation, the total numbers of these cells are decreasing in the periphery of these mice. Furthermore, the administration of the anti-NK1.1 antibody results in the rapid depletion of both NK cells and neutrophils. Together, these effects allow for the successful engraftment of the human lymphoma cells. In addition, based on the rapid recovery of splenic CD45+ leukocytes and the neutrophil population in one week post tumor cell injection and the return of NK cells by Day 14, therapeutic antibody administration can begin as early as Day 14 post human cancer cell injection.

The affinities of rituximab and obinutuzumab for the relevant mouse and human FcγRs were measured using surface plasmon resonance (SPR) to understand the affinity interactions of these two antibodies with the FcγRs present in the Rag2-/- mouse FcγR+ or RHuFR^{1-} mice (Tables 4 and 5). The Fc engineering of obinutuzumab results in a significant 1-log increase in affinity for hFcγRIIIA over rituximab's affinity. However, there is little to no increase in affinity of obinutuzumab for mFcγRIV compared to rituximab. Indeed, both obinutuzumab and ritxumab have approximately the same affinity for mFcγRIV as obinutuzumab has for hFcγRIIIA. This could potentially suggest that both rituximab and obinutuzumab will have equivalent therapeutic benefit in the mouse FcγR expressing mouse, and, because mFcγRIV is a strong mediator of ADCC in mice, the therapy may be equivalent to the observed therapeutic benefit of obinutuzumab in the human FcγR system. The measured affinities for the other mouse and human FcγRs are very similar between the two antibodies. Of note, both obinutuzumab and

TABLE 4

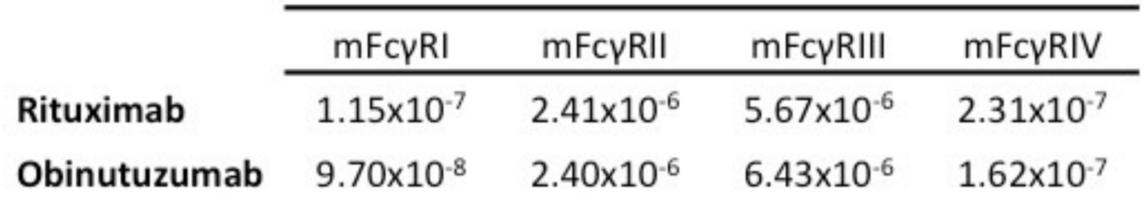

	mFcγRI	mFcγRII	mFcγRIII	mFcγRIV
Rituximab	$1.15\text{x}10^{-7}$	$2.41\text{x}10^{-6}$	$5.67\text{x}10^{-6}$	$2.31\text{x}10^{-7}$
Obinutuzumab	$9.70\text{x}10^{-8}$	$2.40\text{x}10^{-6}$	$6.43\text{x}10^{-6}$	$1.62\text{x}10^{-7}$

Table 4: Rituximab and obinutuzumab affinity measurements for mouse FcγRs. Affinity (K_D) measurements for rituximab and obinutuzumab to mouse FcγRs (I, II, III, & IV) determined by SPR analysis. All affinities are measured in molar concentration (M) units.

TABLE 5

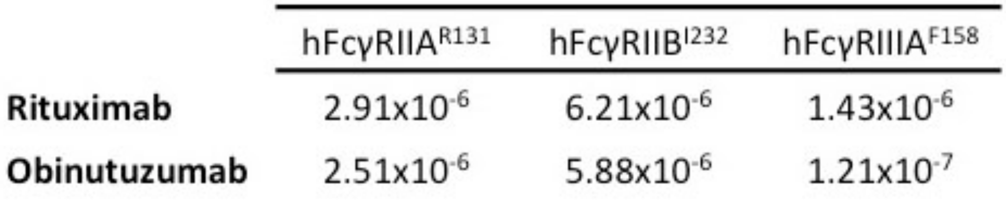

	hFcγRIIA^{R131}	hFcγRIIB^{I232}	hFcγRIIIA^{F158}
Rituximab	$2.91\text{x}10^{-6}$	$6.21\text{x}10^{-6}$	$1.43\text{x}10^{-6}$
Obinutuzumab	$2.51\text{x}10^{-6}$	$5.88\text{x}10^{-6}$	$1.21\text{x}10^{-7}$

Table 5: Rituximab and obinutuzumab affinity measurements for relevant human FcγRs. Affinity (K_D) measurements for rituximab and obinutuzumab to human FcγRs (IIA^{R131}, IIB^{I232}, IIIA^{F158}) determined by SPR analysis. All affinities are measured in molar concentration (M) units.

rituximab have a slightly higher affinity for the inhibitory mouse FcγRII than they do for the inhibitory human FcγRIIb, while the opposite is true for the activating mouse FcγRIII and activating human FcγRIIA.

After the engraftment of the Rag2-/- mouse FcγR+ and RHuFR^{1-} mice with the Daudi lymphoma cells, all mice were randomized into one of four groups for relatively equal initial tumor burden: untreated, isotype (hIgG1), rituximab, and obinutuzumab. Antibody administration began on Day 14 post-injection (p.i.) of the Daudi cells, if applicable, and continued twice weekly for 3 weeks. Bioluminescence imaging occurred weekly to track tumor burden in the mice, but was halted on Day 28 due to signal saturation, and survival was monitored until Day 200 p.i. In the Rag2-/- mouse FcγR+ mice (Figure 17), no significant therapeutic response benefit for rituximab was observed, as seen by little to no change in bioluminescence imaging and quantification of signal. Obinutuzumab slightly reduced tumor burden in these mice by less than 1-log compared to untreated mice. However, obinutuzumab therapy did not confer a survival advantage over rituximab therapy in the Rag2-/- mouse FcγR+ mice. Indeed, both rituximab and obinutuzumab treatment only slightly enhanced survival in these mice over untreated and isotype groups.

In contrast, the RHuFR^{1-} mice recapitulated the clinical superiority of obinutuzumab over rituximab therapy. Rituximab modestly slowed lymphoma growth in the RHuFR^{1-} mice, while obinutuzumab achieved significant eradication of the lymphoma with a ~1- vs. ~2-log reduction in tumor burden from untreated, respectively (Figure 18). Moreover, by Day 28, 9/10 mice on obinutuzumab therapy had no detectable tumor burden, while only 4/10 mice on rituximab therapy showed no detectable tumor.

FIGURE 17

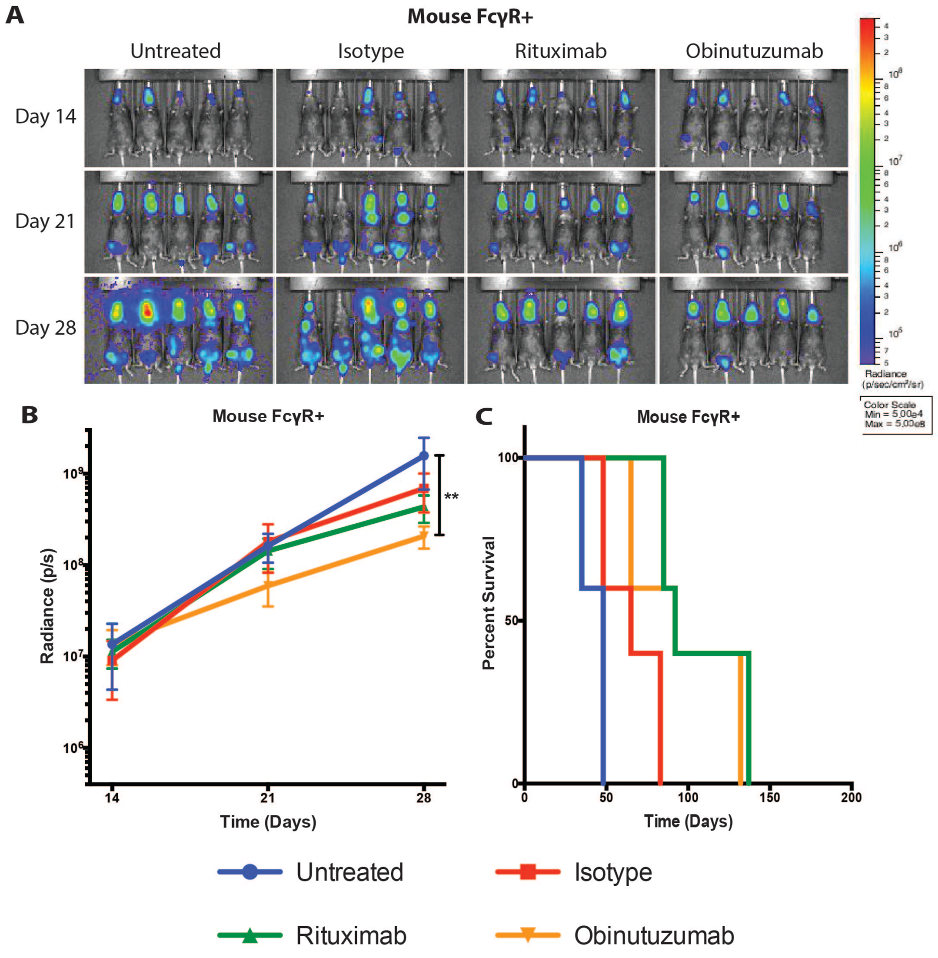

Figure 17: Obinutuzumab versus rituximab therapy of human lymphoma in Rag2-/- mouse FcγR+ mice. A) Bioluminescence imaging of Rag2-/- mouse FcγR+ mice at that start of therapy (Day 14) up until the final imaging time point (Day 28). Imaging was halted after Day 28 due to saturation of signal. No mice died or were sacrificed prior to Day 28. **B)** Quantification of total radiance signal (photons/second) and **C)** Kaplan-Meier survival curves for Rag2-/- mouse FcγR+ mice (n=5 mice/group). No significant difference in tumor burden was observed by Day 28 for rituximab therapy as compared to untreated or isotype treated. Obinutuzumab therapy resulted in a small but significant reduction in overall tumor burden when compared to untreated mice ($p=0.0072$). Despite a slight survival benefit for the rituximab and obinutuzumab treatment groups compared to untreated and isotype ($p=0.0032$ and $p<0.0001$ for rituximab, respectively; $p=0.0026$ for obinutuzumab compared to untreated), no difference in survival was observed between these two anti-CD20 therapy groups.

FIGURE 18

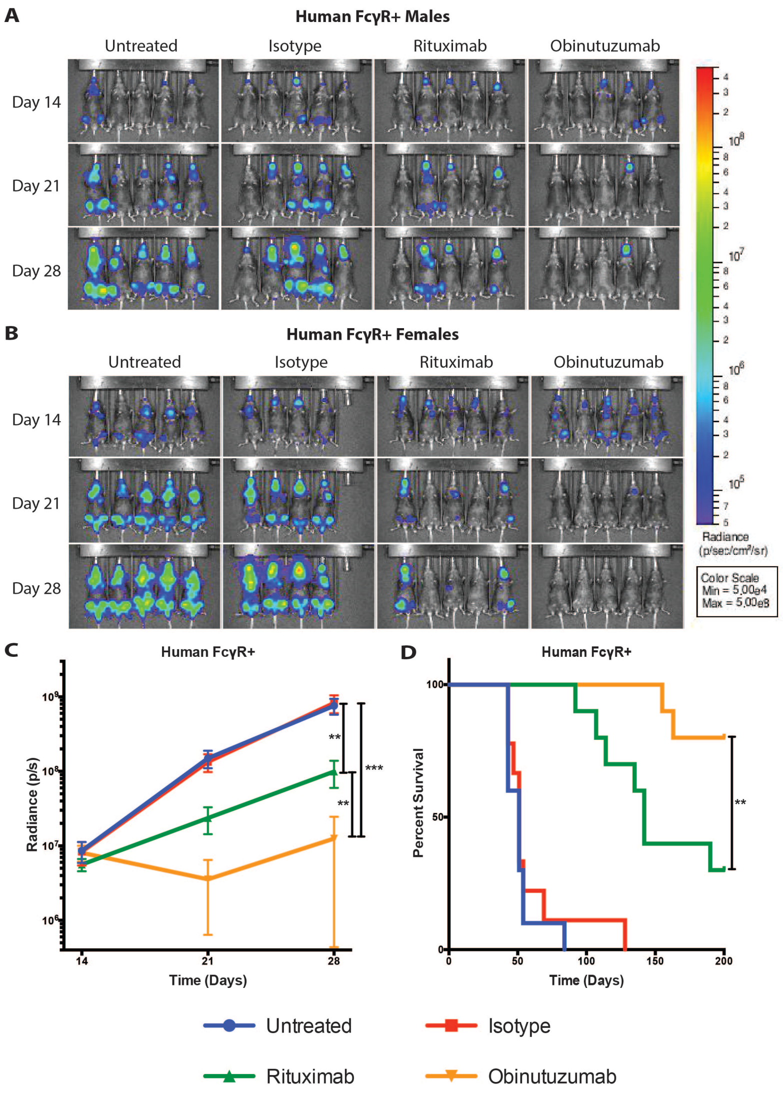

Figure 18: Obinutuzumab versus rituximab therapy of human lymphoma in RHUFR^{1-} mice. Bioluminescence imaging of Rag2-/- human FcγR+ male mice **A)** and female mice **B)** at that start of therapy (Day 14) up until the final imaging time point (Day 28). **C)** Quantification of total radiance signal (photons/second) and **D)** Kaplan-Meier survival curves for all RHuFR^{1-} mice (n= 9-10 mice/group). Rituximab therapy resulted in a modest, albeit significant, reduction in tumor burden compared to untreated and isotype groups (p=0.0042 for both). Meanwhile, on obinutuzumab therapy, the RHuFR^{1-} mice demonstrated significant reductions in tumor burden compared to untreated and isotype (p<0.0001 for both). There was also a significant difference in overall tumor burden between rituximab and obinutuzumab treated groups (p=0.003). Moreover, both treatment groups showed significant survival advantages from untreated and isotype (p<0.0001 for rituximab compared to both; p<0.0001 and p=0.0002 for obinutuzumab, respectively). In addition, there is a greater survival benefit for obinutuzumab therapy compared to mice on rituximab therapy (p=0.0088).

Both rituximab and obinutuzumab treatment resulted in increased median survival compared to untreated and isotype treated mice. Furthermore, a significant survival advantage for obinutuzumab vs. rituximab treated RHuFR^{1-} mice was seen. This data is consistent between the both the male and female mice tested in this model, despite the escape of tumor in a single male mouse, and it directly mimic the enhanced therapeutic response rates and prolonged progression free survival trends for obinutuzumab therapy over rituximab therapy observed in the clinic (72). Furthermore, these data support the importance of testing Fc enhanced therapeutic antibodies in the setting of the human FcγR network.

Discussion

The RHuFR mice provide an improved and more accurate predictive tool for the study of therapeutic anti-cancer antibodies in a xenograft model that faithfully mimics human FcγR signaling and response. In contrast to the traditional immunodeficient model with mouse FcγRs, the RHuFR^{1-} mice reproduced the clinical observations for rituximab vs. obinutuzumab therapy. This is a proof-of-concept of how this mouse can be used to better predict clinical outcomes of anti-cancer antibody therapies.

Further work to validate the usefulness of the RHuFR mice for predictive ability is necessary. We have successfully shown that the RHuFR mouse can distinguish therapeutic benefit of an Fc enhanced human IgG1 compared to a WT hIgG1. While other Fc enhanced antibodies are currently being developed, no other direct clinical comparison between an Fc enhanced antibody and an equivalent WT hIgG1 antibody targeting the same antigen exists. Therefore, we have no other benchmark for predictive ability of our RHuFR mice other than clinically successful antibodies, such as rituximab, trastuzumab, and cetuximab, and clinically unsuccessful antibodies, such as lintuzumab, farletuzumab, brentuximab, iratumumab, and adecatumumab. However, obtaining these failed antibodies is difficult since many of them are no longer being manufactured as whole unmodified antibodies or at all.

Nonetheless, using our RHuFR mouse to test clinically successful therapeutic antibodies, and when available Fc enhanced versions of those antibodies will serve to better prove the utility of this model. Currently, a mammary fat pad model of Her2+ human breast cancer is being developed in the RHuFR^{1-} mice, as well as the Rag2-/-

mouse FcγR+ mice, to validate growth of a solid tumor and therapeutic efficacy of another commercially available therapeutic antibody, trastuzumab, in the RHuFR^{1-} mice.

In addition to more therapeutic antibody studies, repeating the rituximab versus obinutuzumab study in the RHuFR mice with an adjusted dosing schedule for antibody blood clearance would be insightful to whether or not the expression of hFcγRI can interfere with therapeutic antibody efficacy. Furthermore, repeating this lymphoma therapy study in RHuFR$^{1/3A-}$ mice will help our understanding of the role of obinutuzumab's increased affinity for hFcγRIIIA in the enhanced therapeutic response and survival benefit over rituximab therapy. This will be the most compelling evidence for the role hFcγR affinity plays in *in vivo* activity.

Both rituximab and obinutuzumab have been shown to have Fc-independent direct cytotoxic activity via two distinct mechanisms. As a type II anti-CD20 antibody, obinutuzumab is more effective at induced direct cytotoxicity to CD20+ cells than rituximab, a type I anti-CD20 antibody (71). Therefore, it is possible that some of the improved therapeutic response observed in the RHuFR^{1-} obinutuzumab treated mice came from increased direct cytotoxicity rather than enhanced ADCC. This contribution would be minimal since the Rag2-/- mouse FcγR+ mice showed little enhanced therapy for the obinutuzumab treated group compared to rituximab. However, in order to rule this possibility out, we can use PNGase F to treat the rituximab and obinutuzumab antibodies prior to administration to the RHuFR^{1-} mice. PNGase F cleaves off the glycan chains from an antibody's Fc region, thus rendering it unable to engage FcγRs, but still enact Fc-independent direct cytotoxic action. By treating RHuFR^{1-} mice with PNGase F treated rituximab and obinutuzumab, the contribution of direct cytotoxicity for each therapeutic antibody can be measured.

Meanwhile, the RHuFR derivative strains lacking one or more hFcγRs will allow for the probing of the individual roles of each receptor in both pharmacology and therapy. This is especially important when looking to enhance a wild type hIgG1's therapeutic effects. Testing the efficacy of a therapeutic antibody in one of these RHuFR "knockout" mice can help to quickly identify the receptors responsible for mAb therapy *in vivo* and subsequently direct Fc engineering of the antibody to enhance affinity for those receptors most important for therapeutic effect. Furthermore, crossing these RHuFR "knockout" strains can quickly create mice containing other combinations of human FcγR "knockouts" for probing receptor interactions and redundancy in function.

In particular, recent studies have revealed that the hFcγRIIA receptor polymorphism H131R similarly predicts human clinical response to therapeutic antibodies in the same manner as the hFcγRIIIA V158F polymorphism. Specifically, multiple reports for patients receiving rituximab, trastuzumab, or cetuximab treatment demonstrated that patients with the hFcγRIIA H/H genotype experience a higher objective therapeutic response and improved progression free survival than those patients with either the H/R or R/R genotypes (56-60). These results mirror what is reported for the hFcγRIIIA V/V genotype, suggesting that both hFcγRIIA and IIIA play important roles in therapeutic antibody success in patients. With this knowledge, Fc engineering efforts should move from focusing on enhancement of hFcγRIIIA affinity to both hFcγRIIA and IIIA affinity. Our RHuFR mice supply tools to tests the effects of Fc engineering in the presence or absence of both, or one or the other IIA and IIIA receptors.

This will allow researchers to validate the enhanced receptor affinities consequence on therapeutic efficacy *in vivo*.

In addition, this shift from focusing on hFcγRIIIA as the key to therapeutic antibody success to hFcγRIIA mirrors the shift in focusing on NK cells as the main mediator of ADCC to other effector leukocytes, specifically macrophages. Recently, efforts to enhance therapeutic activity of macrophages during cancer therapy via blockage of the CD47 "do not eat me" ligand on cancer cells have been highly successful (91-94). More interestingly is that anti-CD47 therapy can synergize with therapeutic anti-cancer antibodies, such as rituximab (95), suggesting that macrophages are playing an prominent role in antibody *in vivo* therapeutic activity. Other evidence of this has been observed in the immunocompetent humanized FcγR mice, where depletion of macrophages from the mice results in loss of antibody-induced cell depletion, like the model of ITP described here, which is not observed upon NK cell depletion (96). Therefore, our RHuFR mice supply unique tools to study the effects of human FcγR expression on specific effector leukocytes on therapeutic antibody activity for human cancer treatment.

The potential importance of other immune effector cells, such as monocytes and macrophages, in therapeutic antibody efficacy brings up the issue of the high amount of diversity and genetic complexity of the different monocyte and macrophage populations. For example, tissue resident macrophages are highly specialized and functionally distinct in many ways from one another, such as splenic macrophages, liver Kupffer cells, bone osteoclasts, and brain microglia. The genetic programming of these cells required for their specialization can greatly influence their functional output for FcγR-induced cytotoxicity (97). Thus, the expression of the human FcγRs under their endogenous regulatory elements in these vastly differentiated effector cells can give us a substantial advantage in parsing out the extent to which these various specialized effectors can engage in ADCC.

With Fc engineering efforts and the importance of understanding mechanisms of action for FDA approval and patient selection, the RHuFR and RHuFR single and combined "knockout" mice provide essential tools for therapeutic antibody testing. As seen in the model of antibody-induced ITP, use of both the single and combination RHuFR "knockout" mice indicated hFcγRIIA as a main mediator of this observed platelet depletion, possibly through the formation of immune complexes via platelet to platelet hIgG1-hFcγRIIA binding and clustering and subsequent phagocytic clearance. Despite further investigation need to confirm or refute this hypothesis, the studies in the RHuFR single and combination "knockout" mice gave a clear indication of which receptors are involved in the mechanisms of action of the 6A6 antibody in the context of the human FcγR network. Using this as a proof-of-concept, these mice can be used to model other therapeutic antibodies in order to parse out their FcγR mediated mechanisms of action.

Overall, these new RHuFR mice are essential tools to predict the therapeutic activity of an anti-cancer antibody in the clinic and to understanding the mechanisms by which an antibody functions in FcγR mediated cancer cell cytotoxicity. The data presented in this chapter supports the adoption of the RHuFR mice as the new standard for preclinical screening of therapeutic human anti-cancer antibodies.

CHAPTER II

Introduction

Antibody therapies have an additional limitation for the application as a cancer treatment in that they are limited to targeting proteins expressed on the surface of cancer cells. The number of cancer-specific cell surface proteins is limited, and selectively choosing targets that are specific enough to cancer cells to avoid off target toxicity is becoming increasingly challenging. Many cancer specific proteins are intracellular and therefore, inaccessible to targeting with a therapeutic antibody. One such intracellular cancer target is the Wilms' Tumor 1 (WT1) protein (98). WT1 is highly expressed in a large number of both solid and hematological malignancies (Figure 19) (99-115). WT1 is a critical transcription factor that is widely expressed during development (116-119), but in adults, the expression of WT1 is highly limited to a small number of specialized cells within the urogenital and hematopoietic systems (117,120-122). The expression of WT1 in cancer is highly aberrant, and the function of WT1 in oncogenesis is still unclear (123).

Interestingly, WT1 was found to be highly immunogenic (124), with the detection of WT1 specific antibodies discovered in patients with hematological malignancies (125). This let to a series of studies both *in vitro* and in the clinic demonstrating the presentation of immunogenic WT1 peptides on major histocompatibility complex (MHC) class I, which allows the immune system access to the WT1 protein (126-129). This and discoveries of the immunogenicity and presentation of other cancer specific proteins led researchers to create a new class of therapeutic antibodies, called T cell receptor-mimic

FIGURE 19

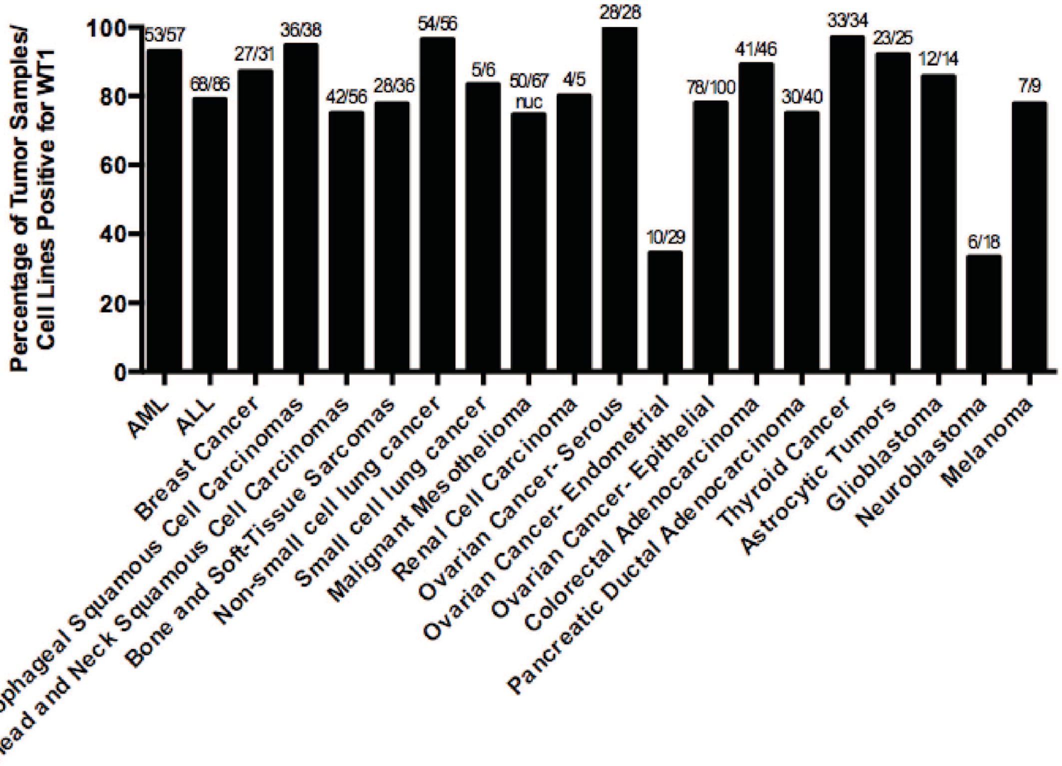

Figure 19: Frequency of overexpression of WT1 in selected hematopoietic malignancies and solid tumors. WT1 overexpression was detected by RT-PCR, IHC, or WB for mRNA or protein expression, respectively, and is defined as increased expression of WT1 mRNA or protein in tumor samples/cell lines as compared to corresponding normal tissues of the same origin*. nuc: nuclear staining, RT-PCR: real-time polymerase chain reaction, IHC: immunohistochemistry, WB: western blot.

(TCRm) antibodies (130). TCRm antibodies mimic a CD8+ TCR in that they are specific for a particular peptide in complex with a certain MHC class I haplotype presented on the cell membrane. However, while TCRs typically bind to their target peptide/MHC with a relatively low affinity, TCRm mAbs can achieve a much higher affinity for their target peptide/MHC. The development of TCRm antibodies allows the therapeutic antibody target selection to be greatly expanded to intracellular cancer-specific proteins presented on MHC class I.

Many TCRm mAbs have been developed thus far, including those targeting cancer antigens presented on MHC class I, such as PR-1 in leukemia(131), TARP in breast and prostate cancer*, human chorionic gonadotropin (hCG)-β, RNA helicase p68, and MUC-1 in breast cancer (132-134), and Melan-A/Mart-1, gp-100, and tyrosinase in melanoma (135). These TCRm mAbs have been used as a tool to study antigen presentation and other aspects of immunobiology in the context of cancer and elsewhere. Furthermore, they have already exhibited substantial therapeutic potential via innate mechanisms of cytotoxicity, including Fc-independent direct cytotoxicity, CDC, and ADCC, as well as being adapted for use as ADCs.

Our lab, in collaboration with Eureka Therapeutics, developed a novel TCRm mAb to directly target a specific WT1-derived 9-mer peptide, RMFPNAPYL (RMF), known to be presented by MHC class I and immunogenic, in complex with the common MHC class I haplotype HLA-A*02:01 (136). This anti-RMF/HLA-A*02:01 mAb, called ESK1, is a human IgG1 and rigorously screened for high specificity and affinity. Specifically, ESK1 was shown to bind selectively to a panel of WT1+ HLA-A*02:01+ cancer cell lines without binding to WT1+ HLA-A*02:01- cancers with nanomolar affinity (136). Furthermore, ESK1 did not bind to peripheral blood mononuclear cells (PBMCs), which are WT1-, derived from HLA-A*02:01+ healthy donors. In mouse models of human leukemia, ESK1 was able to greatly reduced tumor burden (136). We also created an afucosylated Fc engineered version of ESK1, called ESKM, which proved superior to ESK1 in both a mouse models of human leukemia and mesothelioma, both of which were WT1+ HLA-A*02:01+ (137).

Strikingly, when the number of ESK1 antibodies bound to target cancer cells was measured, the number of measured antibodies bound per cell ranged from approximately 750-6,500 ESK1 molecules (136). Considering the nature of a TCRm mAb target, a single peptide of the millions of potential peptides produced in a cell presented on an MHC class I molecule, this range of 750-6,500 potential epitope sites for ESK1 on a target cell is reasonable. However, the human leukemia cell line used in the therapy studies *in vivo*, BV173, was measure to bind an average 750 ESK1 molecules per cell, with as few as ~600 mAbs/cell. Despite this, the bulk of the BV173 tumor burden is cleared *in vivo* upon ESK1 treatment.

While it has been reported that T cells may recognize and kill target cells with as few as 3 epitopes (138), this number is not known for ADCC. It has been presumed to be far higher than that required by T cells since current commercially available therapeutic mAbs, such as rituximab or trastuzumab, target highly expressed proteins (10,000-500,000 potential antigens per cell surface). Compared to that, the range of ESK1 antibodies bound per cell is incredibly low. The implications of these finding can have profound effects on the progress of the therapeutic antibody field. Therefore, a full understanding of the mechanisms of action of ESK1 and ESKM is necessary.

Assays of ADCC *in vitro* demonstrate that both ESK1 and ESKM are successful at mediating FcγR recruitment of immune effectors and subsequent cytotoxicity of multiple WT1+ HLA-A*02:01+ cancer cell lines, with ESKM proving superior due to its enhanced hFcγRIIIA affinity (137). However, no CDC or Fc-independent direct cytotoxicity for either ESK1 or ESKM had been observed *in vitro* (136,137). Furthermore, the afucosylation of ESKM reduces its ability to bind the complement protein, C1q, resulting in a decreased ability to initiate CDC. This suggests that complement cannot be contributing greatly to therapeutic activity *in vivo* due to ESKM's enhanced therapeutic activity. This *in vitro* data strongly suggest that ADCC, and not CDC or Fc-independent direct cytotoxicity, is the mechanism by which ESK1 and ESKM promote therapeutic activity. However, since the environment *in vivo* can potentially influence the interactions of ESK1 and ESKM with their antigenic target, Fc-independent mechanisms of cytotoxicity cannot yet be ruled out.

Therefore, we sought to answer two questions. The first is whether or not ESK can act exclusively via ADCC *in vivo*, or if the environment *in vivo* allows for Fc-independent cytotoxicity not observed *in vitro*. The second is, using ESK1 as a tool, can we uncover the number of epitope sites required for an antibody to bind to induce ADCC via NK cell activation. In this chapter, I will show that indeed, ESK1 functions solely through Fc-dependent ADCC in order to achieve a therapeutic response *in vivo*. Furthermore, I will discuss the tools and methods I used to begin to quantify the number of antigen sites required for ADCC mediated by ESK1, the challenges faced in achieving this answer, and potential solutions for these challenges for quantifying this number in the future.

Materials and Methods

Cloning of ESK heavy chain variable regions into mouse IgG expression vectors

PCR primers contain a 5’ EcoRI restriction enzyme site and 3’ Xho1 or Not1 restriction enzyme site were used to amplify the ESK variable regions from ESK1 heavy and light chain containing plasmids (Eureka Therapeutics, Emeryville, CA), respectively. PCR was performed using *Taq* DNA Polymerase using Standard *Taq* Buffer (New England Biosciences) following manufacturer’s PCR protocol, and PCR products were purified using the QIAquick PCR Purification Kit (Qiagen) according to the manufacturer’s protocol. Restriction enzyme digest on the PCR products and expression vectors were performed using EcoR1 and Xho1 (New England Biosciences) for the heavy chain variable regions and heavy chain expression vectors (mIgG2a, mIgG1, mIgG1 D265A) and EcoR1 and Xho1 (New England Biosciences) for the light chain variable regions and mIgG2a κ light chain expression vector. The heavy and light chain expression vectors were obtained from the Jeffrey Ravetch at Rockefeller University. Restriction enzyme products were run on a 1.5% agarose gel, and the bands were excised and purified from the gel using the QIAEX II Gel Extraction Kit (Qiagen) according to the manufacturers protocol. Ligation reactions were performed using the Quick Ligation Kit (New England Biosciences) following the manufacturers protocol with optimal concentrations of insert to plasmid. XL10-Gold Ultracompetent Cells (Agilent Technologies) were then transformed with the ligation products according to the manufacturer’s protocol. Single colonies were picked and grown up in overnight cultures for verification of successful transformation using the QIAprep Spin Miniprep Kit (Qiagen) and sent for sequencing. Successfully transformed bacterial clones were grown up in large volumes and purified heavy and light chain expression vectors were prepared using the PureLink HiPure Plasmid Maxiprep Kit (Invitrogen). Re-sequencing of these preparations was performed to ensure proper insertion of the ESK or mGO53 variable regions.

Expression of ESK and mGO53 chimeric antibodies

HEK-293T cells were plated in 150mm plates until 90% confluence and then transfected with ESK-mIgG2a, ESK-mIgG1, or ESK-mD265A heavy chain expression vectors + ESK light chain expression vector or the mGO53 isotype controls. Transfections were performed using optimal concentrations of polyethylenimine (PEI) and heavy chain and light chain DNA in Opti-MEM media (Gibco) added to antibody-free cell culture media (DME HG + 1X Nutridoma-SP (Roche)). This transfection media was added to each HEK-293T plate after removal of cell culture media and washing with PBS, and incubated at 37°C for 4-5 days. The media is then collected and fresh DME HG +1X Nutridoma-SP media is re-added to each plate and incubated again at 37°C for 4-5 days. Media is collected for the second time and all collected media is spun down, filtered (0.22µm pore size), and stored at 4°C until ready for purification.

Purification of ESK and mGO53 chimeric antibodies

60% w/v ammonium sulfate precipitation was first performed by slowly adding ammonium sulfate to antibody containing media and incubated overnight at 4°C with continuous mixing. Ammonium sulfate precipitated media was then ultracentrifuged at 10,000g for 1 hour at 4°C. Ammonium sulfate pellets were gently resuspended in 1X PBS and dialyzed in 10,000 molecular weight cutoff Slide-A-Lyzer Dialysis Cassettes (Thermo Scientific) overnight at 4°C, changing dialysis PBS once after 4 hours. Dialyzed samples were spun down at 1,000g for 5min at 4°C .and the supernatant is transferred to a new tube with Protein-G Sepharose Beads (GE Healthcare). Samples were incubated with Protein-G for 4-6 hours at 4°C with constant rotation. The samples were then transferred to a chromatography column and washed with ice cold 1X PBS. Antibody elution was performed with a 0.1M glycine, pH 2.7 elution buffer directly into collection tubes containing a 1M Tris, pH 10 neutralization buffer. Eluted samples were measured for protein content using absorbance at 280nm and pooled if high protein content was measured. Pooled antibody samples were dialyzed again overnight as previously done after ammonium sulfate precipitation.

Antibody protein gels

A total of 1μg of protein from each antibody sample was used. For non-reducing gels, antibodies were denatured in Laemmli sample buffer (Bio-Rad) at 95°C for 5 minutes. For reducing gels, 1X NuPAGE Sample Reducing Agent (Novex) was added to the sample buffer prior to denaturing. Protein gel electrophoresis was performed using 4-15% Mini-PROTEAN TGX gels (Bio-Rad). The gels were stained using the GelCode Blue Stain reagent (Thermo Scientific).

Flow cytometry analysis of ESK target cell binding

Non-adherent cell lines (BV173 and HL-60) were collected, spun down, and washed. Adherent cell lines (JMN and MSTO) were removed from cell culture plates using CellStripper Solution (Corning), spun down, and washed. All cells were blocked using the Human BD Fc Block (BD Biosciences) prior to staining. Single cell suspensions were stained with predetermined optimal concentrations of each antibody, and samples were analyzed using Accuri C6 cytometer (BD Biosciences). ESK and mGO53 antibodies were labeled with APC or PE using the Lightning-Link Kits (Innova Biosciences) as per manufacturer's protocol. Cell samples were stained with antibody cocktails for 30-45min on ice and washed with FACS buffer prior to analysis.

Surface plasmon resonance for measuring antibody affinities for mouse FcγRs

All experiments were performed with a Biacore T200 SPR system (Biacore, GE Healthcare) at 25^{o}C in HBS-EP^{+} buffer (10 mM HEPES, pH 7.4; 150 mM NaCl; 3.4 mM EDTA; 0.005% (v/v) surfactant P20). For the comparison of the affinity of ESK chimeric antibodies for mouse FcγRs, recombinant mouse FcγR ectodomains (Sinobiological) was immobilized to the surface of a CM5 sensor chip (GE Healthcare) using amine coupling chemistry at a density of 500 RU. ESK chimeric antibodies (0.5-16μM; 1:2 successive dilutions) were injected sequentially over flowcells of the sensor chip at a flow rate of 20 μl/min. Association time was 60 s followed by a 300-s dissociation step. At the end of each cycle, sensor surface was regenerated with 10 mM glycine, pH 2.0. Background binding to blank immobilized flow cells was subtracted and affinity constants were calculated using BIAcore T200 evaluation software (GE Healthcare) using the 1:1 Langmuir binding model.

Iodine-125 labeling and ESK chimeric blood half-life measurements

1mCi of the Iodine-125 radionuclide (PerkinElmer) was added to 100μg of each ESK chimeric antibody in PBS. Chloramine-T (Sigma-Aldrich) was added to a final concentration of 100μg/mL and reacted for 1 minute, followed by the addition of sodium metabisulfite (Sigma-Aldrich) at a final concentration of 1mg/mL and reacted for 3 minutes. Labeled antibodies then underwent purification over 10DG desalting columns (Bio-Rad). Reaction efficiency and product recovery was measured using thin layer chromatography with 10% TCA as the solvent. TLC analysis of free versus bound I-125 for both the crude reaction and antibody products measured on a Cobra II Auto-Gamma counter (Packard) using an I-125 protocol allowed for the calculation of antibody concentration and I-125 counts per µg of antibody for each sample. NOD SCID IL2Rγ_C-/- mice (NSG; Jackson Laboratories) between 8-10 weeks of age were injected I.V. with 100µg trace labeled antibody (99µg cold + 1µg hot) in sterile PBS for all ESK chimeric antibodies (n=3 mice/antibody). Mice were bled using heparinized capillary tubes at 2 minutes post antibody injection for the total initial counts injected per mouse. Each blood collection tube was preweighed to measure the total grams of blood collected per mouse for each time point. Mice were subsequently bled at 1 hour, 8 hours, 24 hours, 48 hours, and 96 hours. All blood samples were capped, spun down, and read on the Cobra II Auto-Gamma counter. Sample decay was controlled for by counting an aliquot of each antibody injection mixture at each measured time point.

Leukemia therapy study comparing ESK mouse chimeric antibody efficacy

Female NSG mice (Jackson Laboratories) of 8-10 weeks of age were injected I.V. via tail vein with $3x10^6$ BV173 Philadelphia chromosome+ (Ph+) acute lymphoblastic leukemia cells (luciferase reporter gene+) suspended in sterile PBS. Prior to the onset of therapeutic antibody administration, mice were randomized into 1 of 7 groups (n=5 mice/group): untreated, ESK-mIgG2a, mGO53-mIgG2a, ESK-mIgG1, mGO53-mIgG1, ESK-mD265A, and mGO53-mD265A. Bioluminescence imaging (BLI) of tumor growth and therapeutic antibody administration began on Day 6. Antibodies were administered twice per week at 100µg/dose I.V. for a total of 2 weeks. For BLI, 2mg/mouse of D-Lucifern (Gold Biotechnology) was injected I.V. immediately prior to imaging on an IVIS Spectrum (PerkinElmer). Imaging was halted on Day 28 due to saturation of signal.

Peptide pulsing of the TAP-deficient T2 human lymphoblastic cell line

T2 cells were collected, counted, spun down, and resuspended in pulsing media (RPMI +5% Dialyzed FBS) with 10μg/mL β2-microglobulin (Sigma Aldrich). T2 cells were plated and the desired molar concentration of peptide (Genemed Biotechnologies) was added. For blocking experiments, 30X molar excess of the blocking peptide was also added. T2 cells were incubate overnight at 37°C. For cold pulsing experiments, T2 cells were pulsed and incubated on ice for 8 hours. The following day, T2 cells were washed twice in 1X PBS prior to further manipulation to remove excess peptide. For flow cytometry analysis, cells were blocked with Human BD Fc Block (BD Biosciences) prior to antibody staining. APC or PE labeled ESK1, labeled using the Lightning-Link Kit (Innova Biosciences), or PE-Streptavidin or APC-Streptavidin (Biolegend) were used for staining at predetermined optimal concentrations following the flow cytometry protocol. For PE molecule quantitation, the Quantibrite-PE Fluorescence Quantitation Kit (BD Biosciences) was used according to the manufacturer’s protocol.

Peripheral blood mononuclear cell (PBMC) isolation

Human blood samples were added to 50mL conical tubes with a filter and Lymphocyte Separation Media (Corning). Blood samples were then centrifuged at 2,000rpm at RT for 20min without brakes. Plasma was carefully removed, and the PBMC monolayer was gently pipetted off into new tubes and washed three times with RPMI. The final PBMC preparation was counted in a 1:1 dilution of 3N acetic acid.

ADCC *in vitro* assay using Chromium-51 release

Pulsed T2 cells were collected, counted, and washed of excess peptide. Cells were labeled with Chromium-51 (Cr-51) at 50μCi Cr-51 per 1x10^6 cells for 1 hour at 37°C. Cr-51 labeled target cells were then washed twice and resuspended at desired final cellular concentration in RPMI + 5% dialyzed FBS media. Isolated PBMCs were counted and diluted to final cellular concentration for a predetermined effector to target (E:T) ratio. Antibodies were diluted to 4X desired final concentration and plated in 96-well round-bottom cell culture plates. Target and effector cells were added to antibody wells for final desired E:T ratio and antibody concentration, with all conditions performed in triplicate. Spontaneous target cell Cr-51 release and maximum target Cr-51 was calculated for by plating target cells in media only or media + 1% SDS wells, respectively. Plates were centrifuged at 800rpm for 3 min at 4°C and then incubated at 37°C for 6 hours. 30μL from each well was removed and added to corresponding wells onto LumaPlate-96 microplates (Perkin Elmer). Plates were dried overnight at RT, covered, and read the following day using the Cr-51 counting program on a TopCount scintillation counter (Perkin Elmer).

Virus production, transduction, and selection of FRET vectors in T2 cells

pMSCVpuro vectors containing the CFP-DEVD-YFP and Clover-DEVD-mRuby2 were obtained from the Morgan Huse lab. These vectors were transiently transfected into Phoenix-Ampho (ATCC) cells that stably express viral envelope proteins. Predetermined optimal amounts of Lipofectamine 2000 (Invitrogen) and vector DNA were combined in Opti-MEM media (Gibco) and added to adherent Phoenix-Ampho cells. Cells were incubated for 6 hours at 37°C before transfection media was removed and replaced with cell culture media. 24 and 48 hours post-media change, media from the Phoenix-Ampho cells was collected and filtered (0.45µm pore size) for virus collection. T2 cells were collected, counted, and spun down. 1x10^6 cells were resuspended in media, Polybrene (EMD Millipore) alone, or Polybrene + virus containing media. The optimal concentration of polybrene was previously determined. T2 cells were centrifuged with or without virus at 2,000g for 2 hours at RT, and then incubated overnight at 37°C. Spinfection was repeated the following day with virus from the second day of collection. Cells were then grown up and sorted for CFP/YFP or Clover/mRuby2 expression using an FACSAria III sorter (BD Biosciences).

3D time-lapse confocal microscopy

Pulsed T2 cells were stained with SAv-AF647 (MSKCC Molecular Cytology Core Facility) at a predetermined optimal concentration for 15min on ice and excess streptavidin was washed out after staining. Stained T2 cells were plated at a predetermined optimal cell concentration in Lab-Tek II Chamber slides (Nunc). Isolated PBMCs were added at a 1:1 E:T ratio and kept on ice prior to the start of imaging. ESK1 was added in excess concentrations immediately before the start of imaging. Confocal microscopy was performed using either the Leica TCS SP5 or SP8 inverted microscopes in a 37°C CO_2 controlled chamber for cell culture. For live cell imaging, images were acquired at multiple pre-fixed positions at 2 min intervals with maximum Z-stacks per time interval. Lasers for excitation for CFP and AF647 were used and emission signals for CFP, YFP, and AF647 was collected. Laser intensity was not adjusted once image acquisition began.

Statistical Analysis

All data are shown as means ± SEM. Statistical significance is defined as $p<0.01$. A two-way ANOVA using Bonferroni's multiple comparisons was used for the ESK chimeric antibody therapy study to determine differences in tumor burden between ESK and isotype treatment groups.

Results

ESK therapeutic activity requires FcγR engagement

Mechanistic studies *in vitro* of ESK1 and ESKM (collectively ESK) have demonstrated the essential role of ADCC in its therapeutic function, while concurrently suggesting a lack of involvement of CDC or Fc-independent direct cytotoxicity. This suggests that the main mechanism by which ESK achieves tumor cell clearance *in vivo* is through the Fcγ receptor-mediated recruitment of immune effectors cells to perform ADCC. In order to explore the role of mouse FcγRs in the therapeutic activity of ESK in current mouse models for human cancer cell xenografting, chimeric antibodies containing the antigen-binding region of ESK fused to the Fc regions of mouse IgGs were created. In particular, chimeric antibodies contain the heavy chain variable regions of ESK were cloned into a mammalian expression vector containing the constant domains of either the mouse IgG2a, IgG1, or IgG1 with a D265A point mutation.

The mouse IgG2a Fc region has high binding affinity the activating mouse FcγRIV, the mouse receptor known to be critical for ADCC activity, and therefore a high A/I ratio. Meanwhile, the mouse IgG1 Fc region does not bind to mFcγRIV and has weak binding to activating mFcγRIII and inhibitory mFcγRII, thus resulting in a low A/I ratio. Lastly, the D265A point mutation in the Fc region of mIgG1 diminishes binding to the remaining mouse FcγRs, making it unable to bind to any mouse FcγRs. By using these three ESK mouse chimeric antibodies, we will have an antibody that has a high A/I ratio, a low A/I ratio, and one that is unable to engage mouse FcγRs entirely. (75)

These heavy and light chain expression vectors for these chimeric antibodies were created and cotransfected into HEK-293T cells for expression. The mGO53 variable regions were also cloned into each of these heavy and light chain expression vectors to create isotype controls. The mGO53 antibody does not bind to any known human or mouse proteins. Upon expression, these six chimeric antibodies were purified using a protein-G column and ran on protein gels to ensure purity and correctness of size (Figure 20).

The chimeric antibodies were directly labeled with a fluorophore for analysis of retained binding to target cells. ESK-mIgG2a, ESK-mIgG1, and ESK-mD265A bound similarly to the WT1+ HLA-A*02:01+ cancer cell lines BV173 (Figure 21) and JMN (Figure 22), but did not bind nonspecifically to WT1+ HLA-A*02:01- cells. Furthermore, these ESK chimeric antibodies bound to these target cells as well as the human ESK1 antibody. The isotype control antibodies, mGO53-mIgG2a, mGO53-mIgG1, and mGO53-mD265A did not bind to any of the cancer cell lines tested.

In order to confirm the expected interactions of these ESK chimeric antibodies with the mouse FcγRs, SPR analysis was performed (Table 6). ESK-mIgG2a had very high affinity for mFcγRIV, as expected, resulting in a high-calculated A/I ratio. Meanwhile, ESK-mIgG1did not bind the mFcγRIV at all, but instead only bound activating mFcγRIII and inhibitory mFcγRII, resulting in a very low A/I ratio. Lastly, ESK-mD265A had no detectable binding for any of the four mouse FcγRs. These data recapitulate what is known about the mouse IgG subclass interactions with mouse FcγRs.

FIGURE 20

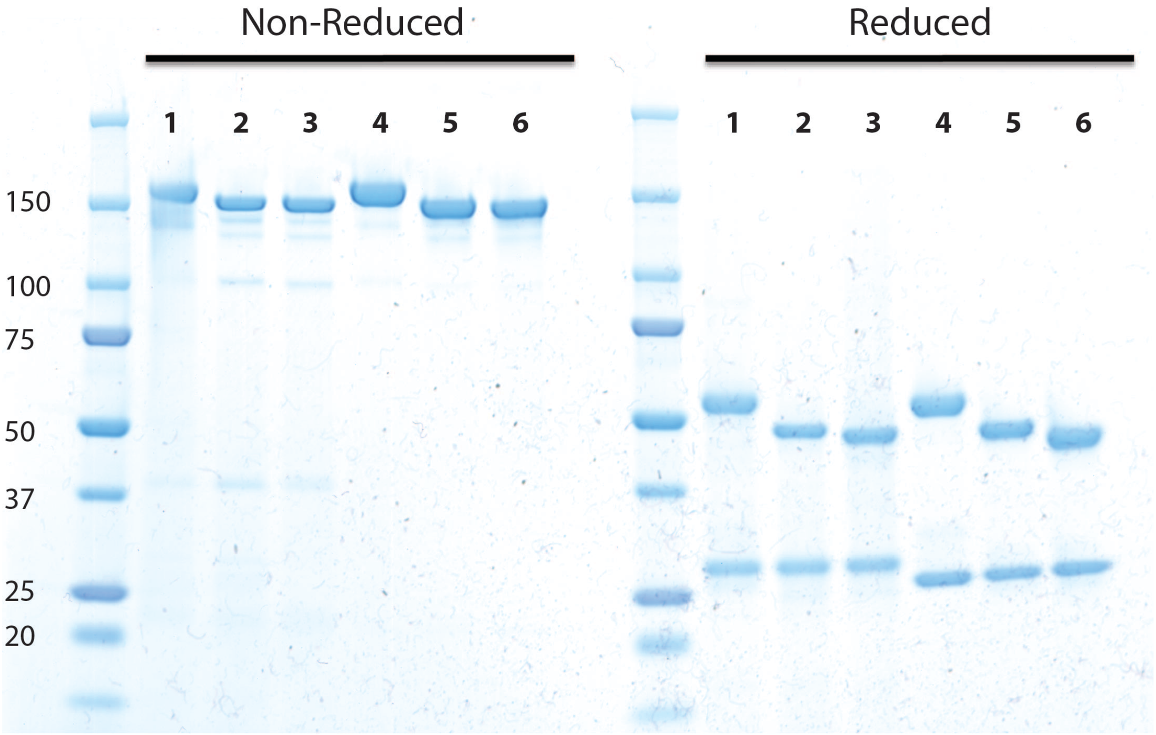

Samples:
1. ESK-mIgG2a
2. ESK-mIgG1
3. ESK-mD265A
4. mGO53-mIgG2a
5. mGO53-mIgG1
6. mGO53-mD265A

Figure 20: Production and purification of ESK and isotype mouse chimeric antibodies. Protein gel with ladder sizes (kDa) listed on the left. Samples loaded on the left half of the protein gel were prepared in non-reducing conditions, while samples on the right half of the protein gel were prepared in reducing conditions to separate heavy and light chains. All the chimeric antibodies were of the expected size (~150kDa), with those containing the mIgG2a constant region having a slightly higher molecular weight. Little to no impurities are observed in the non-reducing conditions, suggesting successful antibody assembly and purification. Reduced samples show the correct sizes for each samples heavy and light chains (~50kDa and ~25kDa, respectively).

FIGURE 21

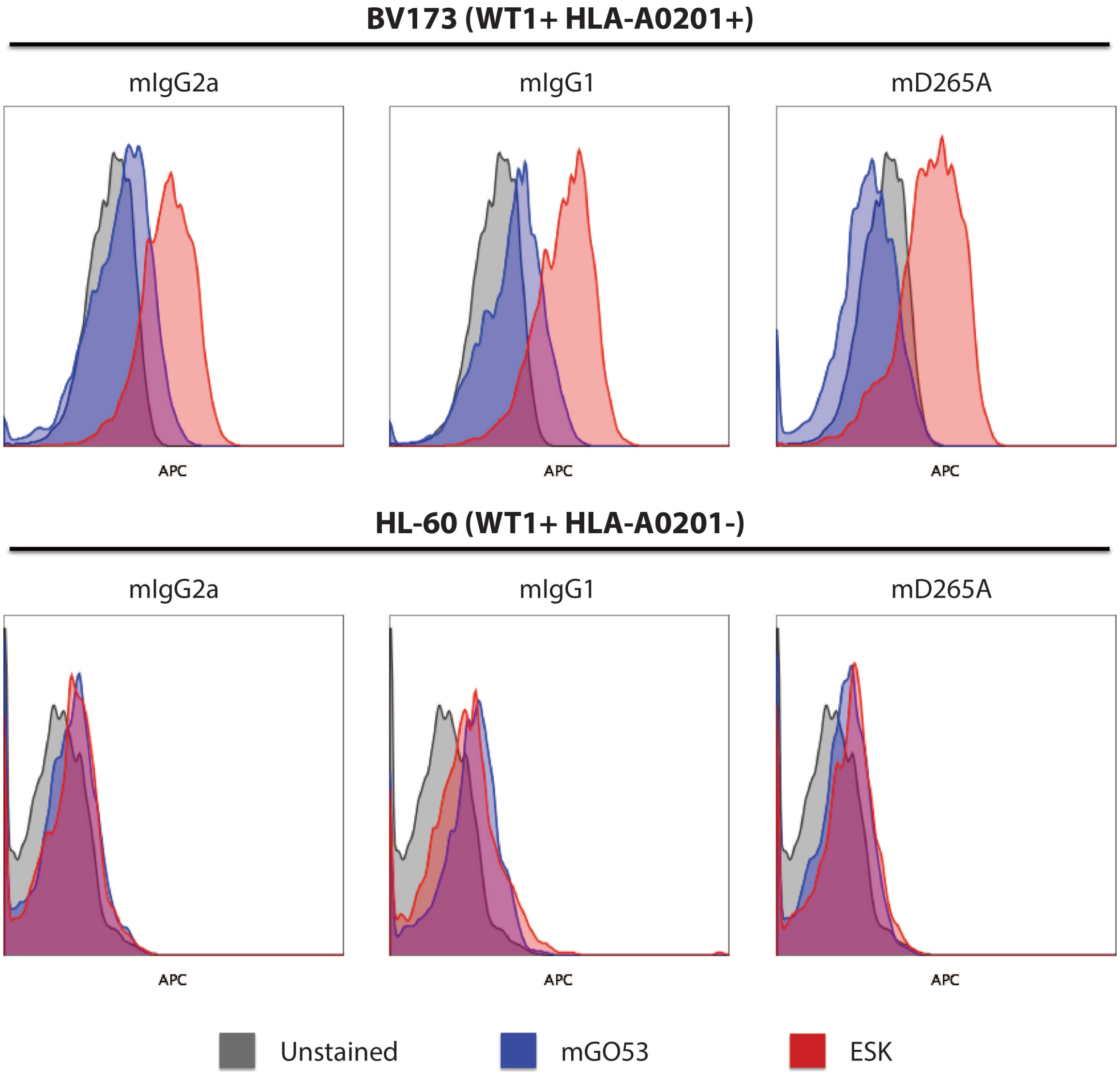

Figure 21: ESK chimeric antibodies bind WT1+ HLA-A*02:01+ human leukemia cells specifically. Flow cytometry analysis of BV173 (top panel, WT1+ HLA-A*02:01+) cells and HL-60 (bottom panel, WT1+ HLA-A*02:01-) cells for ESK mouse chimeric antibody binding. Unstained samples (grey) and isotype (blue, mGO53) and ESK (red) stained samples are shown for each mouse isotype (mIgG2a, mIgG1, or mD265A). BV173 cells bind similarly to all three ESK mouse chimeric antibodies but not the mGO53 isotype controls, while HL-60 cells do not bind to either the ESK or isotype antibodies of any subclass.

FIGURE 22

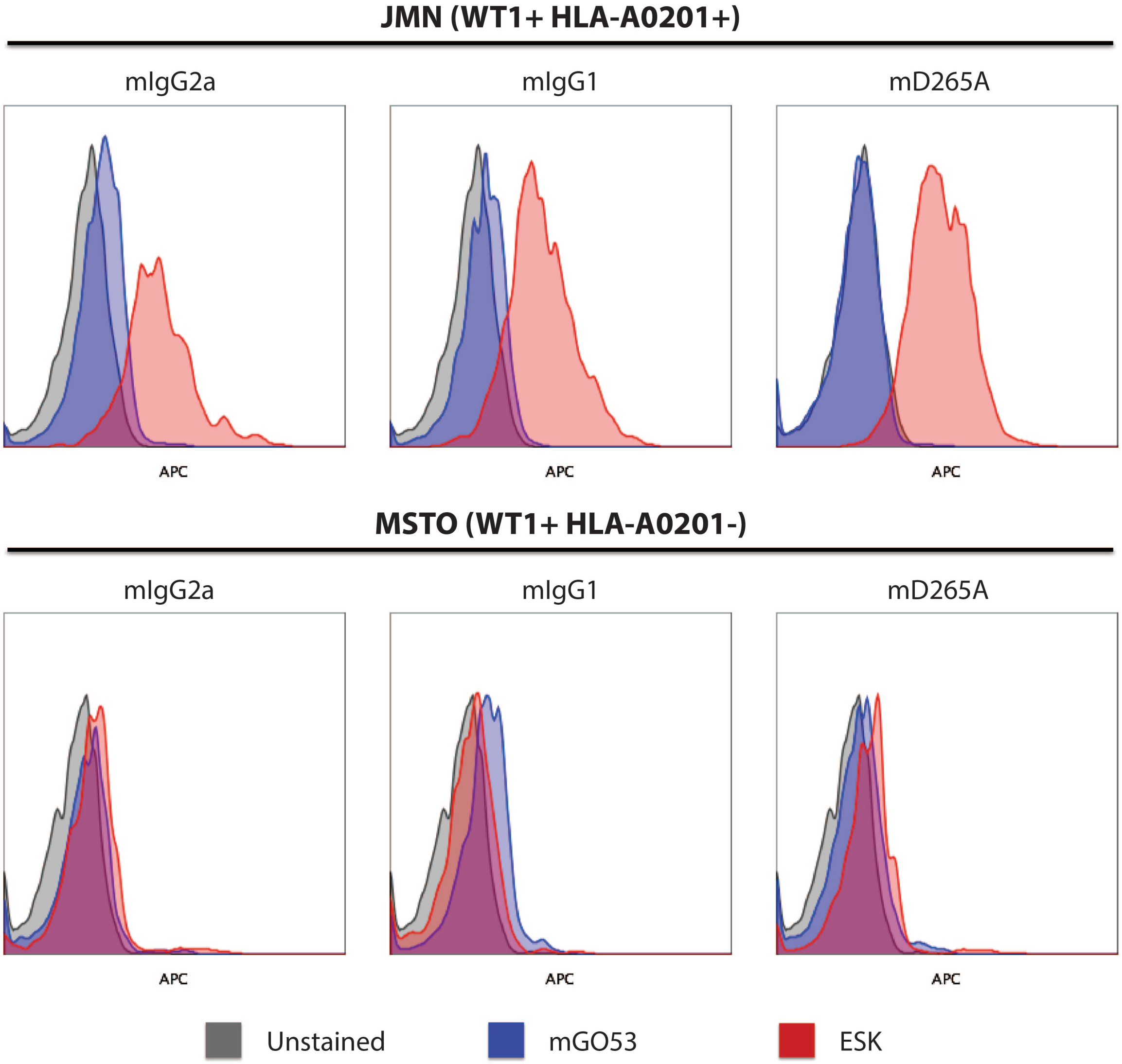

Figure 22: ESK chimeric antibodies bind WT1+ HLA-A*02:01+ human mesothelioma cells specifically. Flow cytometry analysis of JMN (top panel, WT1+ HLA-A*02:01+) cells and MSTO (bottom panel, WT1+ HLA-A*02:01-) cells for ESK mouse chimeric antibody binding. Unstained samples (grey) and isotype (blue, mGO53) and ESK (red) stained samples are shown for each mouse isotype (mIgG2a, mIgG1, or mD265A). JMN cells bind similarly to all three ESK mouse chimeric antibodies but not the mGO53 isotype controls, while MSTO cells do not bind to either the ESK or isotype antibodies of any subclass.

TABLE 6

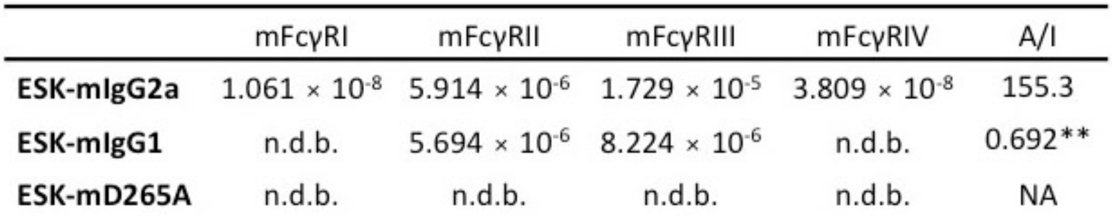

	mFcγRI	mFcγRII	mFcγRIII	mFcγRIV	A/I
ESK-mIgG2a	1.061×10^{-8}	5.914×10^{-6}	1.729×10^{-5}	3.809×10^{-8}	155.3
ESK-mIgG1	n.d.b.	5.694×10^{-6}	8.224×10^{-6}	n.d.b.	0.692**
ESK-mD265A	n.d.b.	n.d.b.	n.d.b.	n.d.b.	NA

Table 6: ESK mouse chimeric antibodies affinities' for mFcγRs. Affinity (K_D) measurements for ESK-mIgG2a, ESK-mIgG1, or ESK-mD265A to mouse FcγRs (I, II, III, & IV) determined by SPR analysis. All affinities are measured in molar concentration (M) units. A/I is calculated as ($1/K_D$ for mFcγRIV)/($1/K_D$ for mFcγRII). n.d.b. indicated no detectable binding. **A/I ratio was calculated with the K_D for mFcγRIII due to n.b.d. for mFcγRIV.

Of note, ESK-mIgG2a also had strong affinity to mouse FcγRI, while the other two chimeric antibodies did not bind to this high affinity receptor. Just as in humans, mFcγRI is the only mouse FcγR capable of binding soluble, monomeric IgG. Due to the fact that we will be performing therapy experiments in immunodeficient mice that lack circulating Ig caused by lack of mature B cells, antibody kinetics for the three ESK chimeric antibodies were measured (Figure 23). The NSG mouse model was used to measure antibody kinetics as this is the model in which we will compare therapeutic efficacy of the three ESK chimeric antibodies. This was also the mouse model used to test the therapeutic efficacy of ESK1 and ESKM. The NSG mouse is highly immunodeficient, lacking functional B, T, and NK cells. Although this is not an ideal model for measuring therapeutic antibody efficacy, it offers several advantages in that it allows us to easily engraft disseminated human leukemias without fear of rejection. Other immunodeficient models, such as SCID or Rag knockout, have functional NK cells and a stronger innate immune system. This often results in the rejection of disseminated human leukemias.

The blood half-lives of both ESK-mIgG1 and ESK-mD265A were both similar, with an extended β-half-life of greater than 1 week. However, for ESK-mIgG2a antibody, the antibody kinetics were significantly shorter, with a β-half-life of less than 24 hours. These kinetics make comparing therapeutic effect between the ESK chimeric antibodies difficult due to differences in blood clearance, and therefore, differences in dosing. We chose to keep antibody dosing regimens between the ESK chimeric antibodies the same rather than administering the antibodies with different schedules and take into consideration the different pharmacokinetics in the analysis of our therapy study.

FIGURE 23

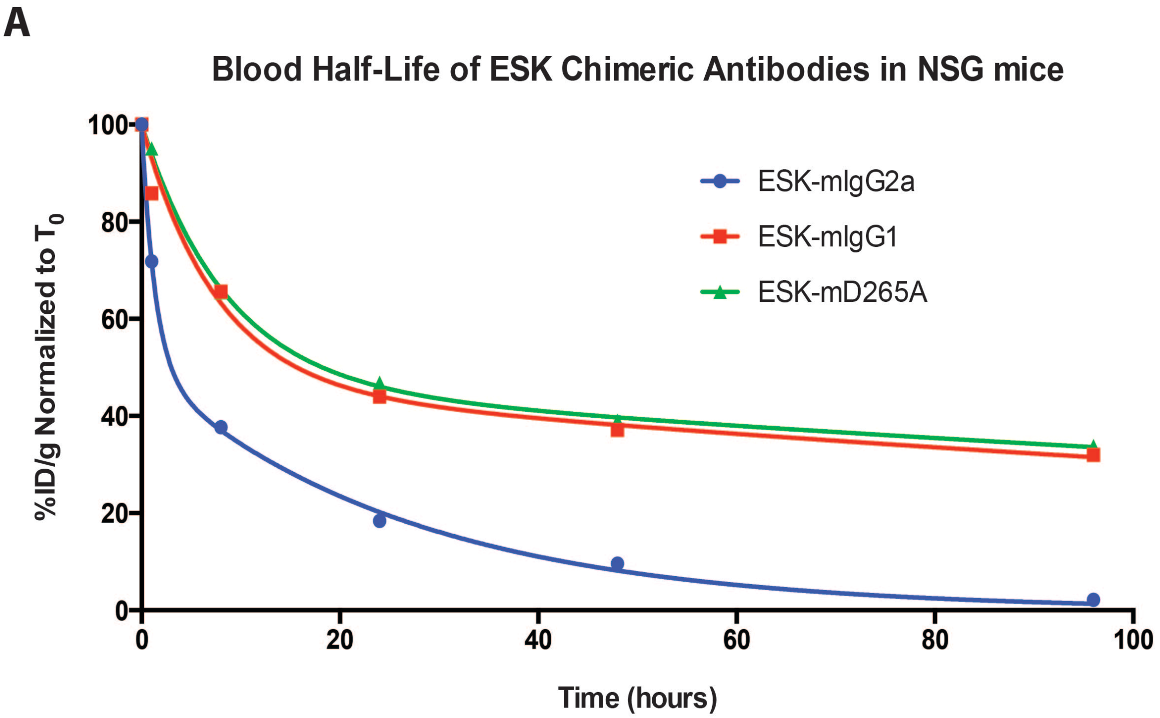

B

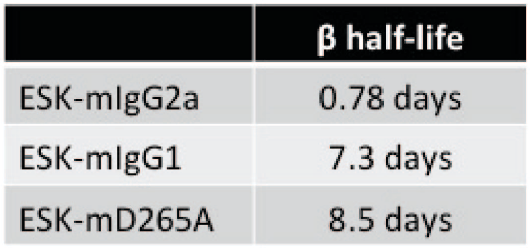

	β half-life
ESK-mIgG2a	0.78 days
ESK-mIgG1	7.3 days
ESK-mD265A	8.5 days

Figure 23: ESK mouse chimeric blood half-lives in NSG mice. A) I-125 labeled ESK-mIgG2a, ESK-mIgG1, or ESK-mD265A blood clearance measured as percent injected dose per gram (%ID/g) normalized to time 0hr (T_0) after injection into NSG mice (n=3 mice/antibody). **B)** Table of calculated β half-lives of ESK-mIgG2a, ESK-mIgG1, or ESK-mD265A in each mouse strain based on a two-phase decay model.

NSG mice were injected with the Philadelpha chromosome (Ph+) acute lymphoblastic leukemia (ALL) human cell line, BV173, that expresses firefly luciferase for bioluminescence imaging on Day 0. On day 6 p.i., mice were randomized into the seven treatment groups to ensure equal tumor burden in all groups at the onset of therapy: untreated, mGO53-mIgG2a, mGO53-mIgG1, mGO53-mD265A, ESK-mIgG2a, ESK-mIgG1, and ESK-mD265A. Antibody administration began on Day 6 p.i. and continued for 2 weeks, with antibody dosing twice weekly. As seen in Figure 24, ESK-mIgG2a had the greatest therapeutic benefit compared to the other ESK chimeric antibodies. ESK-mIgG2a greatly slowed tumor growth compared to the isotype control and untreated mice. Meanwhile, ESK-mIgG1 has a slight but insignificant slowing of tumor growth, most likely due to the residual binding to the activating mFcγRIII. Lastly, ESK-mD265a had no therapeutic effect.

Despite the fact that ESK-mIgG2a did not greatly reduce tumor burden, but rather, slowed growth, in this NSG mouse model of human ALL, it was the only ESK chimeric antibody that showed a therapeutic effect. The reason for the moderate effect of this chimeric antibody compared to the human ESK versions can potentially be due to the different expression systems used to produce these antibodies and the methods employed to purify them. Antibody therapeutic activity is highly influenced by glycosylation with its Fc region, which is variable between different cell types. The ESK chimeric antibodies were transiently transfected and produced in HEK-293T cells, while the human ESK antibodies were produced at Eureka using stable mammalian expression systems. Therefore, the different expression systems could contribute to the discrepancy in the degree of therapeutic potency of the human and chimeric mouse ESK antibodies.

FIGURE 24

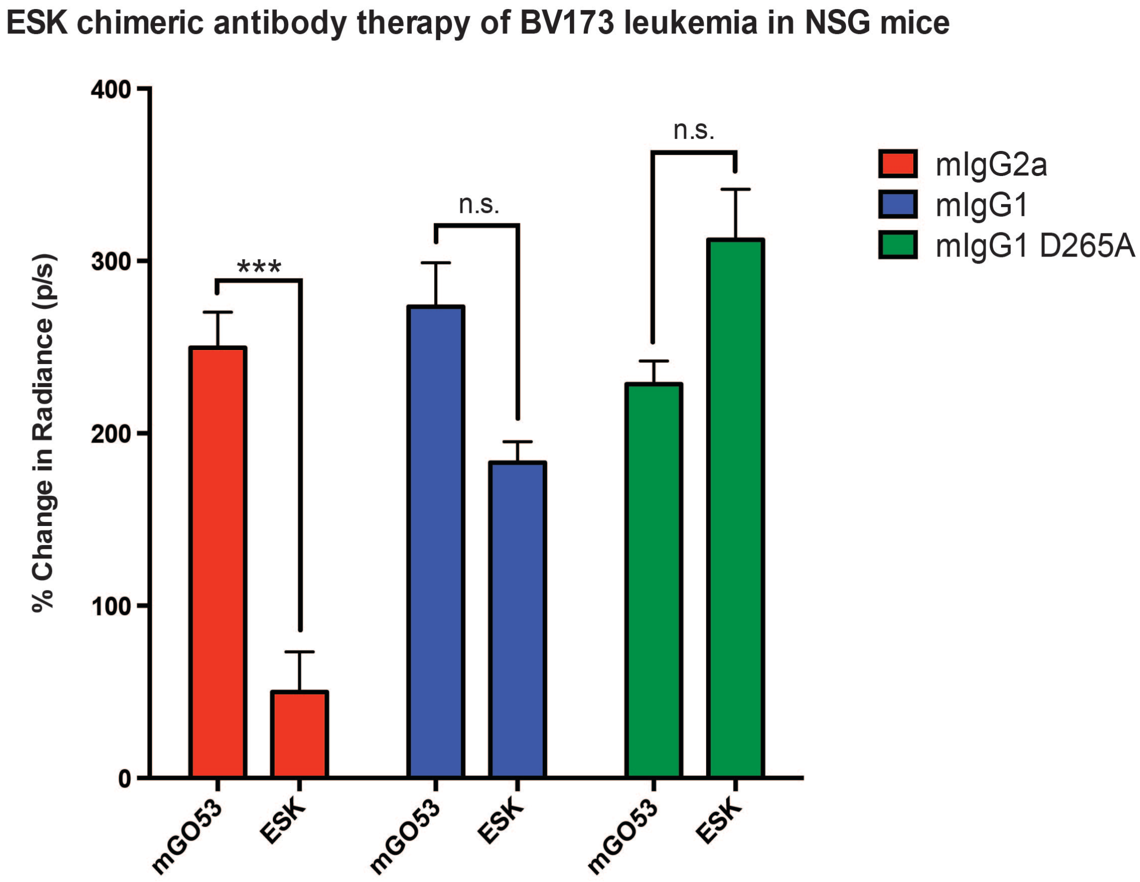

Figure 24: ESK-mIgG2a retains therapeutic efficacy in NSG mice to treat BV173 human leukemia. Bar graph of the percent change in the quantified bioluminescence imaging radiance (photons per second) on Day 12 (1 week of antibody therapy) compared to BLI radiance on Day 6 (start of therapy). Each ESK chimeric antibody was directly compared to the change in BLI signal of their corresponding isotype control (mGO53). Only the ESK-mIgG2a antibody showed a significant slowing of leukemia growth *in vivo* compared to the mGO53-mIgG2a isotype control ($p<0.0001$). ESK-mIgG1 also seemed to slow leukemia growth, but the decrease in BLI signal was not significant compared to the mGO53-mIgG1. ESK-mD265A had increased BLI signal compared to the mGO53-mD265A control, but this was not significant.

However, the fact the ESK-mIgG2a has the highest A/I ratio and is the only ESK chimeric antibody resulting in a significant therapeutic benefit suggests that ESK depends on FcγR receptor engagement for therapy. Furthermore, the lack of therapeutic effect of ESK-mD265A determines that ESK cannot mediate Fc-independent direct cytotoxicity *in vivo*. Therefore, we can determine that in the NSG mouse model, where complement is defective and cannot mediate CDC, ESK requires FcγR engagement for therapeutic activity via ADCC.

Quantification of ESK epitope site number for activation of NK cell ADCC

TCRm mAbs are extremely useful tools for the quantification of epitope site numbers required for an antibody to bind to induce FcγR-mediate NK cell activation and subsequent ADCC. The reason for this is the ability to modulate the number of TCRm epitopes present on a target cell. The way this can be achieved is via the pulsing of a TAP-deficient cell line, like the human lymphoblastic cell line T2, that expresses mostly empty MHC class I on its cell surface (139). These cells can be pulsed with peptides, which are then presented on the available MHC class I. By titrating down the concentration of peptide pulsed onto T2 cells, the average number of peptide/MHC complexes per cell is reduced. This allows for the modulation of available target antigens for a TCRm to bind, thus allowing for an accurate quantitation of antibodies bound to antigen within the immunological synapse between a target cell and an immune effector cell performing ADCC.

In order to be able to quantify the number of antibody binding events required to activate an immune effector cell for ADCC, a quantifiable probe must be developed. The strategy used here recapitulates that used for the quantification of peptide/MHC molecules required for CD4+ and CD8+ T cell activation (138,140). In this approach, the T cell specific peptide used to pulse an antigen-presenting cell (APC) was labeled at the C-terminus with a biotin group attached to the peptide by a flexible linker to prevent interference between the peptide/MHC and the TCR. The biotin can then be stained with a streptavidin labeled with a fluorophore. We adopted this strategy by attaching a flexible linker and biotin group to the C-terminus of the RMF peptide (Figure 25). The C-terminus of the peptide was chosen since it is known that the ESK antibody interacts with

FIGURE 25

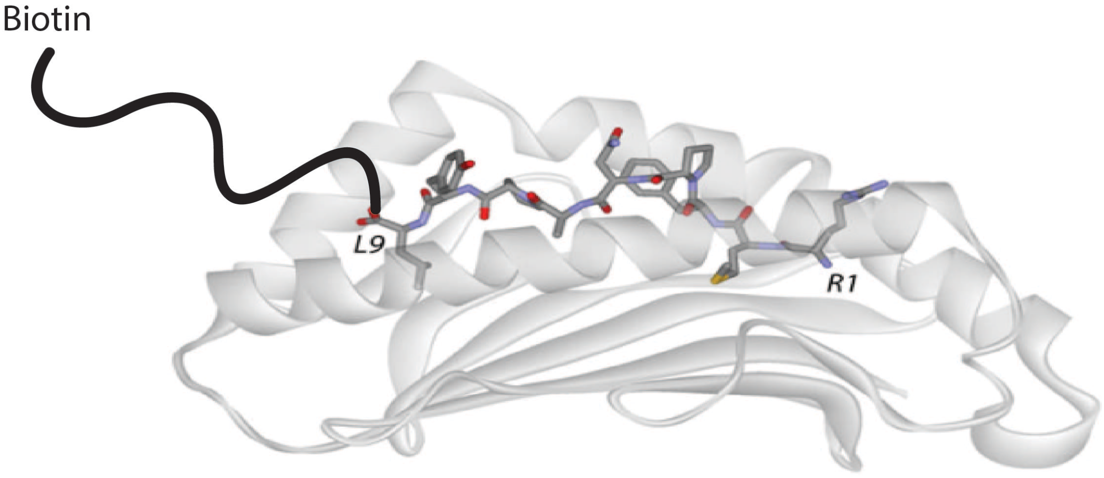

Figure 25: Model of the binding of the RMF-Biotin peptide probe to the MHC Class I HLA-A*02:01 binding groove. The peptide sequence of the RMFPNAPYL 9-mer peptide is modeled to demonstrate fit in the HLA-A*02:01 binding groove. The C-terminal leucine (L-9) is depicted with the flexible linker (-GGG(d-S)GGG(d-S)GGG(d-S)GGG(d-S)K-) attached to the carboxyl group (138,140). The biotin moiety is attached to the lysine (K) at the end of the flexible linker. (d-S) indicated the "D" enantiomer of the serine amino acid. Figure modified from (141).

the RMF/HLA-A*02:01 antigen at the N-terminus of the peptide via alanine scanning experiments (136) and a crystallized structure of bound ESK1 (142). Furthermore, we chose to label the RMF peptide rather than ESK1 since labeling of the antibody may interfere with FcγR interactions with its Fc region, and therefore, the ability to activate ADCC.

Thus, the T2 human lymphoblastic cell line, which is positive for HLA-A*02:01, can be pulsed with the biotinylated RMF peptide (RMF-Biotin) and measured using a fluorophore labeled streptavidin. In order for this system to accurately measure antibody-binding events to the RMF-Biotin/HLA-A*02:01 complex, a number of criteria must be met. First, the RMF-Biotin peptide, which is much longer than the RMF 9-mer, must be successfully presented on empty MHC of the T2 cells, and second, ESK must retain its ability to bind to the RMF-Biotin/MHC complex. Therefore, we pulsed T2's with equivalent saturating molar amounts of the RMF and RMF-Biotin peptides overnight and stained them for ESK1 binding, streptavidin binding (SAv-PE), or both. RMF-Biotin pulsing of T2's allowed for ESK1 binding to T2 cells, as well as for staining with SAv-PE, indicating that the RMF-Biotin is successfully presented by T2 cells (Figure 26A). Simultaneous binding of ESK1 and SAv was also possible with the RMF-Biotin pulsed cells without decreasing the ESK1 binding signal, suggesting that neither the linker-biotin nor the SAv moieties interfere with ESK1 binding of RMF-Biotin (Figure 26B).

Furthermore, RMF and RMF-Biotin pulsed T2's showed similar binding curves for ESK1, with RMF-Biotin pulsed T2's showing slightly stronger ESK1 binding (Figure 26C). This confirms that ESK1 can bind efficiently to the RMF-Biotin/HLA-A*02:01 complex, just as it does the RMF/HLA-A*02:01 complex. To confirm that the

FIGURE 26

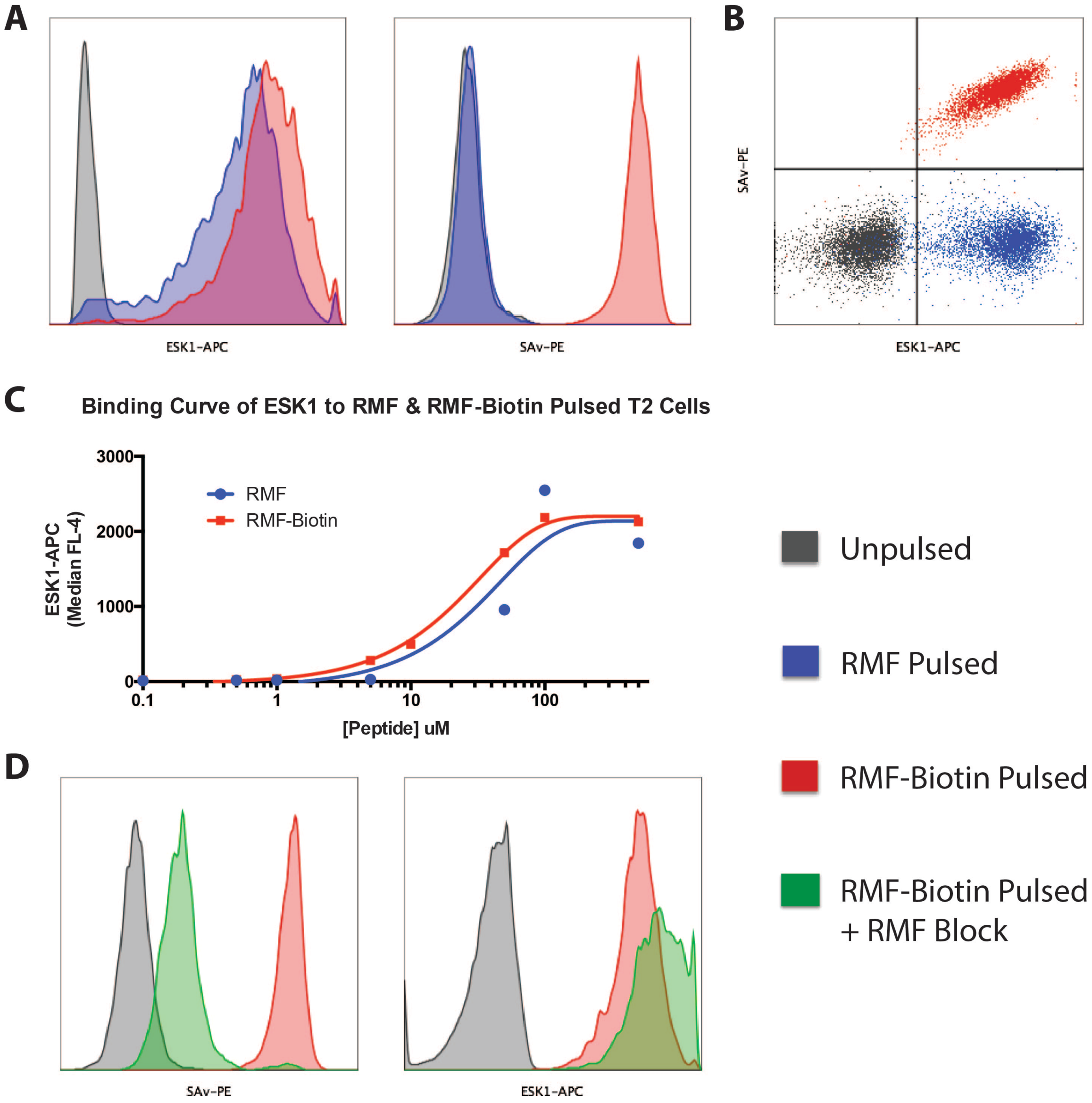

Figure 26: The RMF-Biotin peptide probe can be loaded onto MHC class I and be bound by ESK1 and streptavidin. A) T2 cells unpulsed (grey), RMF pulsed (blue) or RMF-Biotin pulsed (red) stained for ESK1 binding (left) or streptavidin binding (SAv, right). **B)** Simultaneous staining of T2 cells unpulsed (grey), RMF pulsed (blue) or RMF-Biotin pulsed (red) with ESK1-APC (x-axis) and SAv-PE (y-axis). **C)** Binding curve of ESK1-APC staining measured in median FL-4 signal of T2 cells pulsed with RMF (blue) or RMF-Biotin (red) at 1:2 fold successive dilutions of peptide concentrations (μM). **D)** T2 cells unpulsed (grey), RMF-Biotin pulsed (red), or RMF-Biotin pulsed with a 30X excess block of RMF peptide (green) stained with SAv-PE (left) and ESK1-APC (right) demonstrating the specificity of SAv staining.

streptavidin probe specifically interacts with the RMF-Biotin presented in the MHC class I binding groove, a blocking experiment was performed (Figure 26D). Excess RMF was able to greatly diminish the SAv-PE signal on RMF-Biotin pulsed T2's, confirming the specific interaction of the streptavidin probe with the RMF-Biotin. The slight increase in ESK1 binding in the RMF blocked T2 cells comes from the large increase in available peptide concentration. Thus far, the RMF-Biotin can successfully be pulsed onto T2 cells and, in complex with HLA-A*02:01, can be bound by ESK1; neither the linker-biotin nor the streptavidin interfere with pulsing or ESK1 binding and are specific.

A third criteria is that, since streptavidin is tetrameric and can bind multiple biotin molecules simultaneously, the ratio of SAv-PE signal to the number of bound ESK1 molecules must be 1:1. This will ensure that the quantitation of labeled streptavidin correlates directly with the number bound ESK1 antibodies. Therefore, we titrated down the concentration of RMF-Biotin pulsed onto T2 cells and stained the pulsed cells with either the SAv-PE probe or 1:1 labeled ESK1-PE. Using quantitative PE beads, we calculated the number of PE molecules bound per cell for the streptavidin or ESK1 stained samples (Figure 27). By plotting the number of complexes per cell for each pulsed concentration of RMF-Biotin against an $x=y$ line, we can see that a close linear relationship exists between the number of RMF-Biotin/HLA-A*02:01 complexes per cell measured by SAv-PE and ESK1-PE staining. Since antibodies are divalent and streptavidin is tetravalent, if either ESK1-PE or SAv-PE were binding in a manner other than monovalent, this close to perfect linear relationship would not be feasible. Therefore, the binding of the SAv-PE detection probe and the ESK1 mAb to RMF-

FIGURE 27

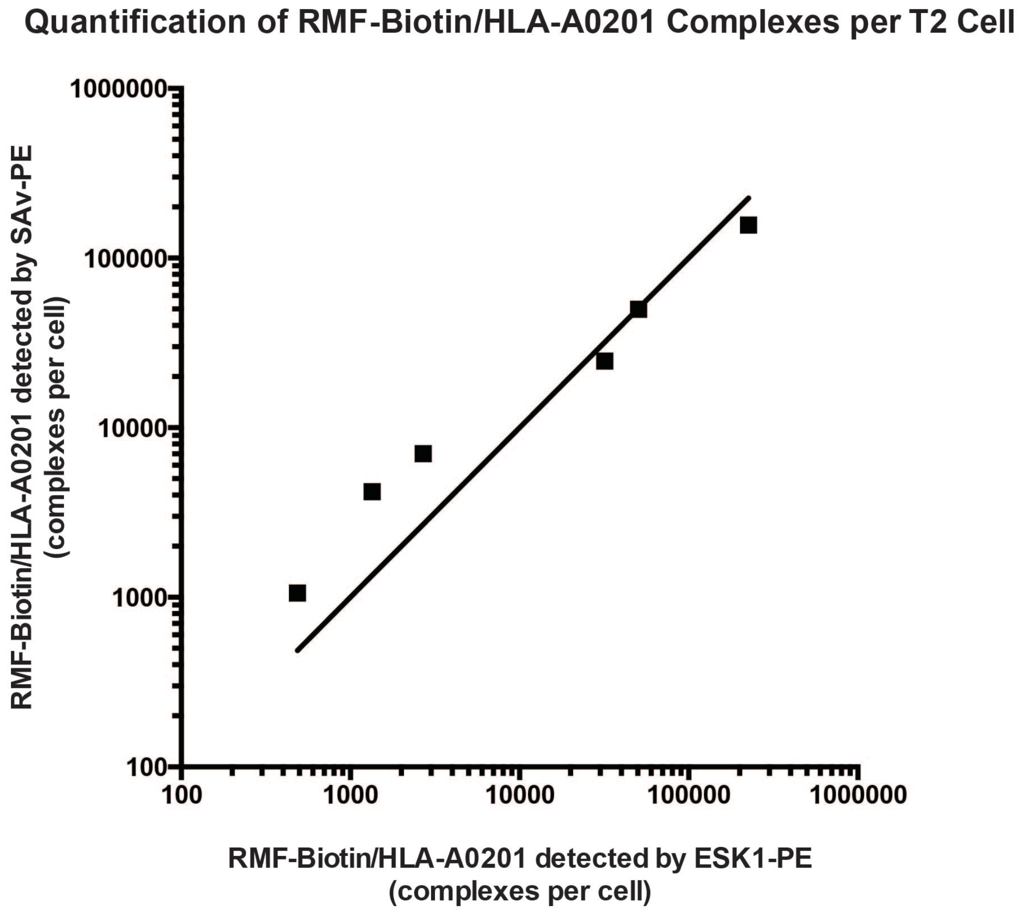

Figure 27: The quantitation of RMF-Biotin/HLA-A*02:01 complexes on pulsed T2 cells measured by ESK1 and streptavidin staining. T2 cells were pulsed with 1:2 successive dilutions of the RMF-Biotin peptide and stained with either ESK1-PE (x-axis) or streptavidin-PE (y-axis, SAv-PE). The number of PE molecules bound per cell was measured using the FL-2 geometric mean for either ESK1 or SAv-PE stained T2 cells at each RMF-Biotin concentration. The FL-2 geometric means were directly correlated to the number of PE molecules per cell using the standard curve equation of the quantitative PE beads simultaneously measured. The plotted line is $x=y$ used for reference.

Biotin/HLA-A*02:01 appear to both be in a 1:1 fashion, allowing for direct and equal correlation of bound SAv to ESK1. Thus, the level of the RMF-Biotin probe, as detected by fluorescently labeled SAv, can be used as a direct surrogate for the number of bound ESK1 antibodies, when present in excess, in these experiments.

Lastly, the RMF-Biotin peptide must not interfere with the ability of ESK to induce *in vitro* ADCC compared to the RMF peptide. Therefore, T2 cells were pulsed overnight with multiple equivalent molar concentrations of the RMF and RMF-Biotin peptide and tested for the ability to undergo ESK1 mediated ADCC *in vitro* (Figure 28). Both RMF and RMF-Biotin pulsed T2 experienced 50-60% specific lysis when treated with ESK1 in this *in vitro* ADCC assay, demonstrating that the biotin appendage does not interfere with ESK1 induced ADCC *in vitro*.

To determine the number of ESK1 antibodies required to promote ADCC, a 3D time-lapse confocal microscopic approach was used. In these experiments, the induction of target cell death by NK cells is our endpoint. NK cells were chosen as the immune effector cell in these experiments since NK cells isolated from human PBMCs are the only immune effector cell that have demonstrated robust *in vitro* ADCC in our hands. In order to detect target T2 cell death, we created stable T2 cell lines expressing two caspase-3 activatable FRET reporters, CFP-DEVD-YFP and Clover-DEVD-mRuby2. These reporters work by exciting the cells with lasers specific for the first fluorophore (CFP and Clover), while measuring emission of both fluorophores in the FRET pairs. Upon activation of ADCC, NK cells secrete vesicles towards their target cell, which, upon fusion with the target cell membrane, release granzymes into the target cell

FIGURE 28

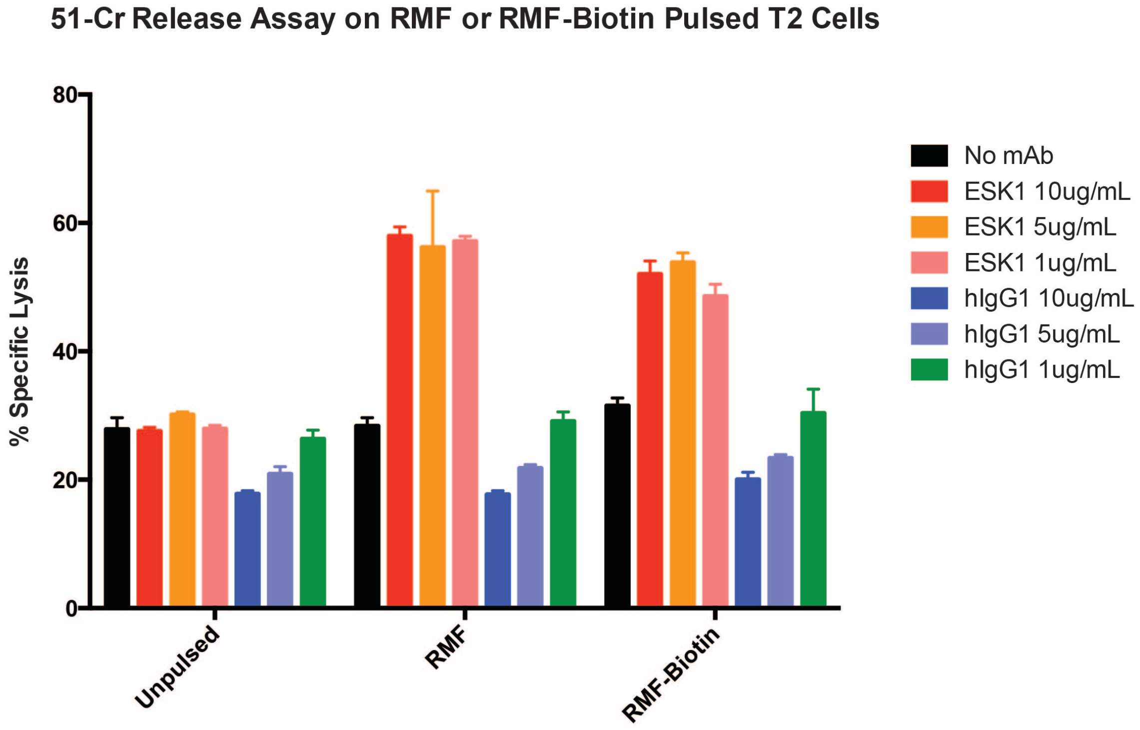

Figure 28: *In vitro* Cr-51 release assay on RMF and RMF-Biotin pulsed T2 cells mediated by ESK1. Cr-51 labeled T2 cells unpulsed, or pulsed with equivalent molar concentrations (50µM) of RMF or RMF-Biotin were co-incubated without antibody, with ESK1, or with an isotype control (hIgG1) and isolated PBMCs at an E:T ratio of 100:1. Three doses of ESK1 and hIgG1 antibody were used (10µg/mL, 5µg/mL, or 1µg/mL). Specific lysis was measured by subtracting spontaneous target T2 cell Cr-51 and used as a percentage of maximum target T2 cell Cr-51 release.

cytoplasm. Granzymes cleave a number of target proteins, including pro-caspase-3, resulting in the production of its active form, caspase-3 (143). The DEVD motif is a cleavage site for activated caspase-3. Thus, once the DEVD site is cleaved in either reporter vector, the two fluorophores separate. This results in a shift in fluorescence emission from CFP+ YFP+, for example, to CFP+ YFP-. Specifically, the CFP-DEVD-YFP FRET reporter has previously been used to observe granzyme B-mediated apoptotic cell death via cytotoxic T-cell activation (144-146). The same paradigm, however, is true for the Clover-DEVD-mRuby2 FRET reporter, and this pair of fluorophores is more photostable, therefore allowing for more frequent and longer image acquisition if necessary. Hence, separation of the FRET pairs upon DEVD cleavage indicates NK cell induced target cell death.

We began the confocal microscopy experiments using the T2 CFP-DEVD-YFP reporter cells since this reporter has previously been validated for similar purposes. Figure 29 demonstrates the expression of the FRET reporter in our T2 cells and that these cells retain the ability to be pulsed with the RMF-Biotin peptide, which can be bound by ESK1. Due to the emission wavelength of YFP and the lack of photostability of PE, the streptavidin probe in the confocal microscopy experiments is labeled with AlexaFluor 647 (AF647). We then wanted to verify that the SAv-AF647 detection probe can stain RMF-Biotin pulsed T2 cells and that this staining is stable at 37°C for time lapse experiments. Experiments were performed that demonstrated the stable detection of RMF-Biotin/HLA-A*02:01 bound by SAv-AF647 on T2 cell surfaces for up to 2 hours at 37°C without significant decreases in fluorescence intensity or observed internalization of the complex (Figure 30).

FIGURE 29

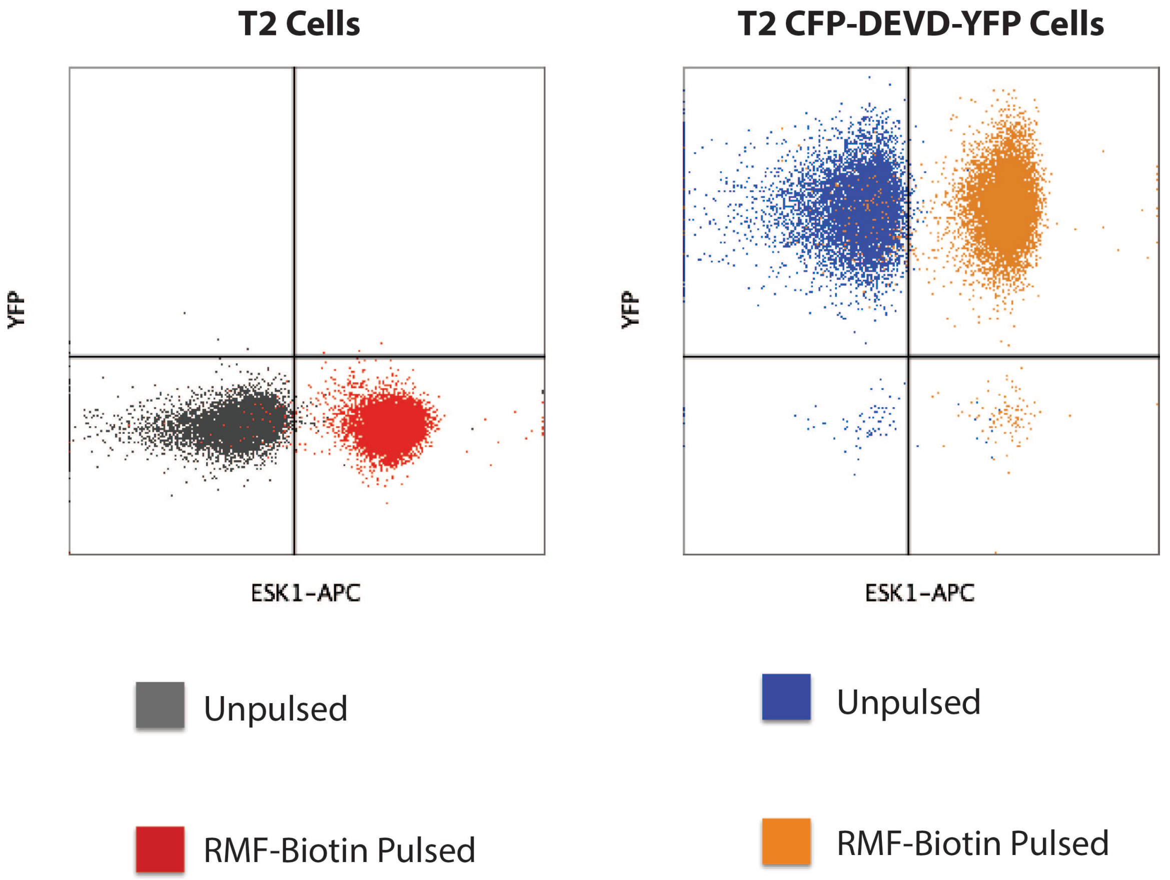

Figure 29: CFP-DEVD-YFP expressing T2 cells can be pulsed with RMF-Biotin. Parental T2 cells (left) and T2 CFP-DEVD-YFP expressing cells (right) unpulsed (grey and blue) or RMF-Biotin pulsed (red and orange) were stained with ESK1-APC to show surface detection of RMF-Biotin/HLA-A*02:01 complexes.

FIGURE 30

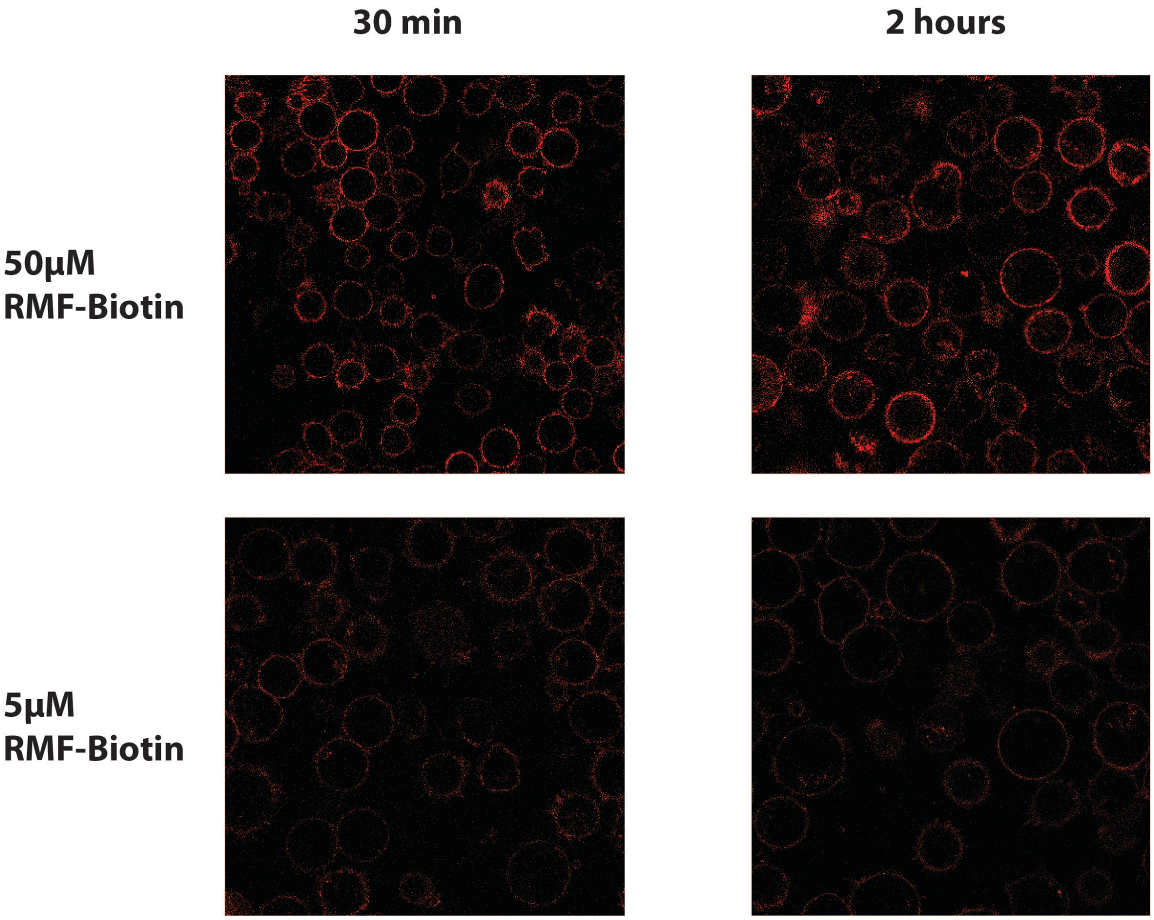

Figure 30: RMF-Biotin/HLA-A*02:01 complexes detected by SAv-AF647 are stable on the T2 cell surface. T2 cells were pulsed with either 50µM (top row) or 5µM (bottom row) RMF-Biotin overnight, labeled with SAv-AF647 (red), and plated in media for live-cell time-lapse confocal imaging. Images were taken at 30 min (left column) or 2 hours (right column) after incubation at 37°C.

In the first pilot experiment to verify the functionality of the CFP-YFP-DEVD FRET report in the target T2 cells in response to exposure to PBMCs upon ESK1 binding, a series of 30 min 3D confocal microscopy images were taken at multiple positions every 2 min, with excitation of CFP and AF647 and detection of CFP, YFP, and AF647 (Figure 31). Over the course of 40 min, a clear shift in CFP+YFP+ to CFP+YFP- was observed. However, this death happened rapidly, cell clustering impeded clear analysis of cell-cell interactions, and no immunological synapse formation between a target T2 cell and an immune effector cell prior to cell death was captured. However, this data was promising in that the CFP-DEVD-YFP vector appeared to be photostable and efficient at indicating cell death. Furthermore, it suggests that shorter windows for imaging might be necessary to capture an immunological synapse, allowing for more experiments to be performed in a shorter time frame.

However, this project came to a halt when RMF-Biotin pulsed T2 cells began to demonstrate inconsistent ESK1 and streptavidin binding. More rigorous testing of RMF-Biotin showed that this peptide no longer bound to streptavidin and weakly bound ESK1 compared RMF (Figure 32). New batches of the RMF-Biotin peptide ordered from the same company and reconstituted in several different manners did not restore ESK1 and streptavidin binding. Furthermore, a different company was used to produce this RMF-Biotin peptide, but it too failed to bind ESK1 or streptavidin after overnight T2 cell pulsing. The streptavidin probes were tested and found to successfully bind another biotinylated protein (data not shown). The peptides were screened for biotin degradation and were found to contain intact biotin (data not shown). HPLC and mass spectrometry of the peptides showed the correct molecular weight of intact peptide and correct

FIGURE 31

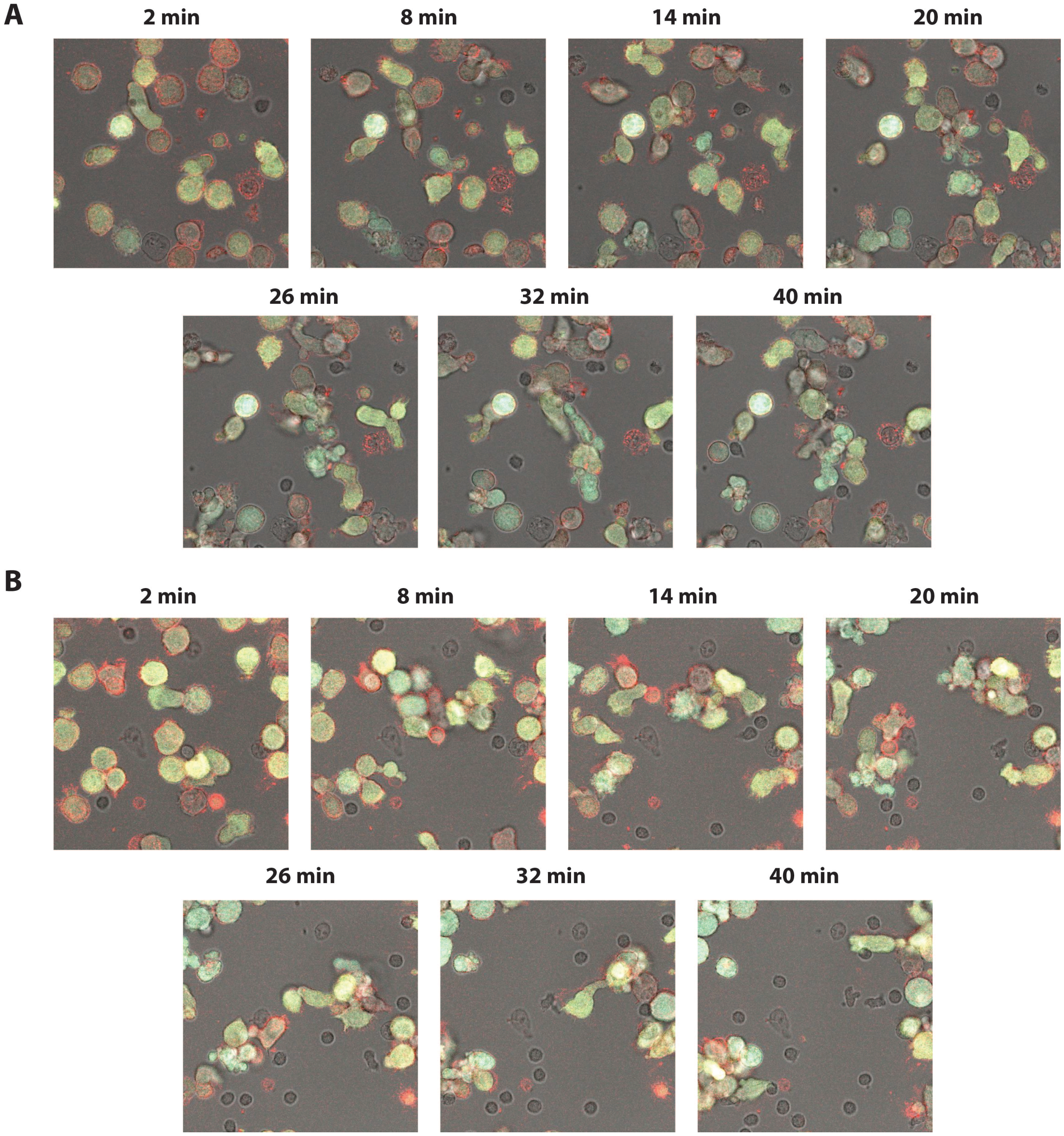

Figure 31: Time-lapse confocal microscopy of RMF-Biotin pulsed T2 CFP-DEVD-YFP cells bound by ESK1 and exposed the PBMCs. Position 1 **A)** and position 2 **B)** of RMF-Biotin pulsed T2 CFP-DEVD-YFP cells stained with SAv-AF647 (red). Unstained cells are the PBMCs added at a 1:1 E:T ratio. Cells were imaged every 2 min at each position with multiple z-stacks. For both positions, T2 cells show an obvious shift from yellow (YFP+) to blue (CFP+) indicating cleavage of the DEVD motif and separation of the FRET reporter. However, immunological synapse formation is not observed due to increased cell clustering over the 40 min time frame.

FIGURE 32

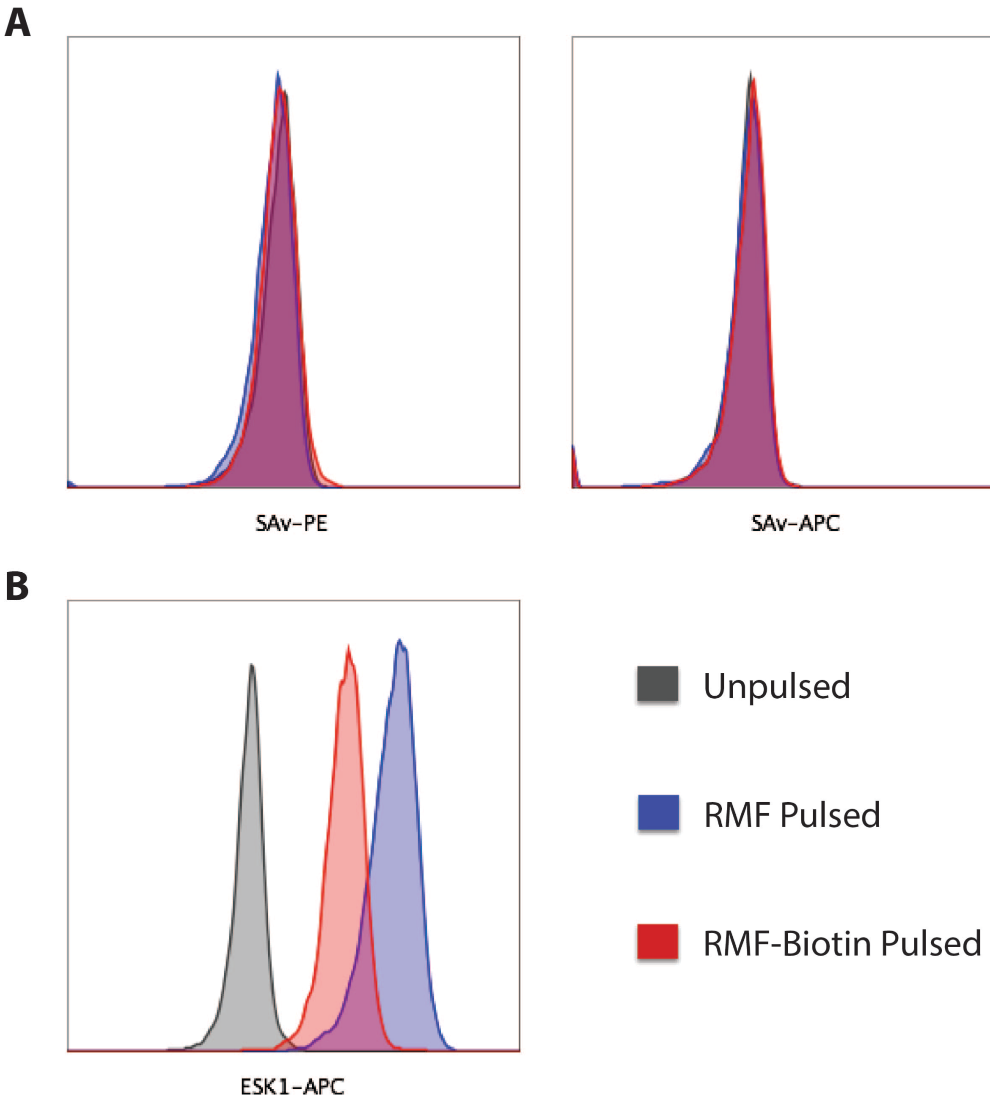

Figure 32: RMF-Biotin pulsed T2 cells no longer bind streptavidin labeled probes and have weaker ESK1 binding. A) T2 cells unpulsed (grey), RMF pulsed (blue) or RMF-Biotin pulsed (red) stained with SAv-PE (left) or SAv-APC (right). No positive staining is observed. **B)** T2 cells unpulsed (grey), RMF pulsed (blue) or RMF-Biotin pulsed (red) stained with ESK1-APC show weaker binding of ESK1 to RMF-Biotin pulsed T2 cells compared to RMF pulsed T2 cells.

composition for the expected sequence of the RMF-Biotin peptide, respectively (data not shown).

Therefore, new potential peptide probes were designed and screened to potentially replace RMF-Biotin (Table 7). The new peptides substitute the 8th amino acid in the RMF 9-mer from a tryrosine to a lysine residue, which has a long side chain with a terminal amine allowing for the addition of a biotin, a linker with a terminal biotin, or a direct fluorophore. The reason for this is that the 9th and final amino acid residue of the RMF 9-mer, leucine (L), is an anchor residue responsible for the binding of the RMF peptide in the binding groove of MHC class I. Therefore, it is possible that the biotin and linker could be interfering with RMF binding to MHC class I. The tyrosine in the RMF peptide slightly bulges out of the MHC class I binding pocket (Figure 25). Therefore, by switching it to a lysine reside, assuming that the new sequence (RMFPNAPKL [RMF-K]) still binds to HLA-A*02:01, interrupting the anchor residue interactions with MHC class I can be avoided.

The RMF-K-Biotin pulsing did not result in strong streptavidin staining despite high ESK1 binding, possibly due steric interference (Figure 33A). On the other hand, RMF-K-Cy5 pulsed T2 cells showed positive Cy5 signal, as well as ESK1 binding (Figure 33B). We further tested the RMF-K-Cy5 peptide probe for specificity and found that the peptide is highly internalized as well as presented on surface MHC class I, therefore resulting in high non-specific signal, which could not be blocked energetically (Figure 34). This is interesting since the mechanisms by which APC peptide pulsing results in MHC peptide presentation is highly disputed. However, these data suggest that

TABLE 7

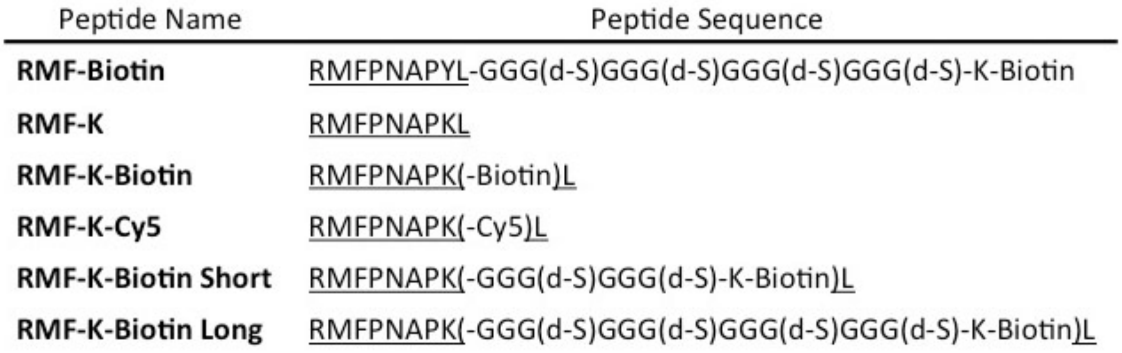

Peptide Name	Peptide Sequence
RMF-Biotin	RMFPNAPYL-GGG(d-S)GGG(d-S)GGG(d-S)GGG(d-S)-K-Biotin
RMF-K	RMFPNAPKL
RMF-K-Biotin	RMFPNAPK(-Biotin)L
RMF-K-Cy5	RMFPNAPK(-Cy5)L
RMF-K-Biotin Short	RMFPNAPK(-GGG(d-S)GGG(d-S)-K-Biotin)L
RMF-K-Biotin Long	RMFPNAPK(-GGG(d-S)GGG(d-S)GGG(d-S)GGG(d-S)-K-Biotin)L

Table 7: List of RMF peptide probe sequences designed for the quantification of ESK1 epitope number. The left column lists the shortened peptide name referred to in text, while the right column displays the full peptide sequence. The first row is the RMF-Biotin peptide originally designed and used, which is described in Figure 25. The second row is the RMF-K peptide that substitutes a lysine (K) for the tyrosine (Y) typically found in the WT1-derived RMF 9-mer. The remaining peptides in rows 3-6 are modifications of the RMF-K peptide. RMF-K-Biotin and RMF-K-Cy5 have a biotin or a Cy5 moiety directly attached to the amino group at the end of the R-chain of the 8th lysine. The RMF-K-Biotin Short and RMF-K-Biotin Long have different length biotinylated linkers attached to the amino group at the end of the R-chain of the 8th lysine.

FIGURE 33

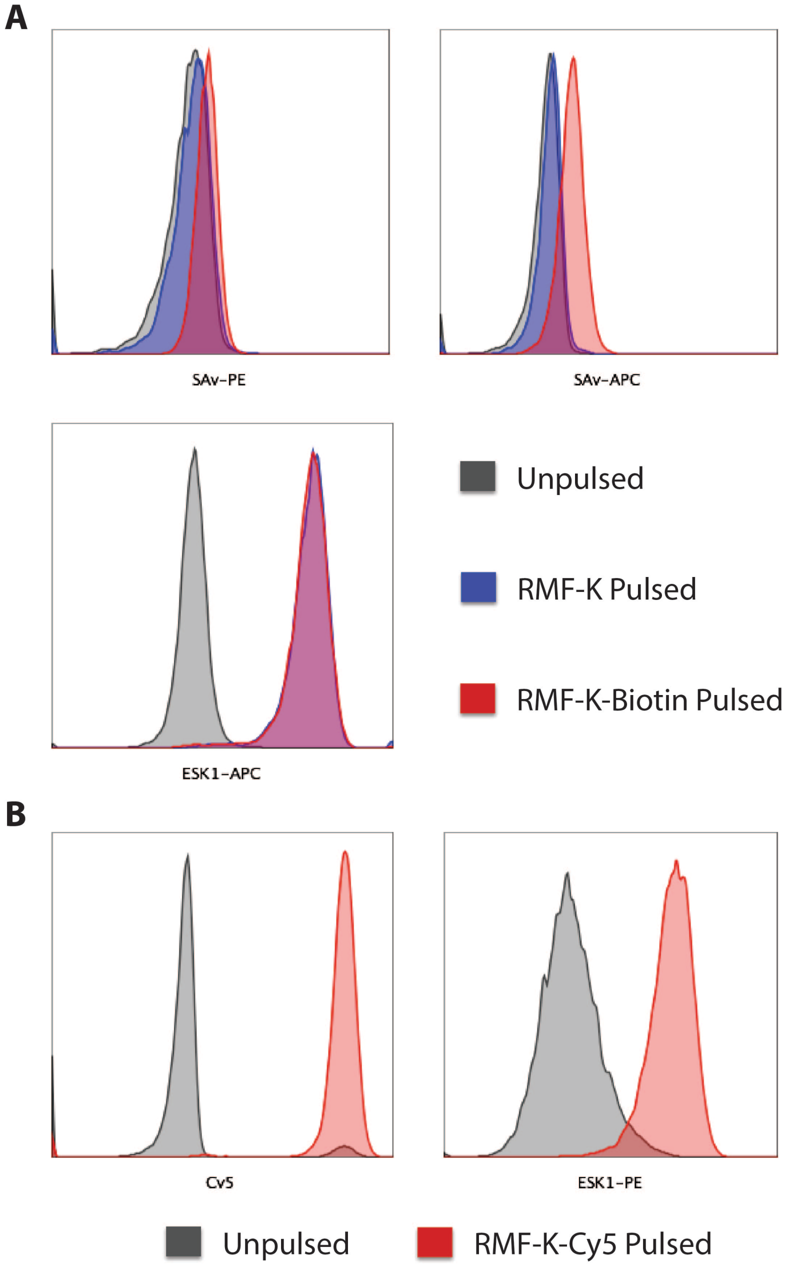

Figure 33: RMF-K-Biotin and RMF-K-Cy5 pulsing of T2 cells. A) T2 cells unpulsed (grey), RMF-K pulsed (blue), or RMF-K-Biotin pulsed (red) are stained with either streptavidin labeled with PE or APC (top row) or ESK1 (middle plot). RMF-K-Biotin pulsed T2s fail to show SAv-PE or SAv-APC staining despite equivalent staining of ESK1 compared to RMF-K pulsed T2s. **B)** T2 cells unpulsed (grey) or RMF-K-Cy5 pulsed (red) unstained (left) or stained with ESK1-PE (right). Unstained cells show high Cy5 signal in the RMF-K-Cy5 pulsed T2s, while ESK1-PE staining is also positive for the RMF-K-Cy5 pulsed cells compared to unpulsed.

FIGURE 34

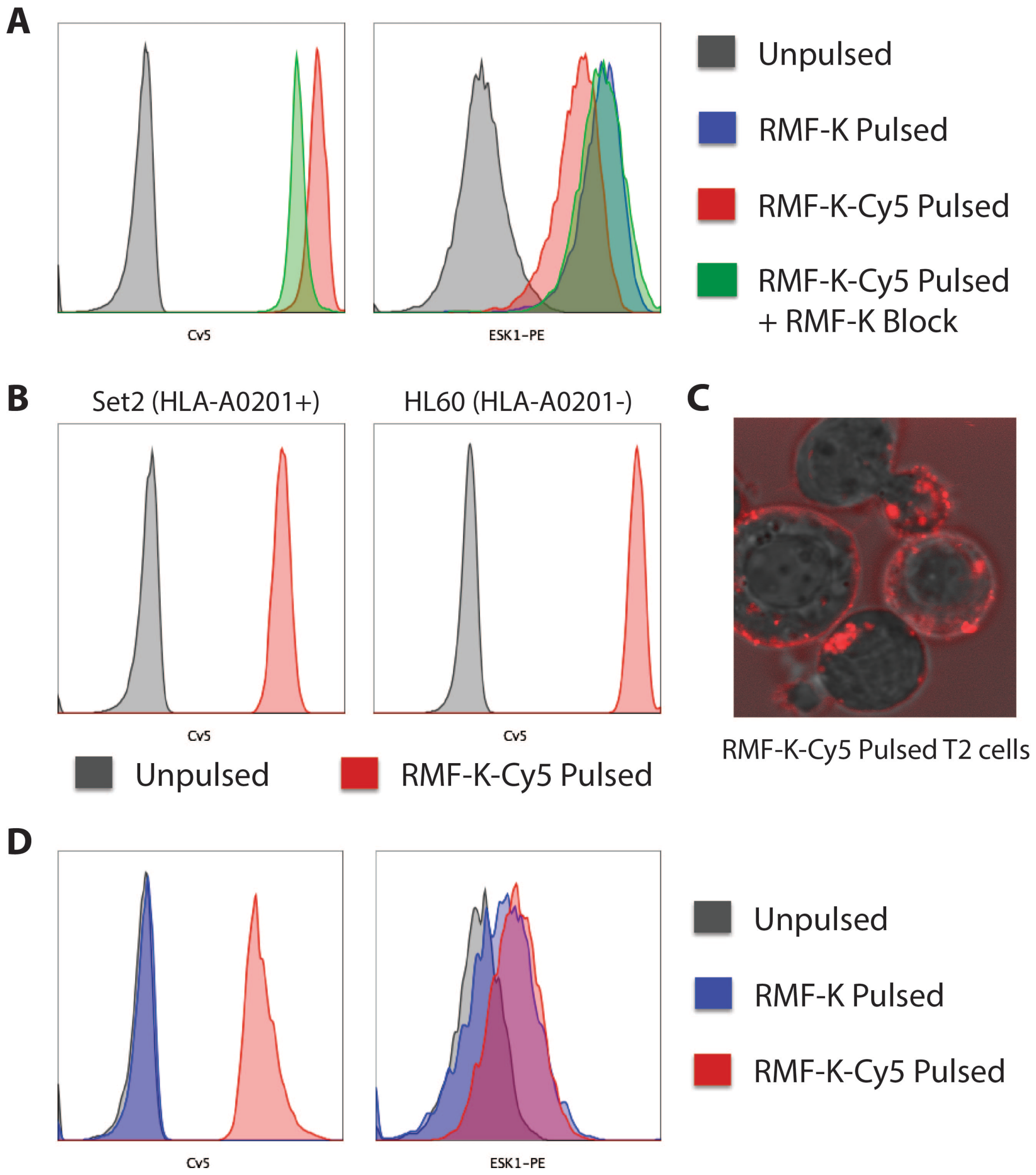

Figure 34: RMF-K-Cy5 is internalized into cells and results in nonspecific peptide/MHC signal. A) T2 cells unpulsed (grey), RMF-K pulsed (blue), RMF-K-Cy5 pulsed (red), or RMF-K-Cy5 pulsed with a 30X excess block of RMF-K peptide (green) unstained (left, Cy5) and stained with ESK1-PE (right) demonstrating the lack of specificity of the Cy5 signal. **B)** Set2 and HL-60 cells (HLA-A*02:01+ and -, respectively) pulsed with RMF-K-Cy5 to further show the lack of specificity of the Cy5 signal. **C)** Live cell confocal imaging of RMF-K-Cy5 pulsed T2 cells showing Cy5 signal (red) internalized into vesicles within the cells as well as presented on the cell surface. **D)** T2 cells unpulsed (grey), RMF-K pulsed (blue), or RMF-K-Cy5 pulsed (red) at 8 hours of pulsing at 4°C. Unstained (left, Cy5) or stained with ESK1 (right) show that the RMF-K-Cy5 peptide is still internalized and some of the RMF-K and RMF-K-Cy5 peptide is bound to HLA-A*02:01 on the cell surface, as detected by ESK1 binding.

peptides are highly internalized and that endosomal uptake may be the main mechanisms by which pulsed peptides are loaded onto MHC class I.

The next two peptides used to pulsed T2 cells were the RMF-K-Biotin Short and RMF-K-Biotin Long (Figure 35). Here both peptides showed superior ESK1 binding than the RMF-K pulsed T2 cells, as well as positive streptavidin binding. However, the RMF-K-Biotin Short showed higher SAv-PE signal. Therefore, this peptide was used to test for specificity. Upon blocking with excess RMF-K peptide, the SAv-PE signal disappeared, while the ESK1 binding remained, demonstrating specific biotin-streptavidin interaction and detection (Figure 35C). Next, the RMF-K-Biotin Short peptide was tested for 1:1 quantitation of peptide/MHC complexes by ESK1 and streptavidin to ensure accurate quantification of antibody binding events associated with SAv signal. However, there was not a 1:1 association of the number of ESK1 bound RMF-K-Biotin Short/HLA-A*02:01 complexes per cell and the number of complexes detected by streptavidin (Figure 36). Indeed, the SAv-PE signal decreased as the concentration of pulsed peptide increased, suggesting that streptavidin detection of this biotinylated peptide is ineffective.

Overall, these studies have shown that quantifying the number of antibodies required to bind its antigen for the induction of ADCC is feasible, but very technically challenging. The research produced in this thesis shows the impracticality of using a peptide probe to answer this question. It also clarifies key experimental points that will make the quantification of antibody-antigen interactions for ADCC more accurate, including using an adherent TAP-deficient cell lines for peptide pulsing to prevent cell clustering upon death and the use of purified human NK cells, or another effector cell, to clearly observe immunological synapse formation.

FIGURE 35

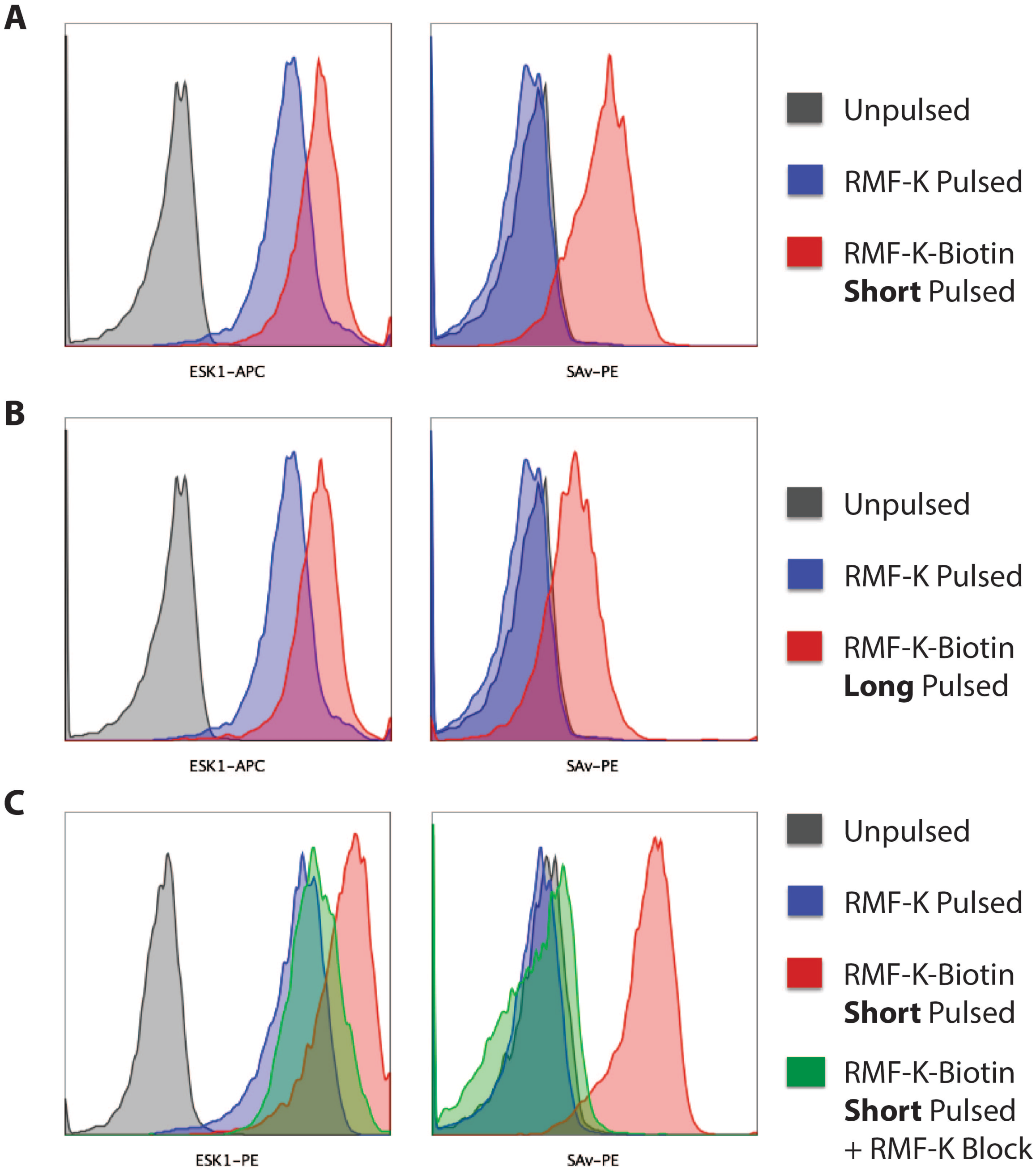

Figure 35: RMF-K-Biotin Short and RMF-K-Biotin Long pulsing of T2 cells. A) T2 cells unpulsed (grey), RMF-K pulsed (blue) or RMF-K-Biotin Short pulsed (red) stained for ESK1 binding (left) or streptavidin binding (SAv, right). **B)** T2 cells unpulsed (grey), RMF-K pulsed (blue) or RMF-K-Biotin Long pulsed (red) stained for ESK1 binding (left) or streptavidin binding (SAv, right). **C)** T2 cells unpulsed (grey), RMF-K pulsed (blue), RMF-K-Biotin Short pulsed (red), or RMF-K-Biotin Short pulsed with a 30X excess block of RMF-K peptide (green) stained with ESK1-PE (left) and SAv-PE (right) and demonstrating the specificity of SAv staining.

FIGURE 36

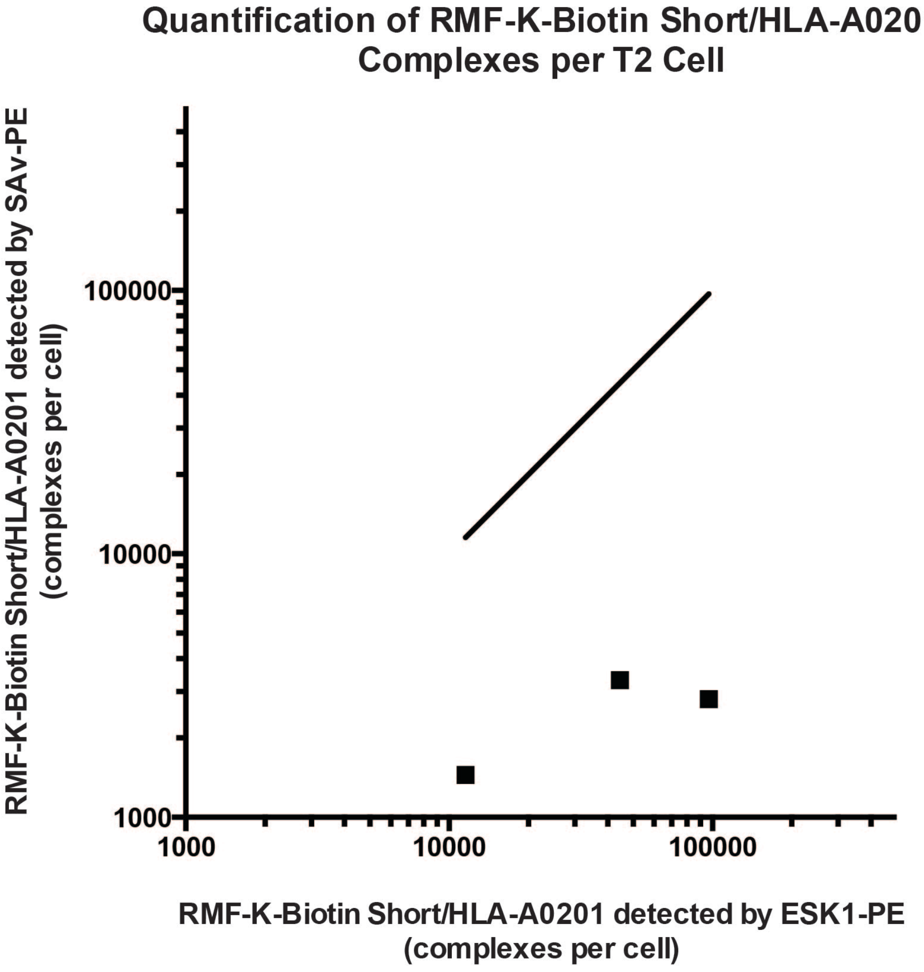

Figure 36: The quantitation of RMF-K-Biotin Short/HLA-A*02:01 complexes on pulsed T2 cells measured by ESK1 and streptavidin staining. T2 cells were pulsed with 1:2 successive dilutions of the RMF-Biotin peptide and stained with either ESK1-PE (x-axis) or streptavidin-PE (y-axis, SAv-PE). The number of PE molecules bound per cell was measured using the FL-2 geometric mean for either ESK1 or SAv-PE stained T2 cells at each RMF-Biotin concentration, and quantified using quantitative PE beads. The plotted line is *x*=*y* used for reference. The number of quantified complexes based of SAv-PE signal is significantly lower than the number of complexes quantified for the ESK1-PE signal.

Discussion

In this chapter, we sought to better understand the limitations of ADCC, and thus, therapeutic antibodies, by using a novel TCRm mAb, ESK1, in hopes to broaden the scope of potential antigenic targets applicable for this therapeutic modality. Despite clearly showing that ESK1 is solely dependent on ADCC for therapeutic function, quantification of the number of ESK1 antibodies necessary to bind its antigenic peptide/MHC complex and activate NK cells for ADCC has eluded us. This has been due to the technical challenge of developing a quantifiable probe for 3D confocal microscopy that directly correlates to peptide/MHC-antibody complex number.

The quantitative approach described here, based on previous reports for CD4+ and CD8+ T cell peptide/MHC complex quantification for activation (138,140), has relied on the use of biotinylated RMF peptides for T2 cell pulsing with subsequent fluorophore labeled streptavidin (SAv) binding. Early experiments showed the feasibility of this method with highly successful SAv and ESK1 binding of biotinylated RMF pulsed T2 cells, with a 1:1 ratio of the number of peptide/MHC complexes quantified by both SAv and ESK1 labeling. However, due to undetermined reasons, the use of this biotinylated RMF peptide began to show inconsistent ESK1 staining and a lack of SAv staining altogether. Redesign of the biotinylated or fluorophore labeled RMF peptide probe improved ESK1 binding and slightly improved SAv binding, but failed to give a 1:1 ratio between ESK1 and SAv quantified peptide/MHC complexes. This prevents movement forward by not allowing us to correlate SAv signal to the number of peptide/MHC complexes or bound ESK1 antibodies.

Therefore, different approaches are necessary to achieve this goal. Other mechanisms of ESK1 binding quantitation, such as radiolabeling and flow cytometry, have shown insufficient signal to noise ratios to be effective for this purpose. For example, in the radioimmunoassay originally quantifying the number of bound ESK1 antibodies to target cells, the range of ESK1 mAbs bound to BV173 cells overlaps with HLA-A*02:01- cell lines that are not killed in ADCC assays by ESK1 (136). Furthermore, flow cytometry of T2 cells pulsed with low amount of RMF peptide (5μM) barely shows ESK1 staining, but these cells can still be killed in ADCC assays. Thus the only approach that remains for quantifying the number of ESK1 antibodies required for cell killing by ADCC remains 3D confocal microscopy. Furthermore, significant advances in confocal microscopy have been made in recent years allowing for superior resolution by decreasing the diffraction limit. These methods, including structured illumination microscopy (SIM) and stochastic optical reconstruction microscopy (STORM), have much higher resolution, increasing the precision of fluorescence detection and thus allowing visualization on a much smaller scale.

In this case, we must revisit the direct labeling of ESK1 itself. Most antibodies are directly labeled via amine coupling. However, this process is random and thus, can significantly interfere with the ability of an FcγR to interact with the Fc region of an antibody to activate ADCC. Despite this, many new bright photostable dyes for single molecule fluorescent applications are small and can be used to label antibodies in specific molar ratios allowing for controlled labeling and the determination of the average number fluorophores per antibody. Although not exact, with enough measurements of minimum fluorescence for the formation of an immunological synapse between a target and effector cell for ADCC activation, a close estimate of the number of antibodies required for this event to take place is feasible. Furthermore, by limiting the molar ratio of fluorophore to antibody during the labeling process, we may be able to limit the disruption of key Fc-FcγR interacting residues in the labeling process. This can be tested using *in vitro* ADCC assays to with 1:2 successive dilutions of both labeled and unlabeled antibodies.

Another approach includes the labeling of free thiol groups after partial reduction of the disulfide bonds in the hinge region of the ESK1 antibody. The hinge region of a hIgG1 contains two disulfide bonds (four cysteine residues, two per heavy chain) between the heavy chains that are responsible for linking the two halves of the antibody. The remaining cysteine residues within the hIgG1 are buried, requiring further protein denaturing in order to access, or are involved in other inter- and intra-chain disulfide linkages that are harder to disrupt. Previous research has shown the feasibility of producing partially reduced hinge region antibodies with two accessible thiol groups for antibody drug conjugation (147). Although this approach has its own technical challenges, such as limiting the reduction conditions to disrupt a single disulfide linkage and ensuring antibody stability and retained antigen binding post-reduction and labeling, if feasible, it will allow for the controlled antibody labeling with minimal risk to Fc-FcγR binding disruption. Furthermore, many small, bright, photostable fluorophores already linked to sulfhydryl-reactive groups, including maleimides, exist and are readily available.

In addition to creating a quantifiable fluorescently labeled ESK1, other experimental considerations must be addressed. For example, T2 cell clustering in the time-lapse experiment prevented the clear identification of cell-to-cell contact between a

T2 cell and an effector cell. Furthermore, the freedom of movement of non-adherent cell lines makes decreasing T2 cell concentration impractical for this analysis due to the possibility of cell movement outside of the field of view. Another solution includes the creation of an adherent HLA-A*02:01+ TAP-deficient cell line. Efforts to do so in our lab have already begun using CRISPR/Cas9 to knockout both the TAP-1 and TAP-2 genes in the JMN human mesothelioma cell line. By doing so, we hope to create a new human adherent cell line that expresses empty MHC class I on its cell surface. This will allow us to moderate the number of RMF/HLA-A*02:01 complexes expressed on the surface of JMN cells via titrating pulsed RMF concentrations. We can then use these cells as our target cell line in this study in the same manner as we did the T2 cells but without the issue of cell clustering.

Furthermore, selecting CD56+ human NK cells from the isolated PBMCs before co-incubating with the antibody labeled target cells will allow for more efficient identification of important interactions. As seen in the pilot confocal microscopy study, the identification of important effector cells was impossible since there are B, T, and NK cells present in the PBMCs, as well as macrophages and monocytes. Determining which target-effector interactions are important in this setting is next to impossible since the NK cells are indistinguishable. Therefore, CD56 positive selection will isolate the relevant NK cells from the other effector cells, preventing this confusion in the future. I have previously shown that CD56 selection of NK cells does not interfere with ESK1-mediated ADCC on RMF pulsed T2 cells *in vitro* (data not shown).

In regards to ADCC activation readout, the CFP-DEVD-YFP FRET reporter can be expressed in the JMN TAP-deficient cell line for indication of caspase-3, and thus, granzyme B induced target cell death. However, although the CFP-DEVD-YFP FRET reporter has shown to work well for cytotoxic T cell activity in other contexts, due to the need to capture a transient interaction and quickly determine if that interaction results in activation, a readout of target cell death might have a long lag time and thus result in lost observations of the cell-to-cell interaction dynamics. Another readout approach is to modify a novel method for ADCC measurement. Recently, the Jurkat T cell line was modified to express both hFcγRIIIA and a luciferase reporter gene under the control of the NFAT regulatory elements of the IL-2 promoter (148). They showed that the luciferase reporter activity was directly correlated to Jurkat activation via hFcγRIIIA for ADCC and that the readout was specific and accurate. Since gene transcription and protein translation would take too long, if we could instead use this immortalized T cell expressing hFcγRIIIA as our effector cell, we can use calcium-influx, which activates NFAT for nuclear translocation and transcription, to rapidly determine T cell activation. Dyes, such as Fura-2, are often used to measure intracellular calcium levels, where increased fluorescence of these dyes indicates increased intracellular calcium, and this increased signaling. This is often used as a measure of T cell activation. Adopting these hFcγRIIIA+ Jurkat reporter cells as our effectors for ADCC activation readout will also remove the requirement for fresh PBMC isolation and NK cell selection. This will allow for these experiments to occur faster and more efficiently, increasing the turn around time between experiments.

Lastly, once the essential experimental parameters have been established (e.g. accurate ESK1 labeling without Fc-FcγR interference, quantification of ESK1 labeling, adherent HLA-A*02:01+ TAP-deficient target cells, and a rapid and clear readout for effector cell activation), a series of time-lapse 3D confocal microscopy using the new super-resolution microscopic tools will be performed. The adherent HLA-A*02:01+ TAP-deficient target cells will be plated the night before and pulsed with the RMF peptide. The following day, the labeled and functional ESK1 antibody will be titrated onto these pulsed cells and the effector cells will be added. Multiple target-effector cell interactions will be captured where the immunological synapse between the cells will be scanned and measured for ESK1 labeled fluorescence intensity while simultaneously measuring readout.

In order to correlate the ESK1 fluorescence signal to a specific number of ESK1 molecules the number of photons emitted by a single ESK1-labeled mAb must be measured. This can be done by adsorbing the labeled ESK1 onto poly-L-lysine coated slides at low concentrations and measuring the average signal intensity emitted by the diffraction-limited spots via photon scanning. With SIM and STORM microscopy methods, diffraction limits have been greatly reduced, thus reducing the limitations of this approach. By measuring and plotting the fluorescence intensity of each diffraction limited spot and using Poisson statistics for the occurrence of overlapping pairs or triplets of stochastically placed molecules, the signal intensity of a single labeled ESK1 mAb can be measured (149). Finally, we can correlate the signal intensity in immunological synapses to the likelihood of effector cell activation to determine the ultimate lower limit of ESK1 mAbs required in the synapse for ADCC activity. Other controls include using hIgG1 labeled antibody isotype controls to confirm specificity of effector cell activation as well as target cells pulsed with an irrelevant peptide HLA-A*02:01 present peptide to rule out non-specific ESK1 binding.

The 3D confocal imaging experiments proposed will also allow us to determine total number of antibodies bound per cell, as well as the pattern and density of the bound antibodies on the cell surface, in addition to the number of antibodies required within an immunological synapse for ADCC. Together, these data will allow us to predict mathematically—based on the total number of antibodies bound per cell and the density of these antibodies (e.g. clustered or dispersed)—the likelihood of activating an effector cell for ADCC by using the likelihood of the minimum required antibodies to be present in the immunological synapse. This predictive schema would be extremely useful for identifying the most promising epitopes to target for antibody therapy, which is especially relevant in the field of TCRm mAbs, thus directing future efforts for creating antibodies with the most therapeutic promise.

CONCLUSIONS

In this thesis, two major challenges facing therapeutic monoclonal antibody therapies to treat cancer are addressed. The first is the discrepancy between preclinical and clinical therapeutic antibody efficacy caused by inadequate preclinical models that do not accurately recapitulate the effector mechanisms employed by hIgG1 present in humans, thus resulting in misleading preclinical data with poor predictive power for clinical success. The second is the limited antigenic targets available for therapeutic antibody targeting due to a lack of understanding of the minimum number of epitopes required for an antibody to bind to induce target cell cytotoxicity and be therapeutically efficacious.

In chapter I, the newly established RHuFR mouse strains were created and characterized. The RHuFR mice were shown to express each of the human FcγRs on mouse leukocytes with the same pattern of expression as seen on human immune cell populations. They also were shown to lack the mouse FcγRs, as well as Rag2, which resulted in a clear loss of circulating B and T cells. These RHuFR mice were effective in a model of antibody-induced thrombocytopenia, indicating that the human FcγR network transgenically expressed in these mice are functionally active. The RHuFR single and combination “knockout” strains were also functionally intact. Furthermore, those mice with a hFcγRIIA “knockout” showed significantly reduced platelet depletion, indicating the role for this receptor in the mechanism by which platelets are depleted in this model. This supports the use of the RHuFR single and combination “knockout” mice for the identification of the receptors contributing to therapeutic antibody efficacy to eliminate cancer *in vivo*, allowing for targeted and more efficient Fc engineering efforts.

The RHuFR mice also proved to be superior to commercially available immunodeficient mouse models for predicting clinical outcomes. In the RHuFR^{1-} mice, obinutuzumab therapy demonstrated significantly improved therapeutic response and survival benefits that rituximab therapy for the treatment of a CD20+ human lymphoma, recapitulating the findings of a phase III clinical study comparing these two therapeutic antibodies (72). Meanwhile, the commercially available Rag2-/- mouse FcγR+ mice failed to demonstrate any difference in survival for mice treated with obinutuzumab compared to those treated with rituximab. Although follow-up studies using other therapeutic antibodies are necessary, this proof-of-concept study is highly compelling and emphasizes the potential utility of these RHuFR mice for predicting the clinical success of therapeutic anti-cancer antibodies at the preclinical stage.

Furthermore, the RHuFR mice are tools to expand our understanding of the complexity of the human FcγR network and how individual antibody targets (e.g. epitope, target cell type, microenvironment, etc.) can greatly shape the observed therapeutic effect for a given antibody. With the focus of the anti-cancer antibody community on Fc engineering to enhance efficacy, these RHuFR mice serve as a solution to the current preclinical testing problem. These Fc enhanced antibodies must be studied in settings where the human FcγRs they are engineered to are present in order to investigate their interaction with the receptor network, not just a single receptor, as well as how effector leukocyte expression of the receptors affects antibody activity. Studying these antibodies in the RHuFR mice will provide a more thorough understanding of their activity in a more accurate setting and help to better predict their action in humans.

In chapter II, the mechanism of action of a new TCRm antibody, ESK1, *in vivo* was explored by creating ESK mouse chimeric antibodies that have a high A/I ratio, low A/I ratio, or cannot bind FcγRs. In a mouse model of leukemia, only the ESK chimeric antibody with a high A/I ratio had a significant therapeutic effect, while the ESK chimeric antibodies with a low A/I ratio and the antibody unable to engage FcγRs showed little to no therapeutic benefit, respectively. This confirmed *in vitro* data demonstrating that ESK1 exerts therapeutic action exclusively via the engagement of FcγRs to initiate ADCC. Therefore, ESK1 is the first human TCRm mAb that has strong therapeutic activity *in vivo* and acts solely through ADCC.

ESK1 was found to have limited antigenic targets, ranging from 750-6,500 ESK1 antibodies bound to WT1+ HLA-A*02:01+ cancer cell lines. Furthermore, the Ph+ ALL cell line used in the therapy models *in vivo*, BV173, was on the lower end of this range, with an average of 750 ESK1 antibodies bound per cell, and some with as low as 500 mAbs per cell. Therefore, we used the ESK1 antibody to explore the lower limit of antigen number for the activation of ADCC by human NK cells *in vitro*. In order to quantify the number of antibodies required to initiate ADCC in an effector cell, 3D confocal microscopy was used. Other methods for quantifying ESK1 mAbs bound per cell and detecting ADCC, flow cytometry and radioisotope counting, have high signal-to-noise ratios that prevent the quantification of this biological process at a single cell level. Furthermore, similar efforts to quantify the number of epitopes for CD4+ and CD8+ T cells for activation proved successful.

Therefore, the TAP-deficient T2 human lymphoblastic cell line expressing empty HLA-A*02:01 on its surface was pulsed with a biotinylated RMF peptide. Initially, this RMF-Biotin peptide proved equivalent to the normal RMF peptide for binding to HLA-A*02:01, as well as for binding ESK1 once presented. RMF-Biotin pulsed T2 cells also showed strong binding of a fluorophore labeled streptavidin for detection, and quantification of RMF-Biotin/HLA-A*02:01 complexes on the T2 cell surface by ESK1 and SAv probes showed a 1:1 correlation, allowing for the quantification of SAv to directly represent the number of epitopes and ESK1 antibodies bound per cell. However, these data were not repeatable with new batches of RMF-Biotin, and newly designed probes failed to recapitulate these key controls.

Despite these failings, a few key experimental points were clarified for answering this question. First, ESK1 must be directly modified with a fluorophore for exact quantitation without the disruption of antigenic binding or Fc-FcγR interactions to initiate ADCC. Although achieving this might be technically challenging, labeling of the RMF peptide has proven to be unreliable, thus requiring this step for successful quantitation. Second, using an adherent target cell line will make the imaging of the interaction between an ESK1-bound target cell and an effector NK cell easier and more efficient by avoiding cell clustering without decreasing the number of cells, thus increasing the likelihood of capturing immunological synapse formation. Lastly, a clear readout of the activation of ADCC is necessary and must occur rapidly once FcγR engagement occurs. The CFP-DEVD-YFP FRET reporter expressed in the T2 cells clearly indicated the activation of cell death over the 40 min time frame of the pilot study, despite no observations of immunological synapse formation. This suggests that target cell death is occurring rapidly and this readout may not be fast enough for the clear identification of effector cell activation. Other methods, such as calcium influx within an effector cell, may be necessary to identify activated cells and thus, immunological synapse formation.

Overall, this thesis has sought to give the scientific community, especially for those involved in cancer immunotherapy, a greater understanding for conceiving new therapeutic cancer antibody targets outside the traditional landscape as well as improved tools for testing those novel therapeutic antibodies to probe their mechanism of action and predict their clinical success in patients with cancer.

BIBLIOGRAPHY

1. Rettig, W.J., *et al.* (1989) Immunogenetics of Human Cell Surface Differentiation. *Annual Review of Immunology*, **7**, 481-511.

2. Melchers, F. (1998) Antibodies, Synthesis A2 - Delves, Peter J. In *Encyclopedia of Immunology (Second Edition)*. Elsevier, Oxford, pp. 154-158.

3. Wang, D., *et al.* (1998) Antibodies, Specificity A2 - Delves, Peter J. In *Encyclopedia of Immunology (Second Edition)*. Elsevier, Oxford, pp. 148-154.

4. Thanavala, Y. (1998) Antiserum A2 - Delves, Peter J. In *Encyclopedia of Immunology (Second Edition)*. Elsevier, Oxford, pp. 218-220.

5. Lipman, N.S., *et al.* (2005) Monoclonal Versus Polyclonal Antibodies: Distinguishing Characteristics, Applications, and Information Resources. *ILAR Journal*, **46**, 258-268.

6. Köhler, G., *et al.* (1975) Continuous cultures of fused cells secreting antibody of predefined specificity. *nature*, **256**, 495-497.

7. Group, T.O.M.T.S. (1985) A Randomized Clinical Trial of OKT3 Monoclonal Antibody for Acute Rejection of Cadaveric Renal Transplants. *New England Journal of Medicine*, **313**, 337-342.

8. Kimball, J.A., *et al.* (1995) The OKT3 antibody response study: a multicentre study of human anti-mouse antibody (HAMA) production following OKT3 use in solid organ tranplantation. *Transplant Immunology*, **3**, 212-221.

9. Morrison, S.L., *et al.* (1984) Chimeric human antibody molecules: mouse antigen-binding domains with human constant region domains. *Proceedings of the National Academy of Sciences of the United States of America*, **81**, 6851-6855.

10. Padlan, E.A. (1991) A possible procedure for reducing the immunogenicity of antibody variable domains while preserving their ligand-binding properties. *Molecular Immunology*, **28**, 489-498.

11. Jones, P.T., *et al.* (1986) Replacing the complementarity-determining regions in a human antibody with those from a mouse. *Nature*, **321**, 522-525.

12. Bazan, J., *et al.* (2012) Phage display—A powerful technique for immunotherapy: 1. Introduction and potential of therapeutic applications. *Human Vaccines & Immunotherapeutics*, **8**, 1817-1828.

13. Maloney, D.G., *et al.* (1997) IDEC-C2B8 (Rituximab) Anti-CD20 Monoclonal Antibody Therapy in Patients With Relapsed Low-Grade Non-Hodgkin's Lymphoma. *Blood*, **90**, 2188.

14. Reff, M.E., *et al.* (1994) Depletion of B cells in vivo by a chimeric mouse human monoclonal antibody to CD20. *Blood*, **83**, 435.

15. Harrison, A.M., *et al.* (2014) Rituximab for Non-Hodgkin's Lymphoma: A Story of Rapid Success in Translation. *Clinical and translational science*, **7**, 82-86.

16. Cobleigh, M.A., *et al.* (1999) Multinational Study of the Efficacy and Safety of Humanized Anti-HER2 Monoclonal Antibody in Women Who Have HER2-Overexpressing Metastatic Breast Cancer That Has Progressed After Chemotherapy for Metastatic Disease. *Journal of Clinical Oncology*, **17**, 2639-2639.

17. Carter, P., *et al.* (1992) Humanization of an anti-p185HER2 antibody for human cancer therapy. *Proceedings of the National Academy of Sciences of the United States of America*, **89**, 4285-4289.

18. Cunningham, D., *et al.* (2004) Cetuximab Monotherapy and Cetuximab plus Irinotecan in Irinotecan-Refractory Metastatic Colorectal Cancer. *New England Journal of Medicine*, **351**, 337-345.

19. Saltz, L.B., *et al.* (2004) Phase II Trial of Cetuximab in Patients With Refractory Colorectal Cancer That Expresses the Epidermal Growth Factor Receptor. *Journal of Clinical Oncology*, **22**, 1201-1208.

20. Sutherland, M.K., *et al.* (2009) Anti-leukemic activity of lintuzumab (SGN-33) in preclinical models of acute myeloid leukemia. *mAbs*, **1**, 481-490.

21. Ebel, W., *et al.* (2007) Preclinical evaluation of MORAb-003, a humanized monoclonal antibody antagonizing folate receptor-alpha. *Cancer Immunity : a Journal of the Academy of Cancer Immunology*, **7**, 6.

22. Wahl, A.F., *et al.* (2002) The Anti-CD30 Monoclonal Antibody SGN-30 Promotes Growth Arrest and DNA Fragmentation in Vitro and Affects Antitumor Activity in Models of Hodgkin's Disease. *Cancer Research*, **62**, 3736-3742.

23. Borchmann, P., *et al.* (2003) The human anti-CD30 antibody 5F11 shows in vitro and in vivo activity against malignant lymphoma. *Blood*, **102**, 3737-42.

24. Naundorf, S., *et al.* (2002) In vitro and in vivo activity of MT201, a fully human monoclonal antibody for pancarcinoma treatment. *Int J Cancer*, **100**, 101-10.

25. Feldman, E.J., *et al.* (2005) Phase III randomized multicenter study of a humanized anti-CD33 monoclonal antibody, lintuzumab, in combination with

chemotherapy, versus chemotherapy alone in patients with refractory or first-relapsed acute myeloid leukemia. *J Clin Oncol*, **23**, 4110-6.

26. Sekeres, M.A.*, et al.* (2013) Randomized phase IIb study of low-dose cytarabine and lintuzumab versus low-dose cytarabine and placebo in older adults with untreated acute myeloid leukemia. *Haematologica*, **98**, 119-28.

27. Vergote, I.*, et al.* (2016) A Randomized, Double-Blind, Placebo-Controlled, Phase III Study to Assess Efficacy and Safety of Weekly Farletuzumab in Combination With Carboplatin and Taxane in Patients With Ovarian Cancer in First Platinum-Sensitive Relapse. *J Clin Oncol*.

28. Forero-Torres, A.*, et al.* (2009) A Phase II study of SGN-30 (anti-CD30 mAb) in Hodgkin lymphoma or systemic anaplastic large cell lymphoma. *Br J Haematol*, **146**, 171-9.

29. Ansell, S.M.*, et al.* (2007) Phase I/II study of an anti-CD30 monoclonal antibody (MDX-060) in Hodgkin's lymphoma and anaplastic large-cell lymphoma. *J Clin Oncol*, **25**, 2764-9.

30. Schmidt, M.*, et al.* (2010) An open-label, randomized phase II study of adecatumumab, a fully human anti-EpCAM antibody, as monotherapy in patients with metastatic breast cancer. *Ann Oncol*, **21**, 275-82.

31. Hay, M.*, et al.* (2014) Clinical development success rates for investigational drugs. *Nat Biotech*, **32**, 40-51.

32. Pedersen, I.M.*, et al.* (2002) The chimeric anti-CD20 antibody rituximab induces apoptosis in B-cell chronic lymphocytic leukemia cells through a p38 mitogen activated protein–kinase–dependent mechanism. *Blood*, **99**, 1314.

33. Belyanskaya, L.L.*, et al.* (2007) Human agonistic TRAIL receptor antibodies Mapatumumab and Lexatumumab induce apoptosis in malignant mesothelioma and act synergistically with cisplatin. *Molecular Cancer*, **6**, 66-66.

34. Khalil, M.*, et al.* (2007) Anti-CD40 agonist antibodies: preclinical and clinical experience. *Update on cancer therapeutics*, **2**, 61-65.

35. Yakes, F.M.*, et al.* (2002) Herceptin-induced Inhibition of Phosphatidylinositol-3 Kinase and Akt Is Required for Antibody-mediated Effects on p27, Cyclin D1, and Antitumor Action. *Cancer Research*, **62**, 4132.

36. Perez-Torres, M.*, et al.* (2006) Epidermal Growth Factor Receptor (EGFR) Antibody Down-regulates Mutant Receptors and Inhibits Tumors Expressing EGFR Mutations. *Journal of Biological Chemistry*, **281**, 40183-40192.

37. Rogers, L.M.*, et al.* (2014) Complement in Monoclonal Antibody Therapy of Cancer. *Immunologic research*, **59**, 203-210.

38. Nimmerjahn, F.*, et al.* (2008) Fcγ receptors as regulators of immune responses. *Nat Rev Immunol*, **8**, 34-47.

39. Smyth, M.J.*, et al.* (2005) Activation of NK cell cytotoxicity. *Molecular Immunology*, **42**, 501-510.

40. Nuray, G.*, et al.* (2014) Macrophages eliminate circulating tumor cells after monoclonal antibody therapy. *The Journal of Clinical Investigation*, **124**, 812-823.

41. Herter, S.*, et al.* (2014) Glycoengineering of Therapeutic Antibodies Enhances Monocyte/Macrophage-Mediated Phagocytosis and Cytotoxicity. *The Journal of Immunology Author Choice*, **192**, 2252-2260.

42. Uribe-Querol, E.*, et al.* (2015) Neutrophils in Cancer: Two Sides of the Same Coin. *Journal of Immunology Research*, **2015**, 21.

43. Nimmerjahn, F.*, et al.* (2005) Divergent Immunoglobulin G Subclass Activity Through Selective Fc Receptor Binding. *Science*, **310**, 1510-1512.

44. Stewart, R.*, et al.* (2014) The role of Fc gamma receptors in the activity of immunomodulatory antibodies for cancer. *Journal for ImmunoTherapy of Cancer*, **2**, 29.

45. Diamantis, N.*, et al.* (2016) Antibody-drug conjugates—an emerging class of cancer treatment. *British Journal of Cancer*, **114**, 362-367.

46. Huehls, A.M.*, et al.* (2015) Bispecific T cell engagers for cancer immunotherapy. *Immunology and cell biology*, **93**, 290-296.

47. Fesnak, A.D.*, et al.* (2016) Engineered T cells: the promise and challenges of cancer immunotherapy. *Nat Rev Cancer*, **16**, 566-581.

48. Viardot, A.*, et al.* (2016) Phase 2 study of the bispecific T-cell engager (BiTE) antibody blinatumomab in relapsed/refractory diffuse large B-cell lymphoma. *Blood*, **127**, 1410-1416.

49. Brentjens, R.*, et al.* (2013) CD19-targeted T cells rapidly induce molecular remissions in adults with chemotherapy-refractory acute lymphoblastic leukemia. *Science translational medicine*, **5**, 177ra38-177ra38.

50. Cragg, M.S.*, et al.* (2004) Antibody specificity controls in vivo effector mechanisms of anti-CD20 reagents. *Blood*, **103**, 2738.

51. Beers, S.A.*, et al.* (2008) Type II (tositumomab) anti-CD20 monoclonal antibody out performs type I (rituximab-like) reagents in B-cell depletion regardless of complement activation. *Blood*, **112**, 4170.

52. Wang, S.-Y*., et al.* (2009) Depletion of the C3 component of complement enhances the ability of rituximab-coated target cells to activate human NK cells and improves the efficacy of monoclonal antibody therapy in an in vivo model. *Blood*, **114**, 5322.

53. Otten, M.A*., et al.* (2008) Experimental Antibody Therapy of Liver Metastases Reveals Functional Redundancy between FcγRI and FcγRIV. *The Journal of Immunology*, **181**, 6829.

54. Clynes, R.A*., et al.* (2000) Inhibitory Fc receptors modulate in vivo cytoxicity against tumor targets. *Nat Med*, **6**, 443-446.

55. Simpson, T.R*., et al.* (2013) Fc-dependent depletion of tumor-infiltrating regulatory T cells co-defines the efficacy of anti-CTLA-4 therapy against melanoma. *J Exp Med*, **210**.

56. Weng, W.-K*., et al.* (2003) Two Immunoglobulin G Fragment C Receptor Polymorphisms Independently Predict Response to Rituximab in Patients With Follicular Lymphoma. *Journal of Clinical Oncology*, **21**, 3940-3947.

57. Zhang, W*., et al.* (2007) FCGR2A and FCGR3A Polymorphisms Associated With Clinical Outcome of Epidermal Growth Factor Receptor–Expressing Metastatic Colorectal Cancer Patients Treated With Single-Agent Cetuximab. *Journal of Clinical Oncology*, **25**, 3712-3718.

58. Musolino, A*., et al.* (2008) Immunoglobulin G Fragment C Receptor Polymorphisms and Clinical Efficacy of Trastuzumab-Based Therapy in Patients With HER-2/neu–Positive Metastatic Breast Cancer. *Journal of Clinical Oncology*, **26**, 1789-1796.

59. Bibeau, F*., et al.* (2009) Impact of FcγRIIa-FcγRIIIa Polymorphisms and KRAS Mutations on the Clinical Outcome of Patients With Metastatic Colorectal Cancer Treated With Cetuximab Plus Irinotecan. *Journal of Clinical Oncology*, **27**, 1122-1129.

60. Tamura, K*., et al.* (2011) FcγR2A and 3A polymorphisms predict clinical outcome of trastuzumab in both neoadjuvant and metastatic settings in patients with HER2-positive breast cancer. *Annals of Oncology*, **22**, 1302-1307.

61. Racila, E*., et al.* (2008) A Polymorphism in the Complement Component C1qA Correlates with Prolonged Response Following Rituximab Therapy of Follicular Lymphoma. *Clinical Cancer Research*, **14**, 6697-6703.

62. Wang, S.-Y*., et al.* (2008) NK-cell activation and antibody-dependent cellular cytotoxicity induced by rituximab-coated target cells is inhibited by the C3b component of complement. *Blood*, **111**, 1456-1463.

63. Nimmerjahn, F.*, et al.* (2012) Translating basic mechanisms of IgG effector activity into next generation cancer therapies. *Cancer Immunity*, **12**, 13.

64. Shields, R.L.*, et al.* (2001) High Resolution Mapping of the Binding Site on Human IgG1 for FcγRI, FcγRII, FcγRIII, and FcRn and Design of IgG1 Variants with Improved Binding to the FcγR. *Journal of Biological Chemistry*, **276**, 6591-6604.

65. Lazar, G.A.*, et al.* (2006) Engineered antibody Fc variants with enhanced effector function. *Proc Natl Acad Sci U S A*, **103**.

66. Kubota, T.*, et al.* (2009) Engineered therapeutic antibodies with improved effector functions. *Cancer Sci*, **100**, 1566-72.

67. Peipp, M.*, et al.* (2008) Antibody fucosylation differentially impacts cytotoxicity mediated by NK and PMN effector cells. *Blood*, **112**, 2390.

68. Junttila, T.T.*, et al.* (2010) Superior In vivo Efficacy of Afucosylated Trastuzumab in the Treatment of HER2-Amplified Breast Cancer. *Cancer Research*, **70**, 4481-4489.

69. Gerdes, C.A.*, et al.* (2013) GA201 (RG7160): A Novel, Humanized, Glycoengineered Anti-EGFR Antibody with Enhanced ADCC and Superior In Vivo Efficacy Compared with Cetuximab. *Clinical Cancer Research*, **19**, 1126-1138.

70. Ferrara, C.*, et al.* (2006) Modulation of therapeutic antibody effector functions by glycosylation engineering: Influence of Golgi enzyme localization domain and co-expression of heterologous β1, 4-N-acetylglucosaminyltransferase III and Golgi α-mannosidase II. *Biotechnology and Bioengineering*, **93**, 851-861.

71. Mossner, E.*, et al.* (2010) Increasing the efficacy of CD20 antibody therapy through the engineering of a new type II anti-CD20 antibody with enhanced direct and immune effector cell-mediated B-cell cytotoxicity. *Blood*, **115**, 4393-402.

72. Goede, V.*, et al.* (2014) Obinutuzumab plus chlorambucil in patients with CLL and coexisting conditions. *N Engl J Med*, **370**, 1101-10.

73. Nimmerjahn, F.*, et al.* (2007) Fc‑Receptors as Regulators of Immunity. In *Advances in Immunology*. Academic Press, vol. Volume 96, pp. 179-204.

74. Hamaguchi, Y.*, et al.* (2006) Antibody isotype-specific engagement of Fcγ receptors regulates B lymphocyte depletion during CD20 immunotherapy. *The Journal of Experimental Medicine*, **203**, 743-753.

75. Nimmerjahn, F.*, et al.* (2005) FcγRIV: A Novel FcR with Distinct IgG Subclass Specificity. *Immunity*, **23**, 41-51.

76. Veeramani, S., *et al.* (2011) Rituximab infusion induces NK activation in lymphoma patients with the high-affinity CD16 polymorphism. *Blood*, **118**, 3347-3349.

77. Weng, W.-K., *et al.* (2009) Genetic polymorphism of the inhibitory IgG Fc receptor FcγRIIb is not associated with clinical outcome in patients with follicular lymphoma treated with rituximab. *Leukemia & lymphoma*, **50**, 723-727.

78. Cartron, G., *et al.* (2002) Therapeutic activity of humanized anti-CD20 monoclonal antibody and polymorphism in IgG Fc receptor FcγRIIIa gene. *Blood*, **99**, 754-758.

79. Overdijk, M.B., *et al.* (2012) Crosstalk between Human IgG Isotypes and Murine Effector Cells. *The Journal of Immunology*, **189**, 3430.

80. Smith, P., *et al.* (2012) Mouse model recapitulating human Fcγ receptor structural and functional diversity. *Proceedings of the National Academy of Sciences*, **109**, 6181-6186.

81. Bruhns, P. (2012) Properties of mouse and human IgG receptors and their contribution to disease models. *Blood*, **119**, 5640-5649.

82. Gordon, S., *et al.* (2005) Monocyte and macrophage heterogeneity. *Nat Rev Immunol*, **5**, 953-964.

83. Heijnen, I.A., *et al.* (1996) Antigen targeting to myeloid-specific human Fc gamma RI/CD64 triggers enhanced antibody responses in transgenic mice. *Journal of Clinical Investigation*, **97**, 331-338.

84. McKenzie, S.E., *et al.* (1999) The Role of the Human Fc Receptor FcγRIIA in the Immune Clearance of Platelets: A Transgenic Mouse Model. *The Journal of Immunology*, **162**, 4311-4318.

85. Li, M., *et al.* (1996) Reconstitution of human Fc gamma RIII cell type specificity in transgenic mice. *The Journal of Experimental Medicine*, **183**, 1259-1263.

86. Bournazos, S., *et al.* (2014) Human IgG Fc domain engineering enhances antitoxin neutralizing antibody activity. *The Journal of Clinical Investigation*, **124**, 725-729.

87. Bournazos, S., *et al.* (2014) Broadly neutralizing anti-HIV-1 antibodies require Fc effector functions for in vivo activity. *Cell*, **158**, 1243-1253.

88. DiLillo, D.J., *et al.* (2014) Broadly neutralizing hemagglutinin stalk-specific antibodies require Fc[gamma]R interactions for protection against influenza virus in vivo. *Nat Med*, **20**, 143-151.

89. Heller, G.*, et al.* (1996) Resampling Procedures to Compare Two Survival Distributions in the Presence of Right-Censored Data. *Biometrics*, **52**, 1204-1213.

90. Bournazos, S.*, et al.* (2014) Humanized Mice to Study FcγR Function. In Daeron, M.*, et al.* (eds.), *Fc Receptors*. Springer International Publishing, Cham, pp. 237-248.

91. Chao, M.P.*, et al.* (2011) Therapeutic Antibody Targeting of CD47 Eliminates Human Acute Lymphoblastic Leukemia. *Cancer Research*, **71**, 1374.

92. Kim, D.*, et al.* (2012) Anti-CD47 antibodies promote phagocytosis and inhibit the growth of human myeloma cells. *Leukemia*, **26**, 2538-2545.

93. Willingham, S.B.*, et al.* (2012) The CD47-signal regulatory protein alpha (SIRPa) interaction is a therapeutic target for human solid tumors. *Proceedings of the National Academy of Sciences*, **109**, 6662-6667.

94. Liu, J.*, et al.* (2015) Pre-Clinical Development of a Humanized Anti-CD47 Antibody with Anti-Cancer Therapeutic Potential. *PLoS ONE*, **10**, e0137345.

95. Chao, M.P.*, et al.* (2010) Anti-CD47 Antibody Synergizes with Rituximab to Promote Phagocytosis and Eradicate Non-Hodgkin Lymphoma. *Cell*, **142**, 699-713.

96. DiLillo, D.J.*, et al.* (2015) Differential Fc-receptor engagement drives an anti-tumor vaccinal effect. *Cell*, **161**, 1035-1045.

97. Gordan, S.*, et al.* (2015) bIgG time for large eaters: monocytes and macrophages as effector and target cells of antibody-mediated immune activation and repression. *Immunological Reviews*, **268**, 52-65.

98. Cheever, M.A.*, et al.* (2009) The Prioritization of Cancer Antigens: A National Cancer Institute Pilot Project for the Acceleration of Translational Research. *Clinical Cancer Research*, **15**, 5323.

99. Rodeck, U.*, et al.* (1994) Expression of the WT1 Wilms' tumor gene by normal and malignant human melanocytes. *International Journal of Cancer*, **59**, 78-82.

100. Menssen, H.*, et al.* (1995) Presence of wilms' tumor gene (wt1) transcripts and the WT1 nuclear protein in the majority of human acute leukemias. *Leukemia*, **9**, 1060.

101. Campbell, C.E.*, et al.* (1998) Constitutive expression of the Wilms tumor suppressor gene (WT1) in renal cell carcinoma. *International Journal of Cancer*, **78**, 182-188.

102. Foster, M.R.*, et al.* (2001) Immunohistochemical Analysis of Nuclear Versus Cytoplasmic Staining of WT1 in Malignant Mesotheliomas and Primary

Pulmonary Adenocarcinomas. *Archives of Pathology & Laboratory Medicine*, **125**, 1316-1320.

103. Loeb, D.M.*, et al.* (2001) Wilms’ Tumor Suppressor Gene Is Expressed in Primary Breast Tumors Despite Tumor-specific Promoter Methylation. *Cancer Research*, **61**, 921.

104. Dennis, S.L.*, et al.* (2002) Expression and mutation analysis of the Wilms' tumor 1 gene in human neural tumors. *International Journal of Cancer*, **97**, 713-715.

105. Oji, Y.*, et al.* (2002) Overexpression of the Wilms' tumor gene WT1 in de novo lung cancers. *International Journal of Cancer*, **100**, 297-303.

106. Oji, Y.*, et al.* (2003) Overexpression of the Wilms' tumor gene WT1 in head and neck squamous cell carcinoma. *Cancer Science*, **94**, 523-529.

107. Oji, Y.*, et al.* (2003) Overexpression of the Wilms' tumor gene WT1 in primary thyroid cancer. *Cancer Science*, **94**, 606-611.

108. Oji, Y.*, et al.* (2003) Overexpression of the Wilms' tumor gene WT1 in colorectal adenocarcinoma. *Cancer Science*, **94**, 712-717.

109. Ueda, T.*, et al.* (2003) Overexpression of the Wilms' tumor gene WT1 in human bone and soft-tissue sarcomas. *Cancer Science*, **94**, 271-276.

110. Oji, Y.*, et al.* (2004) Overexpression of the Wilms' tumor gene WT1 in pancreatic ductal adenocarcinoma. *Cancer Science*, **95**, 583-587.

111. Oji, Y.*, et al.* (2004) Overexpression of the Wilms' tumor gene WT1 in primary astrocytic tumors. *Cancer Science*, **95**, 822-827.

112. Oji, Y.*, et al.* (2004) Overexpression of the Wilms' Tumor Gene WT1 in Esophageal Cancer. *Anticancer Research*, **24**, 3103-3108.

113. Waldstrøm, M.*, et al.* (2005) Immunohistochemical Expression of Wilms Tumor Gene Protein in Different Histologic Subtypes of Ovarian Carcinomas. *Archives of Pathology & Laboratory Medicine*, **129**, 85-88.

114. Hylander, B.*, et al.* (2006) Expression of Wilms tumor gene (WT1) in epithelial ovarian cancer. *Gynecologic Oncology*, **101**, 12-17.

115. Nakatsuka, S.-i.*, et al.* (2006) Immunohistochemical detection of WT1 protein in a variety of cancer cells. *Mod Pathol*, **19**, 804-814.

116. Pritchard-Jones, K.*, et al.* (1990) The candidate Wilms' tumour gene is involved in genitourinary development. *Nature*, **346**, 194-197.

117. Pelletier, J., *et al.* (1991) Expression of the Wilms' tumor gene WT1 in the murine urogenital system. *Genes & Development*, **5**, 1345-1356.

118. Armstrong, J.F., *et al.* (1993) The expression of the Wilms' tumour gene, WT1, in the developing mammalian embryo. *Mechanisms of Development*, **40**, 85-97.

119. Hosen, N., *et al.* (2007) The Wilms/' tumor gene WT1-GFP knock-in mouse reveals the dynamic regulation of WT1 expression in normal and leukemic hematopoiesis. *Leukemia*, **21**, 1783-1791.

120. Huang, A., *et al.* (1990) Tissue, developmental, and tumor-specific expression of divergent transcripts in Wilms tumor. *Science*, **250**, 991.

121. Park, S., *et al.* (1993) The Wilms tumour gene WT1 is expressed in murine mesoderm-derived tissues and mutated in a human mesothelioma. *Nat Genet*, **4**, 415-420.

122. Hosen, N., *et al.* (2002) Very low frequencies of human normal CD34+ haematopoietic progenitor cells express the Wilms' tumour gene WT1 at levels similar to those in leukaemia cells. *British Journal of Haematology*, **116**, 409-420.

123. Yang, L., *et al.* (2007) A tumor suppressor and oncogene: the WT1 story. *Leukemia*, **21**, 868-876.

124. Ohminami, H., *et al.* (2000) HLA class I-restricted lysis of leukemia cells by a CD8+ cytotoxic T-lymphocyte clone specific for WT1 peptide. *Blood*, **95**, 286.

125. Gaiger, A., *et al.* (2001) WT1-specific serum antibodies in patients with leukemia. *Clinical Cancer Research*, **7**, 761s-765s.

126. Oka, Y., *et al.* (2000) Cancer Immunotherapy Targeting Wilms' Tumor Gene WT1 Product. *The Journal of Immunology*, **164**, 1873.

127. Oka, Y., *et al.* (2000) Human cytotoxic T-lymphocyte responses specific for peptides of the wild-type Wilms' tumor gene (WT1) product. *Immunogenetics*, **51**, 99-107.

128. Gao, L., *et al.* (2000) Selective elimination of leukemic CD34+ progenitor cells by cytotoxic T lymphocytes specific for WT1. *Blood*, **95**, 2198.

129. Oka, Y., *et al.* (2004) Induction of WT1 (Wilms' tumor gene)-specific cytotoxic T lymphocytes by WT1 peptide vaccine and the resultant cancer regression. *Proceedings of the National Academy of Sciences of the United States of America*, **101**, 13885-13890.

130. Denkberg, G., *et al.* (2002) Direct visualization of distinct T cell epitopes derived from a melanoma tumor-associated antigen by using human recombinant

antibodies with MHC- restricted T cell receptor-like specificity. *Proceedings of the National Academy of Sciences of the United States of America*, **99**, 9421-9426.

131. Sergeeva, A., *et al.* (2011) An anti-PR1/HLA-A2 T cell receptor-like antibody mediates complement dependent cytotoxicity against acute myeloid leukemia progenitor cells. *Blood*.

132. Epel, M., *et al.* (2008) Targeting TARP, a novel breast and prostate tumor-associated antigen, with T cell receptor-like human recombinant antibodies. *European Journal of Immunology*, **38**, 1706-1720.

133. Verma, B., *et al.* (2010) Direct discovery and validation of a peptide/MHC epitope expressed in primary human breast cancer cells using a TCRm monoclonal antibody with profound antitumor properties. *Cancer immunology, immunotherapy*, **59**, 563-573.

134. Verma, B., *et al.* (2010) TCR Mimic Monoclonal Antibody Targets a Specific Peptide/HLA Class I Complex and Significantly Impedes Tumor Growth In Vivo Using Breast Cancer Models. *The Journal of Immunology*, **184**, 2156.

135. Michaeli, Y., *et al.* (2009) Expression Hierarchy of T Cell Epitopes from Melanoma Differentiation Antigens: Unexpected High Level Presentation of Tyrosinase-HLA-A2 Complexes Revealed by Peptide-Specific, MHC-Restricted, TCR-Like Antibodies. *The Journal of Immunology*, **182**, 6328.

136. Dao, T., *et al.* (2013) Targeting the Intracellular WT1 Oncogene Product with a Therapeutic Human Antibody. *Science Translational Medicine*, **5**, 176ra33.

137. Veomett, N., *et al.* (2014) Therapeutic Efficacy of an Fc-Enhanced TCR-like Antibody to the Intracellular WT1 Oncoprotein. *Clinical Cancer Research*, **20**, 4036.

138. Purbhoo, M.A., *et al.* (2004) T cell killing does not require the formation of a stable mature immunological synapse. *Nat Immunol*, **5**, 524-530.

139. Luft, T., *et al.* (2001) Exogenous Peptides Presented by Transporter Associated with Antigen Processing (TAP)-Deficient and TAP-Competent Cells: Intracellular Loading and Kinetics of Presentation. *The Journal of Immunology*, **167**, 2529.

140. Irvine, D.J., *et al.* (2002) Direct observation of ligand recognition by T cells. *Nature*, **419**, 845-849.

141. Borbulevych, O.Y., *et al.* (2010) Structures of native and affinity-enhanced WT1 epitopes bound to HLA-A*0201: implications for WT1-based cancer therapeutics. *Molecular immunology*, **47**, 2519-2524.

142. Ataie, N., *et al.* (2016) Structure of a TCR mimic antibody with target predicts pharmacogenetics. *Journal of molecular biology*, **428**, 194-205.

143. Goping, I.S., *et al.* (2003) Granzyme B-Induced Apoptosis Requires Both Direct Caspase Activation and Relief of Caspase Inhibition. *Immunity*, **18**, 355-365.

144. Breart, B., *et al.* (2008) Two-photon imaging of intratumoral CD8(+) T cell cytotoxic activity during adoptive T cell therapy in mice. *The Journal of Clinical Investigation*, **118**, 1390-1397.

145. Garrod, Kym R., *et al.* (2012) Dissecting T Cell Contraction In Vivo Using a Genetically Encoded Reporter of Apoptosis. *Cell Reports*, **2**, 1438-1447.

146. Mouchacca, P., *et al.* (2013) Visualization of Cytolytic T Cell Differentiation and Granule Exocytosis with T Cells from Mice Expressing Active Fluorescent Granzyme B. *PLOS ONE*, **8**, e67239.

147. Hamblett, K.J., *et al.* (2004) Effects of Drug Loading on the Antitumor Activity of a Monoclonal Antibody Drug Conjugate. *Clinical Cancer Research*, **10**, 7063.

148. Parekh, B.S., *et al.* (2012) Development and validation of an antibody-dependent cell-mediated cytotoxicity-reporter gene assay. *mAbs*, **4**, 310-318.

149. van den Wildenberg, S.M.J.L., *et al.* (2011) A Brief Introduction to Single-Molecule Fluorescence Methods. In Peterman, E.J.G., *et al.* (eds.), *Single Molecule Analysis: Methods and Protocols*. Humana Press, Totowa, NJ, pp. 81-99.